

# UC Irvine

## UC Irvine Electronic Theses and Dissertations

### Title

Wake Simulation of the Multicopter Test Bed and Validation of CHARM Software

### Permalink

<https://escholarship.org/uc/item/2d78x5rv>

### Author

SHIRAZI, DORSA

### Publication Date

2020

### Copyright Information

This work is made available under the terms of a Creative Commons Attribution License, available at <https://creativecommons.org/licenses/by/4.0/>

Peer reviewed|Thesis/dissertation

**Wake Simulation of the  
Multicopter Test Bed  
and Validation of CHARM Software**

BY

**DORSA SHIRAZI**

submitted in partial satisfaction of the requirements for  
the degree of Master of Science in  
Mechanical and Aerospace Engineering

UNIVERSITY OF CALIFORNIA, IRVINE

**Thesis Committee:**

**Derek Dunn-Rankin, Ph.D., Advisor, Committee Chair**

**Yu-Chien Chien, Ph.D., Co-advisor, Committee**

**Haitem Taha, Ph.D., Committee Member**

## **Acknowledgments**

The author would like to thank her advisers Professor Dunn-Rankin and Dr. Yu-Chien (Alice), who have guided her and allowed her to grow in the past five years of her education at the University of California Irvine. The author would like to acknowledge Kristen Kallstrom, who has been an absolute help in this project and developed the airfoil tables for the KDE rotor. Also, a shout out to Sarah Conley, Carl Russell, Dan Wachspress, Ethan Romander, Gloria Yamauchi, Wayne Johnson, Witold Koning, Alyna Anderson, Michael Keenan, Finbar Argus, Michelle Dominguez, who gave so very generously their knowledge and time.

The author would also like to express profound gratitude to her husband, Sepehr Hemmati, family, friends, and boss, Dr. William Warmbrodt. The author is sincerely appreciative of their encouragement, advice, and support. Their support not only made this work possible but greatly influenced the author's rapid health recovery process.

Last but not least, a big thanks to Professor Oscar Stafsudd at the University of California, Los Angeles. Doctor Stafsudd introduced the author to the field of research back in 2015. He believed in her and allowed her in his lab when she was just a community college student with no research experience.

# Contents

<b>Acknowledgements</b>	<b>1</b>
<b>List of Figures</b>	<b>4</b>
<b>List of Tables</b>	<b>9</b>
<b>Nomenclature</b>	<b>11</b>
<b>Abstract</b>	<b>13</b>
<b>1 Motivation and Background</b>	<b>15</b>
1.1 Introduction.....	15
1.2 Multirotor Test Bed.....	16
1.2.1 Multirotor Test Bed Wind Tunnel Testing .....	17
1.2.2 Multirotor Test Bed Test Matrix .....	20
<b>2 CHARM Numerical Method and Settings</b>	<b>21</b>
2.1 Introduction to CHARM.....	22
2.2 CHARM Input Files .....	23
2.2.1 2D Airfoil Section Data Input File .....	23
2.2.2 Blade Geometry Input File .....	27
2.2.3 Blade Dynamics Input File.....	30
2.2.4 Rotor Wake Input File.....	34
2.2.5 Run Characteristics Input File .....	37
2.3 Output Files.....	41
2.4 Vortex-X.....	42
<b>3 CHARM Validation</b>	<b>44</b>
3.1 Figure of Merit Validation Parameter .....	44
3.2 UH-60A Performance Validation .....	48
3.2.1 UH-60A Experiment.....	59



3.2.2	UH-60A Flight Performance .....	50
3.3	SUI Performance Validation .....	52
3.3.1	SUI Experiment .....	52
3.3.2	SUI Flight Performance.....	55
<b>4</b>	<b>Simulation Results of MTB</b>	<b>59</b>
4.1	KDE Rotor in CHARM .....	60
4.1.1	Rotor Positions in CHARM .....	63
4.2	Isolated Rotor in Hover.....	64
4.3	Simulation of Multirotor Test Bed in Forward Flight in the Wind Tunnel.....	67
4.3.1	One Rotor in the Wind Tunnel .....	68
4.3.2	Two Rotors in the Wind Tunnel .....	71
4.3.3	Four Rotors in the Wind Tunnel.....	73
4.3.4	Six Rotors in the Wind Tunnel .....	75
4.4	Agreement with Experiments.....	78
4.5	Simulation of Multirotor Test Bed without Wind Tunnel.....	79
<b>5</b>	<b>Discussion</b>	<b>84</b>
5.1	Multirotor Test Bed in Wind Tunnel and Free Field Results comparison to Experiments.....	84
5.2	Wake Effect.....	87
<b>6</b>	<b>Conclusion and Future Work</b>	<b>93</b>
6.1	Conclusion.....	93
6.2	Future Work .....	94
	<b>References</b>	<b>96</b>
	<b>Appendix A: Data Sheets</b>	<b>101</b>
	<b>Appendix B: Flow Visualization Vortex-X</b>	<b>105</b>
	<b>Appendix C: CHARM Input Files</b>	<b>113</b>

## List of Figures

1.1	MTB CAD assembly [51] .....	16
1.2	MTB in the 7- by 10-Foot Wind Tunnel at Ames Research Center [4].....	17
1.3	Location of MTB on the turntable at the wind tunnel [5] .....	18
1.4	Location of MTB and rotors in the wind tunnel test section .....	18
1.5	Rotors identification numbers and spin directions.....	19
2.1	Parts and aerodynamic terms of an airfoil [21] .....	24
2.2	Variation of lift coefficient vs. the angle of attack.....	24
2.3	Location of several airfoil station thought the propeller [22].....	26
2.4	An example of <i>2D airfoil section data</i> input file.....	27
2.5	The elastic axis on the V-22 rotor blade.....	28
2.6	The sweep angle.....	28
2.7	Anhedral and dihedral angles [26] .....	29
2.8	The plane flap versus split flap.....	29
2.9	An example of <i>blade geometry</i> input file.....	30
2.10	<i>A blade dynamics</i> input file from CHARM tutorial.....	31
2.11	The main rotor's hub and hinge system.....	33
2.12	The blade flapping.....	33
2.13	Leading and lagging in fully articulated rotor blade.....	33
2.14	Tilt, shaft, and collective angles.....	35
2.15	UH-60A airloads rotor in the 40- by 80-Foot Wind Tunnel at Ames Research Center (ARC) [35] .....	35
2.16	Schematic of free wake model.....	36
2.17	<i>A rotor/wake</i> input file from CHARM tutorial.....	37
2.18	<i>A run characteristics</i> input file from CHARM tutorial.....	38
2.19	Shows (a) positive shaft angle and (b) negative shaft angle .....	39
2.20	[NAME]sweep.dat output file example.....	42
2.21	[NAME].off output file example.....	42
2.22	The simulation of MTB with six rotor in Vortex-X software .....	43

3.1	Streamtube at hovering flight.....	45
3.2	UH-60A rotor system at the National Full-Scale Aerodynamics Complex wind tunnel [44].....	48
3.3	Vortex-X simulation of the UH-60A rotor system out of ground effect in hover.....	50
3.4	Figure of merit comparison for UH-60A rotor system at a 0 degrees shaft angle in hover .....	51
3.5	The power comparison of UH-60A rotor system with wind tunnel data at a 0 degrees shaft angle in hover .....	51
3.6	Hover test for the SUI isolated rotor in 7- by 10-Foot Wind Tunnel[47].....	52
3.7	The header of the 2D airfoil section data input file for SUI rotor.....	53
3.8	Axial view of SUI rotor (top), and 20 radial station segments (bottom) [46].....	54
3.9	CHARM description of the 7- by 10-Foot Wind Tunnel in the <i>run characteristics</i> input file .....	55
3.10	SUI hover case results using 20 airfoil sections to define the <i>blade geometry</i> input file .....	56
3.11	The thrust values for SUI rotor at forward flight at four different pitch angles .....	57
3.12	SUI rotor in hover .....	58
3.13	SUI rotor at forward flight.....	58
4.1	Axial view of KDE rotor and 28 cross sections- in blade geometry input file the geometry of 20 airfoil cross section was used starting at the root cut (marked in red) [52].....	60
4.2	Blade regions in vertical descend.....	61
4.3	Graphical representation of advancing and retreating sides of a rotor.....	62
4.4	The coordinate defined by CHARM for MTB structure test stand in free stream. Notice that this MTB system is a side view with the free stream coming from the left (while Figure 1.5 is a top view with the free stream coming from the right).....	63
4.1	The MTB structure and location of the rotors at (a) 0 shaft angle and (b) negative shaft angle.....	64
4.2	Side view of the MTB at shaft angles of (a) 0 degrees, (b) -5 degrees, and (c) -10 degrees .....	64

4.3	Aerodynamic forces on a rotor disk (right) - forces and moments on the load cell (left).....	65
4.4	Isolated rotor in hover – RPM <sup>2</sup> vs thrust.....	66
4.5	Isolated rotor in hover – RPM <sup>3</sup> vs power.....	66
4.6	Isolated rotor in hover – RPM vs figure of merit.....	67
4.7	The top view of location of the rotor number two inside the wind tunnel boundary defined by CHARM.....	69
4.8	The side view of location of the rotor number two inside the wind tunnel boundary defined by CHARM.....	69
4.9	The rotor thrust and power values for single rotor cases in the short configuration at wind tunnel in forward flight testing at 20 and 40 ft/s.....	70
4.10	Flow visualization of single KDE rotor in the short rotor configuration, a -10 degrees pitch angle, and a forward flight speed of 20 ft/s in the wind tunnel....	71
4.11	The top view of location of rotors number three and four inside the wind tunnel boundary defined by CHARM.....	71
4.12	Averaged thrust and average power values for two rotor cases in the short configuration at wind tunnel in forward flight testing.....	72
4.13	Flow visualization of rotors number three and four at short rotor configuration, -10 degrees pitch angle, with speed of 20 ft/s in wind tunnel.....	73
4.14	The top view of location of rotors number 1-4 inside the wind tunnel boundary defined in CHARM.....	73
4.15	Averaged thrust and power values for four rotor cases in the short configuration at wind tunnel in forward flight testing.....	74
4.16	Flow visualization of rotors numbers 1-4 in the short rotor configuration, at the -10 degrees pitch angle, and with a wind tunnel speed of 20 ft/s.....	75
4.17	Rotors height in the wind tunnel at 0 degrees pitch angle at (a) tall and (b) short configuration for six rotor cases.....	75
4.18	The top view of location of rotors number 1-6 inside the wind tunnel boundary defined in CHARM.....	76
4.19	Data and CHARM results for six rotors at short configuration in the wind tunnel - thrust and power vs. pitch angle.....	76
4.20	Experimental data and CHARM results for six rotors at tall configuration in the wind tunnel - thrust and power vs. pitch angle.....	78

4.21	Six rotors at tall configuration in the wind tunnel, with a -10 degrees pitch angle and forward flight speed of 20 ft/s.....	79
4.22	Single rotor in free field - thrust and power vs. pitch angle.....	80
4.23	Two rotor and four rotor free field cases- average thrust and average power vs. pitch angle.....	81
4.24	Six rotors at short and tall configurations in free field - thrust and power vs. pitch angle - forward speeds of 20 ft/s and 40 ft/s.....	83
5.1	Single rotor at short configurations - thrust and power vs. pitch angle .....	85
5.2	Two rotors at short configurations - thrust and power vs. pitch angle.....	85
5.3	Four rotors cases in short configurations - thrust and power vs. pitch angle.....	86
5.4	Six rotor case in the short configurations - thrust and power vs. pitch angle.....	86
5.5	Six rotor case in the tall configurations - thrust and power vs. pitch angle .....	87
5.6	Four rotor cases - rotors interactions - forward flight speed 20 ft/s.....	88
5.7	Six rotor cases at short and tall configurations - rotor wakes interactions - forward flight speed 20 and 40 ft/s .....	90
5.8	Six rotor wake interactions at (a) 0 degrees pitch and 20 ft/s, (b) 0 degrees pitch and 40 ft/s, (c) -10 degrees pitch and 20 ft/s, and (d) -5 degrees pitch and 20 ft/s.....	91
6.1	SUI blade geometry.....	101
6.2	SUI airfoil geometry at 22 radial stations [47].....	102
6.3	Parts and aerodynamic terms of an airfoil.....	103
6.4	Rotors location in CHARM simulations.....	104
6.5	Isolated KDE rotor at hover .....	105
6.6	Single KDE rotor at forward flight 20 ft/s in wind tunnel - pitch -10 degrees - side view .....	105
6.7	Single KDE rotor at forward flight 20 ft/s in wind tunnel - pitch -5 degrees - side view .....	106
6.8	Single KDE rotor at forward flight 40 ft/s in wind tunnel - pitch 0 degrees - side view .....	106
6.9	Single KDE rotor at forward flight 40 ft/s in free field - pitch 0 degrees - side view .....	106
6.10	Single KDE rotor at forward flight 40 ft/s in free field - pitch -10 degrees - side view .....	107
6.11	Single KDE rotor at forward flight 40 ft/s in wind tunnel - pitch 0 degrees - top view .....	107
6.12	Two rotor cases at forward flight 20 ft/s in wind tunnel with pitch -10 degrees .....	107
6.13	Two rotor cases at forward flight 20 ft/s in wind tunnel - side view - pitch angle (a) -10 degrees (b) -5 degrees (c) 0 degrees .....	108

6.14	Four rotor cases at forward flight 20 ft/s in wind tunnel - side view - pitch angle (a) -10 degrees (b) -5 degrees (c) 0 degrees .....	109
6.15	Four rotor cases at forward flight 20 ft/s in wind tunnel - top view – pitch angle 0 degrees.....	110
6.16	Six rotor cases in tall configuration at forward flight 20 ft/s in wind tunnel - side view - pitch angle (a) -10 degrees (b) -5 degrees (c) 0 degrees.....	110
6.17	Six rotor cases in tall configuration at forward flight 20 ft/s in wind tunnel - top view - pitch angle (a) -10 degrees (b) -5 degrees (c) 0 degrees.....	111
6.18	Six rotor cases in tall configuration at forward flight 40 ft/s in wind tunnel - top view - pitch angle 0 degrees.....	112

# List of Tables

1.1	MTB wind tunnel - test variables.....	19
1.2	MTB test cases.....	20
2.1	Categorizing the flight using the Mach number.....	25
2.2	IFVFLGS setting for wake calculation.....	40
3.1	UH-60A rotor parameters.....	49
3.2	SUI rotor parameters.....	53
3.3	SUI rotor parameters for <i>2D airfoil section data</i> input file.....	53
3.4	SUI blade geometry distribution.....	55
4.1	The KDE rotor parameters.....	60
4.2	Reynolds number of four main airfoil stations used to generate the airfoil tables in XFOIL.....	62
4.3	MTB test matrix.....	68
4.4	Discrepancy between the CHARM prediction and experimental data for single rotor at the wind tunnel in forward flight testing.....	70
4.5	Discrepancy between the CHARM prediction and experimental data for two MTB rotors at the wind tunnel in forward flight testing speed of 20 ft/s.....	72
4.6	Discrepancy between the CHARM prediction and experimental data for four MTB rotors at the wind tunnel in forward flight testing at speed of 20 ft/s.....	74
4.7	Discrepancy between the CHARM prediction and experimental data for six rotors case at short configuration at the wind tunnel in forward flight speed of 20 and 40 ft/s.....	77
4.8	Discrepancy between the CHARM prediction and experimental data for six rotors case at tall configuration at the wind tunnel in forward flight speed of 20 and 40 ft/s.....	77
4.9	Discrepancy between the CHARM predictions and experimental 4.10 data for the single rotor case in free field forward flight.....	80
4.11	Discrepancy between the CHARM predictions and experimental 4.12 data for two and four rotors at forward flight in free field.....	80
4.13	Discrepancy between the CHARM prediction and experimental data for six rotors in short and tall configurations at forward flight in free field...82	82

5.1	Thrust and power discrepancies between simulations and experimental data for front and middle rotors in four rotors case.....	88
5.2	Absolute discrepancy of average thrust and power between prediction and experimental data for front, middle, and back rotors in six rotor cases at short configuration.....	91
5.3	Absolute discrepancy of average thrust and power between prediction and experimental data for front, middle, and back rotors in six rotor cases at tall configuration.....	92
6.1	Absolute average discrepancy between CHARM wind tunnel and free field prediction and experimental data.....	94
6.2	Absolute maximum discrepancy between CHARM wind tunnel and free field prediction and experimental data.....	94



# Nomenclature

$A$	rotor disc area [m <sup>2</sup> ]
$a$	speed of sound air [m/s]
$C_D$	drag coefficient
$C_L$	lift coefficient
$C_M$	moment coefficient
$C_P$	power coefficient
$C_Q$	torque coefficient
$C_T$	thrust coefficient
$c$	chord length [m]
$c_d$	section drag
$c_l$	section lift
$c_m$	section moment
$D$	drag [N]
$FM$	figure of merit
$L$	lift [N]
$M$	Mach number
$M$	Molecular mass of gas
$N$	Number of blades
$P$	rotor power [W]
$P_m$	mechanical power [W]
$Q$	torque [N- m]
$R$	rotor radius [m]

$R$	gas constant
$Re$	Reynolds number
$RPM$	revolutions per minute
$T$	thrust [N]
$T$	absolute temperature
$V$	velocity [m/s]
$V_\infty$	free stream velocity [m/s]
$v_i$	induced velocity [m/s]
$w$	wake velocity [m/s]
$X$	independent variable
$\alpha$	angle of attack [degree]
$\beta$	rigid flapping mode
$\gamma$	adiabatic constant
$\delta$	discrepancy
$\mu$	dynamic viscosity [(N s)/m <sup>2</sup> ]
$\Omega$	angular velocity [rad/s]
$\rho$	density [kg/m <sup>3</sup> ]
$\sigma$	rotor solidity

# Abstract

Urban air mobility as a fast transportation solution has captured the attention of private companies and government aviation departments in the 21st century. The new designs of aerial vehicles are coming one after another but often neglecting the aerodynamic characteristics and the effect of interacting rotors. The Multirotor Test Bed (MTB) project was initiated at NASA Ames Research center to support the NASA Revolutionary Vertical Lift Technology (RVLT) Project to study rotorcraft performance specifically for multirotor aircraft. The MTB is a modular multirotor that can make testing feasible for up to six rotors at different angles and rotor arrangements, including tall and short configurations at different horizontal and vertical distances. The MTB is assembled and tested in the U.S Army's 7- by 10-Foot Wind Tunnel. This work focuses on the importance of aerodynamic interaction between MTB rotors using the Comprehensive Hierarchical Aeromechanics Rotorcraft Model (CHARM) software, developed commercially by Continuum Dynamics, Inc. The CHARM software is capable of modeling Vertical Take Off and Landing (VTOL) aircraft aerodynamics in maneuvering and steady flight conditions. CHARM allows the user to define flow and body characteristics, including the rotor geometry, aerodynamic condition, wind tunnel speed, and airfoil tables as inputs. This report first examines CHARM's capability by comparing its predictions to the UH-60A Black Hawk rotor and SUI Endurance rotor experimental test results in hover and forward flight conditions. These comparisons can help to validate CHARM results, provide a better understanding of simulated flight characteristics, and demonstrate its predictive capability.

With these validations as the foundation, this work then simulates one MTB rotor in hover, and further compares with wind tunnel test data as the confirmation of the CHARM parameters. Once accurate performance is verified, the MTB rotor is simulated in forward flight both in the wind tunnel and in a free field environment. The simulation variables include one, two, four, and six rotors at the short and tall configurations, and with shaft angles of 0, -5, and -10 degrees. These results can demonstrate the rotor wake interaction and its impact on rotor performance. This

information can also help determine which configurations should be explored for the future wind tunnel tests. This study can be used as guidance for using CHARM to predict rotor behavior and understanding the importance of the rotor wake interaction for future air mobility designs.

Keywords: Urban Air Mobility, Multicopter, CHARM

---

# CHAPTER 1

---

## Motivation and Background

Since 1820, thousands of different aircraft have been designed and constructed, but creating an efficient and affordable aerial vehicle is still a challenge, particularly for multi-rotor craft. Each vehicle needs a different design due to various size, flight condition, rotor size, and engine type constraints associated with the desired task of the aircraft. Having reliable computational software that accurately predicts aircraft performance can improve safety and reduce time and costs in bringing the design to fruition. This study demonstrates and validates the use of a numerical simulation tool, CHARM, and shows its potential and feasibility for modeling rotorcraft in relation to real flight conditions and compares to experimental data. This study is focused on whether CHARM can help determine the critical factors in designing a six-rotor vehicle using wind tunnel data and simulation results.

### 1.1. Introduction

It is clear in the past two decades that multi-rotor aircraft have been and will continue to be the major contributors to surveillance, search and rescue, and resource mapping, along with a host of further applications. In response to this recognition, NASA started to explore multirotor aerodynamic performance in 2015 and 2017 [1, 2]. Several quadcopters were tested in the U.S. Army 7- by 10-Foot Wind Tunnel at NASA Ames Research Center. The experimental results of the wind tunnel have provided scientific information to better understand the small Unmanned Aircraft System (sUAS) performance. These data include the importance of the rotor size and material, and the impact of payload weight, aircraft size, and rotor performance. However, these early experiments had some limitations. For example, the entire

aircraft was connected to one load cell, which only allows the measurement of the overall performance of the vehicle. This then provides only limited understanding of the individual aerodynamic behavior of the rotors. In addition, the quadcopter sUAM were manufactured for a fixed rotor distance ratio; therefore, no adjustment was possible to test different rotor distance combinations. These limitations led to the attention and need for a multirotor test bed that would allow an adjustable assembly with individual load cells per rotor to accomplish independent, and more accurate measurements for thrust and power of each rotor [6]. The completed multirotor test bed (MTB) assembly accomplished these improvements and also allowed for lateral, longitudinal, and vertical adjustment of rotors positions. In addition, each rotor has a load cell and can tilt individually. Moreover, the pitch angle of the entire assembly can change using the shaft that is connected to the central beam of the MTB structure, as shown in Figure 1.1. Further, different propeller sizes can be tested on the MTB due to longitudinal, vertical, and lateral distance adjustability.

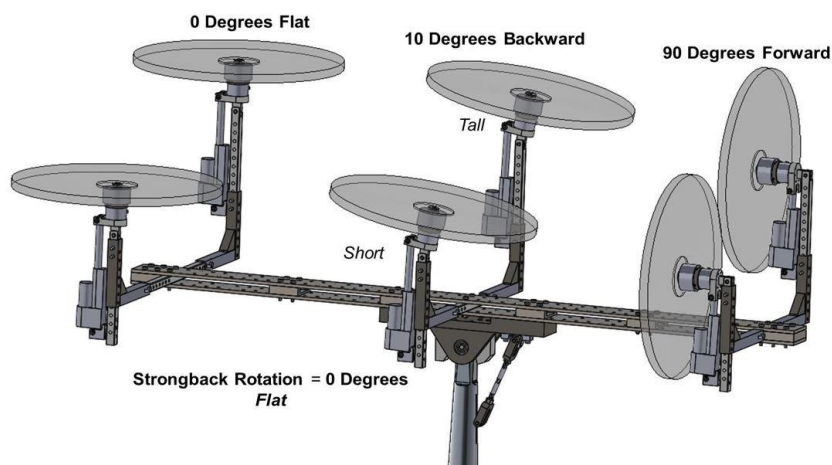


**Figure 1.1:** MTB CAD assembly [51]

## 1.2. Multirotor Test Bed

The MTB project started with the goal of creating a flexible testbed to study multirotor configurations and the performance of each rotor and the aerodynamic interaction and acoustics [6]. Figure 1.2 shows the MTB assembly located in the U.S. Army 7- by 10-Foot Wind Tunnel. Details of the MTB are provided next and also described in a paper by Sarah Conley<sup>1</sup> and Carl Russell<sup>2</sup> [4]. The first run of

---

<sup>1</sup> Mechanical Design Engineer and Deputy Test Director

<sup>2</sup> Test Director, Principal Investigator

the MTB system occurred in October 2019.

The MTB assembly can pitch 30 degrees forward and 10 degrees aft. Each rotor can tilt 90 degrees forward and 10 degrees aft. Further, the MTB assembly allows adjusting the longitudinal, vertical, and lateral distances. The longitudinal spacing is between 25.5 inches and 72.0 inches, with an adjustability of 1.5-inch increments. The lateral spacing between rotors can change between 24.7 inches to 38.7 inches in one-inch increments. The vertical distance can increase 9 inches from the short configuration to the tall configuration, with one-inch intermediate increments if desired. The MTB assembly weighs approximately 340 lbs, and most of the parts are made out of 17-4PH H900 stainless steel, 13-8PH H950 stainless steel, 932 bearing bronze, and AISI 4130 alloy steels.



**Figure 1.2:** MTB in the 7- by 10-Foot Wind Tunnel at Ames Research Center [4]

### **1.2.1. Multirotor Test Bed Wind Tunnel Testing**

The MTB test was performed in the U.S. Army wind tunnel. This wind tunnel's test section has dimensions of 7.0 x 10.0 x 15.0 feet. Figure 1.3 shows the MTB structure connected through the shaft to the middle of the turntable in the test section of the wind tunnel.

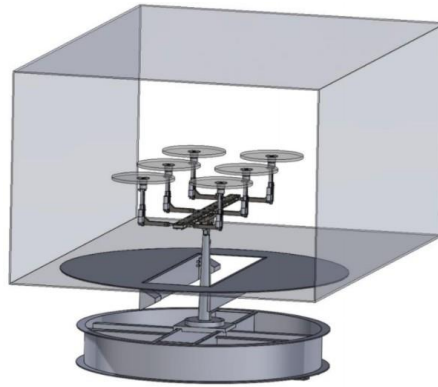


**Figure 1.3:** Location of MTB on the turntable at the wind tunnel [5]

After the MTB was assembled in the wind tunnel, each rotor location was measured and recorded. Figure 1.4 shows the top view of the wind tunnel and the position of the six rotors. Note that the center of the MTB is not at the center of the wind tunnel test section. The MTB center is about  $5/32$  inches forward in the positive X-axis direction, and  $3/8$  inches closer to one of the walls in the positive y-direction. The rotor used for the MTB project, the KDE -CF245-DP with 24.5 inch diameter, has its tips at 2.40 and 2.34 inches from the side walls.

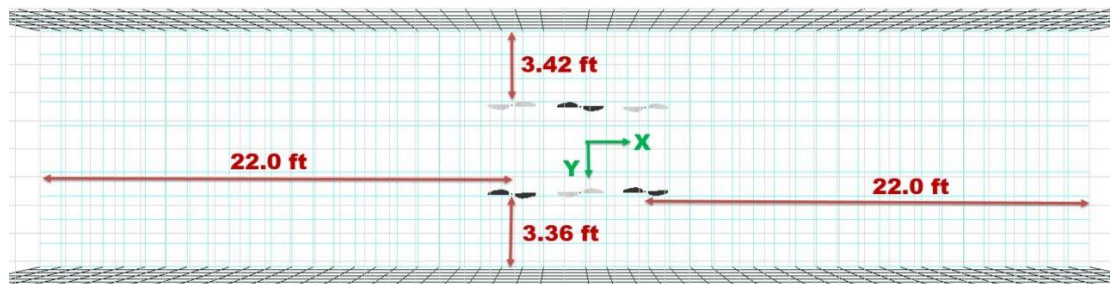


**Figure 1.4:** Location of MTB and rotors in the wind tunnel test section

Each rotor has a six-axis load cell. Each load cell can handle 10 lbs of thrust and  $\pm 20$  lbs of oscillations. Also, each rotor has a rotational speed sensor to record the individual rotor RPM. The rotor numbers, spin directions, and wind direction are shown in Figure 1.5. The lower rotor numbers are located upstream at the front of the group. Rotors one, four, and five are spinning counter-clockwise. Rotors two, three, and six are turning clockwise to cancel out the gyroscopic effect from rotors one, four, and five.



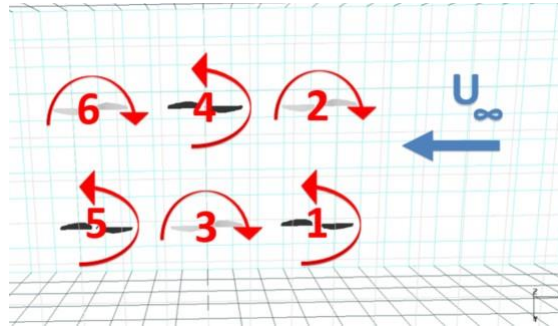


**Figure 1.5:** Rotor identification numbers and spin directions

In this report, all the cases were tested at the rotor speed of 2000 RPM, and wind tunnel speeds of 20 and 40 ft/sec. The lateral and longitudinal distances between the rotors were held constant at 38.7 and 36 inches, respectively. The distance between rotors was measured from the center of the rotor, hub to hub. For the purpose of this research, two different vertical distances were tested: short and tall. For the tall configuration, the rotor is located 7 inches higher than in the short configuration. Also, the entire assembly was tested at the pitch angles of 0, -5, and -10 degrees with a constant tilt of 0 degrees from all individual rotors. Table 1.1, shows the MTB test variables being used for the comparisons made in this report [6]. To develop a better understanding of rotor performance, one variable was changed in each case.

**Table 1.1:** MTB wind tunnel - test variables

Variable	Fixed/Changing	Low	High	Unit
Vertical Distance	Changing	short	long	inch
Lateral Distance	Fixed	36	36	inch
Longitudinal Distance	Fixed	38.7	38.7	inch
Shaft Angle	Changing	0	10	degrees
Rotor Speed	Fixed	2000	2000	RPM
Number of Rotors	Changing	1	6	
Wind tunnel Speed	Changing	20	40	ft/s

## 1.2.2. Multirotor Test Bed Test Matrix

In 2019, the MTB was experimentally evaluated with different test case conditions, such as the RPM sweep, yaw sweep, wind tunnel air speed, MTB assembly pitch angle, and number of rotors. The six rotor case was tested at the two vertical configurations (tall and short) to study the wall effects. For two rotor tests, all rotors were removed except the middle rotors. For the four rotor case, the back rotors were removed. While many hover cases were tested in 2019 with different numbers of rotors, only one of the hover cases has been cleared to be used for this report. For the one rotor case, data was collected at hover using rotor number 2. Note that the MTB is an ongoing project, and only some of the wind tunnel data were available to use in this paper. Table 1.2 shows the number of rotors that were used for the four different case types. The full MTB test matrix and rotor positions in the wind tunnel are shown in Appendix A.

**Table 1.2:** MTB test cases

Case	Rotors Used	Vertical Configuration
One Rotor	2	Short
Two Rotors	3,4	Short
Four Rotors	1,2,3,4	Short
Six Rotors	1,2,3,4,5,6	Short and Tall

---

# CHAPTER 2

---

## CHARM Numerical Method and Settings

CHARM is a comprehensive VTOL aircraft analysis developed by Continuum Dynamics Inc (CDI). CHARM models the aircraft aerodynamic and dynamic interactions using a combination of Fast Vortex/Fast Panel Solution methods. Its objective is to provide accurate results for aerodynamic interactions with short computational time. NASA is interested in this computational approach because the CHARM software requires less CPU usage and memory, so that the simulation can be completed in a shorter amount of time and with reduced computational resources when compared with high-fidelity computational fluid dynamics (CFD) solvers. CHARM is therefore an appropriate tool for conceptual design studies along with other commonly used software designed for rotorcraft simulation, such as CAMRADII<sup>1</sup> [7, 24] and RotCFD<sup>2</sup> [51]. CHARM simulates real-time free wake instability, and it also allows the examination of the rotor performance, particularly for multi-rotors and possible wake-body interactions. These capabilities show the value of CHARM for simulating the performance of generic multirotor systems. These simulations require comparison with experimental results, which is the focus of this paper. This chapter will provide information about the CHARM software, including its settings and capabilities.

---

<sup>1</sup> Comprehensive Analytical Model of Rotorcraft Aerodynamics and Dynamics (CAMRADII) is an aeromechanical analysis of helicopters and rotorcraft, which was developed by Dr. Wayne Johnson.

<sup>2</sup> RotCFD, a CFD code developed by Sukra Helitek, Inc.

## 2.1. Introduction to CHARM

This section draws most of its information from the CHARM User's Manual (Version 6.4) developed by Wachspress et al. from Continuum Dynamics Inc. and other documentation distributed by the developers [13-16,49-50]. Hence, this paper is a description of the expected and past proven performance of CHARM along with the author's view. The CHARM software runs under Linux, Windows, or macOS operating systems. CHARM uses the combination of fast vortex and fast panel solution methods [14,15,18] to model the aircraft aerodynamic and dynamic interactions to deliver information such as load, trim, wake geometry, and surface pressure. In the fast panel method, each panel has a constant source and doublet strength, where the source strengths satisfy the Dirichlet boundary<sup>1</sup> conditions for the ambient flow field. The developers of CHARM indicate that the Fast Vortex/Fast Panel method uses a grouping scheme in addition to a validated multipole approximation to decrease the computational time by over two orders of magnitude for  $10^5$  panels. In the grouping technique, the vertices and panels are grouped into nested cells. For high-density areas, these grids will be more refined for nested cells. The calculation has been determined by using multipole expansion and Taylor series extrapolations. Note that the panel method has some limitations in the quality of modeling flow separation. Also, this method requires a knowledgeable user to set up proper panel representations of bodies. In addition, CHARM uses the Constant Vorticity Contour (CVC) approach to model wakes [16]. The CVC is capable of determining the swirl velocity profile and rolled up vortex [18]. The CVC has been shown to improve wake geometry and induced velocity predictions. Note that even though CVC does not require the user to supply different values of tip vortex core radius for different flight conditions and configurations, the predicted internal structure of the rolled-up vortex remains approximate [18,19]. Compared to higher-order methods, CHARM uses the panel method to solve inviscid potential flows, which results in less CPU and memory usage. The potential flow panel method allows the rotor wash characteristics from the presence of a wind tunnel or influence of the fuselage to be included by using, for example, the fast panel fuselage model in CHARM [18,

---

<sup>1</sup> For the Dirichlet boundary condition, one of the boundaries must have a constant value, e.g.,  $u(x) = \text{constant}$

49-50]. The potential flow panel code provides a simple way to combine the fixed and rotating frames, which is an advantage over the Euler/Navier- Stokes numerical methods. However, the Euler/Navier-Stokes approaches are capable of capturing the motion of the viscous fluid at the cost of extensive computational time and memory.

## 2.2. CHARM Input Files

To simulate a rotor system in CHARM, a *run characteristics* input file is needed in addition to four input files. These four files are *rotor/wake*, *blade geometry*, *blade dynamics*, and *2D airfoil section data* input files. The *run characteristics* input file provides the flight condition and rotor parameters. The *rotor/wake* input file contains the rotor configuration and wake model parameters. The *blade geometry* input file has blade geometry information; the *blade dynamics* input file carries the blade dynamics solution parameters; and the *2D airfoil section data* input file has information on the 2D airfoil section in C81 or F-Gen format [11,12]. In the discussion that follows, the following convention is used for naming these input files:

1. The *run characteristics* input file (*Name.inp*)
2. The *rotor/wake* input file (*Name.rw.inp*)
3. The *blade geometry* input file (*Name.bg.inp*)
4. The *blade dynamics* input file (*Name.bd.inp*)
5. The *2D airfoil section data* input file (*Name.af.inp*)

The next five subsections provide an introduction to each input file.

### 2.2.1. 2D Airfoil Section Data Input File

A conventional airfoil geometry is characterized by its upper camber, lower camber, leading-edge radius, trailing edge thickness, mean camber, and chord line, Figure 2.1. These features change the airflow behavior over the airfoil. The aerodynamic forces on an airfoil depend on the angle of attack  $\alpha$ , the density of the air  $\rho$ , the velocity of the free-stream  $V_\infty$ , the viscosity of the air  $\mu$ , and the speed of sound in the free stream  $a_\infty$ .

$$F = f_n(V_\infty, \rho, \alpha, \mu, a_\infty) \quad (2.1)$$

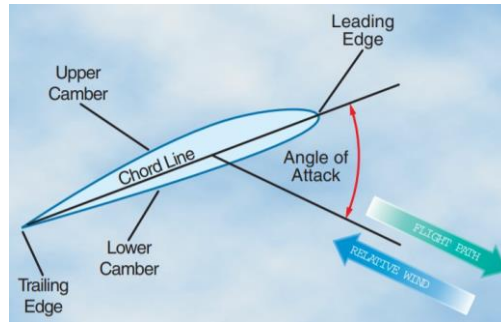


**Figure 2.1:** Parts and aerodynamic terms of an airfoil [21]

The drag and lift vary with the angle of attack, which is defined as the angle between the chord line and the airflow direction. Figure 2.2 shows the three regions of the lift coefficients versus the angle of attack [21]; linear region, nonlinear region, and stall region.

In the linear region, the lift coefficient increases proportionally to increasing the angle of attack. At the nonlinear region right before the stall point, the drag increases due to the initial separation of flow from the airfoil's surface. In this region, the lift coefficient increases at a slower rate with increasing the angle of attack. Start of region three is the stall point, known as the maximum lift coefficient, the airfoil experiences an increasingly large amount of drag with increase in angle of attack and much less lift. Due to this phenomenon, the 2D airfoil tables, along with all the calculations in this report, will remain in the linear region to avoid the complexity of the nonlinear separation and stall region.

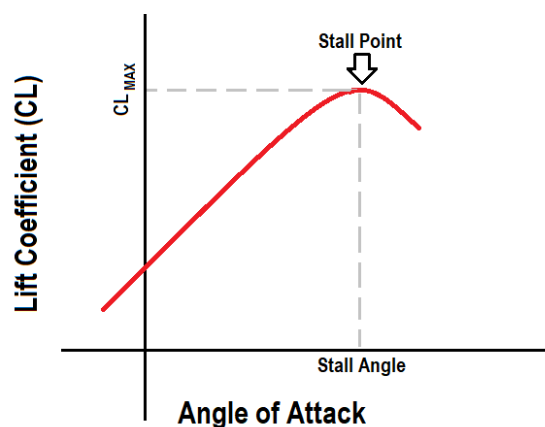


**Figure 2.2:** Variation of lift coefficient vs. the angle of attack

The *2D airfoil section data* input file contains the aerodynamic coefficients, section

lift  $c_l$ , section drag  $c_d$ , and section moment  $c_m$ , which are generated according to the angle of attack  $\alpha$  and the Mach number  $M$  of each airfoil section. Mach number is a dimensionless quantity defined as the ratio of the freestream flow velocity  $V$  to the speed of sound  $a$ , Equation 2.2. Table 2.1 shows the Mach number regimes. For this report, all the Mach numbers will not exceed sonic conditions  $0 < M \leq 1$ .

$$M = \frac{V}{a} \quad (2.2)$$

$$M = \frac{V}{\sqrt{\gamma R T}}$$

**Table 2.1:** Categorizing the flight using the Mach number

Regime	Subsonic	Transonic	Sonic	Supersonic	Hypersonic	Hypervelocity
Mach	<0.8	0.8–1.2	1.0	1.2–5.0	5.0–10.0	>10.0

The aerodynamic coefficient for each airfoil section was calculated using Equation 2.3, where  $C_L$  is the lift coefficient,  $C_D$  is the drag coefficient,  $C_M$  is the moment coefficient,  $L$  is lift,  $D$  is drag,  $M$  is moment,  $\rho$  is air density,  $c$  is the cord, and  $V_\infty$  is free stream velocity. Note that the  $\frac{1}{2}\rho V_\infty^2$  is the dynamic pressure.

$$c_l = \frac{L}{\frac{1}{2}\rho V_\infty^2 c} \quad c_d = \frac{D}{\frac{1}{2}\rho V_\infty^2 c} \quad c_m = \frac{M}{\frac{1}{2}\rho V_\infty^2 c} \quad (2.3)$$

The rotor geometry changes from the root to the tip to improve rotor performance and achieve higher lift at a slower speed. One example of parameters that change through the propeller blade is the twist angle. Since a rotor's geometry is changing through its length, it is critical to input the geometry of several airfoil stations and aerodynamic coefficients to increase the simulation accuracy. Using several airfoil stations increases simulation accuracy and allows for more accurately modeling of the blade's actual geometry. Figure 2.3 shows the location of several airfoil cutouts at different radial stations on the AWT propeller [22] as an example. The information about the rotor geometry will be input in the *blade geometry* input file described in the next section. Figure 2.4 shows a section of the *2D airfoil section data* input file. On the first line, the value is the number of airfoil sections used in the airfoil table calculation, which always includes the cutout and the tip sections.

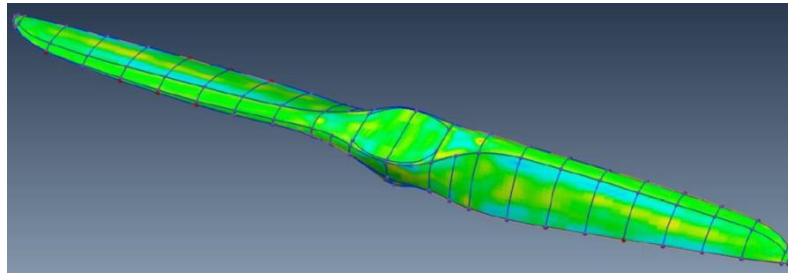


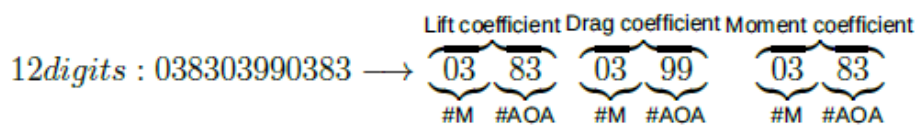
**Figure 2.3:** Location of several airfoil station through the propeller [22]

The second value indicates an absence or presence of the thickness profiles of the airfoils. Since this value is zero, the maximum thickness is provided through the *THICKN* parameter. The third parameter provides an option to apply Reynolds number corrections. The manner of Reynolds number correction associated with a value of 2 is described in Figure 2.4. On the second line, five radial positions along the blade span are input, and the third line presents the airfoil thickness as a fraction of the chord. The following line shows the radial location of the airfoil section  $r/R$ . In Figure 2.4, the first airfoil section is shown. The next line is the Reynolds number associated with the data being provided for this airfoil, and the second number is the Reynolds scaling factor, which according to the CHARM user's manual, can be set to 0.2. The Reynolds number at the radial station will vary with flight condition, which CHARM will correct for it from the table values.

The Reynolds number is a dimensionless ratio of the inertial to viscous forces in a fluid, as shown in Equation 2.4, where  $\rho$  is the fluid density,  $V$  is the velocity of the fluid,  $L$  is the characteristic length, and  $\mu$  is the dynamic viscosity of the fluid.

$$Re = \frac{\rho VL}{\mu} \quad (2.4)$$

Each airfoil table has a separate header that represents the number of Mach and angle of attack entries for each of the aerodynamic coefficients. The header is 12 digits. The first four digits belong to the lift coefficients; the second four numbers present the drag coefficients, and the last four digits belong to the coefficients of the moment. In every four digits, the first two are the number Mach (M) entries, and the second two digits are the number of angle of attack (AOA) entries.





The first horizontal line of each airfoil table are Mach numbers, and the first column from the left (after the Mach number row) are angle of attack values.

	4	0	2	
	0.0	0.191	0.721	1.0
	0.221	0.78	0.089	0.056
Re# at current radial station	r/R = 0.0			
	26565	0.2	Re# scaling factor	
	roR 0.191			383 399 383
AOA [Degree]	0.0000	0.1000	1.0000	Mach#
	-180.00	0.0000	0.0000	0.0000
	-172.50	0.7800	0.7800	0.7800
	-161.00	0.6200	0.6200	0.6200
	▪			▪
	▪			▪
	▪			▪
	▪			▪
	▪			▪
	▪			▪
	▪			▪
	161.00			
	172.50			
	180.00			

Figure 2.4: An example of 2D airfoil section data input file

### 2.2.2. Blade Geometry Input File

The *blade geometry* input file has information about the blade dimensions, such as the chord length, thickness, and twist angles. CHARM uses some of the *blade geometry* information to calculate the blade section lift, moment, and aerodynamic loads using the vortex lattice method [16]. Figure 2.9 shows an example of the *blade geometry* input files.

The first parameter on the *blade geometry* input file is *NSEG*. *NSEG* is the number of blade segments. If the rotor was built out of one airfoil through its span, one segment would be enough to describe the rotor. The root cutout, *CUTOUT*, is the distance between the hub axis and the blade root. Usually, the first airfoil station will measure at inboard  $10 - 20\% \frac{r}{R}$  to account for the inboard, non-lifting portion of the rotor

blade (the stall region of the blade). Each segment length is input as a  $SL$  value. The summation of all segment's length, in addition to the cutout length, should come to the total radius of the rotor, depicted in Equation 2.5.

$$R = \sum_{n=1}^{NSEG} SL + CUTOUT \quad (2.5)$$

The chord length for each airfoil station is recorded in  $CHORD$ , and the last value is the chord length of the blade tip. The elastic axis offset,  $ELOFSG$ , is measured from the 1/4 chord towards the trailing edge, and it is reported as a fraction of chord length [23], Figure 2.5. The  $ELOFSF$  parameter will be set to zero if no information is available about the elastic axis.

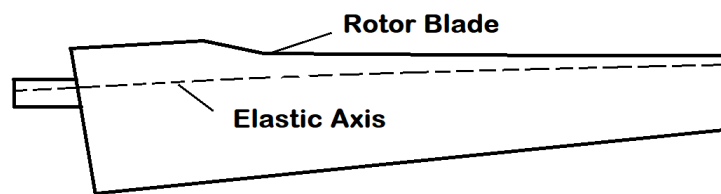


**Figure 2.5:** The elastic axis on the V-22 rotor blade

The sweep angle,  $SWEEP$ , is the angle between the quarter chord line and the chord [25], Figure 2.6. The  $TWRD$  value is the twist angle of the cutout at zero collective pitch. The twist angle of each segment  $TWSTGD$  will be measured relative to the last segment's twist angle.

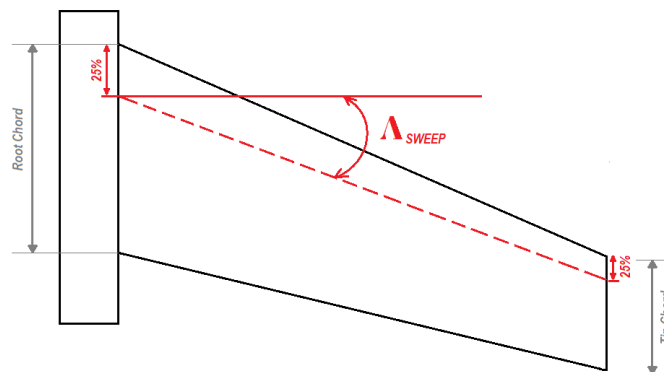


**Figure 2.6:** The sweep angle

The  $ANHD$  parameter is the anhedral droop degree for each segment. The anhedral angle allows for a greater roll capability. Figure 2.7 shows the difference

between the anhedral and dihedral angles. The *THCKND* parameter is the root and tip blade thickness as a fraction of the chord length.

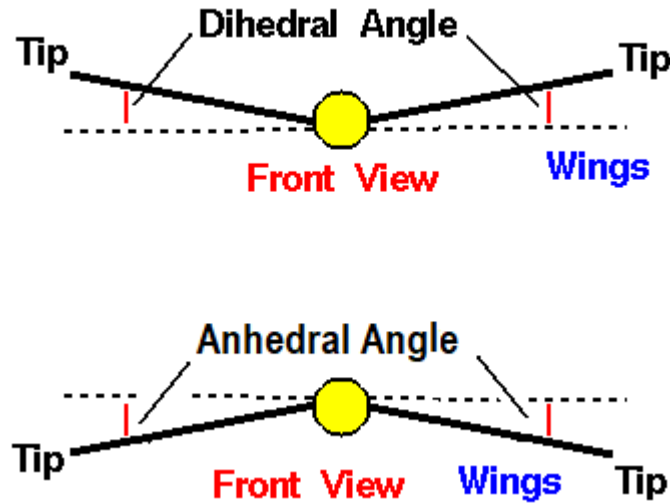


**Figure 2.7:** Anhedral and dihedral angles [26]

*KFLAP* indicates the presence of flaps, as shown in Figure 2.8.  $KFLAP = 1$  for plain flap, and for split flaps  $KFLAP = 2$ ; in the example (Figure 2.9),  $KFLAP = 0$  indicates no flaps exist in any of the segments. For an aircraft, flaps can reduce the stall speed and provide better control during takeoff and landing due to the associated camber increase leading to the increased total airfoil area. The *FLAPND*, *FLHINGE*, and *FLDEFL* parameters are used to define the segment's flap length, flap hinge offset, and deflection of the segment [9, 27].

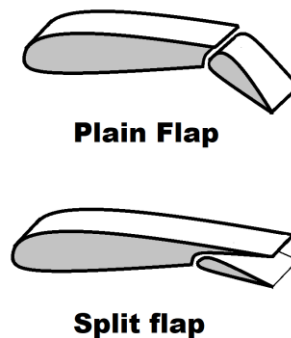


**Figure 2.8:** The plane flap versus split flap

The *NCAM* parameter shows the number of chordwise positions where camber is defined. For the simulations in this report  $NCAM = 0$  since no camber profile was provided. CHARM users can set up the vortex lattice method using the

*NCHORD*, *NSPAN*, and *ICOS* parameters. The *NCHORD* and *NSPAN* parameters control the number of vortex lattice panels chordwise and spanwise respectively. The *ICOS* value controls the vortex lattice layout schemes [9]. *ICOS* = -1 indicates auto spacing for the vortex lattice layout scheme.

```

NSEG
 1
CUTOUT
 0.7200
SL(ISEG)
 2.880
CHORD(ISEG)
 0.6000      0.6000
ELOFSG(ISEG) - (elastic axis offset)
 0.000      0.000
SWEEP(ISEG)
 0.000
TWRD (Blade root twist at zero collective in degrees)
 11.00
TWSTGD(ISEG)
 -16.00
ANHD(ISEG)
 0.000
THIKND(ISEG)
 0.1200      0.1200
KFLAP(ISEG)
 0
FLAPND(ISEG)
 0.0000
FLHNGE(ISEG)
 0.0000
FLDEFL(ISEG)
 0.000
NCAM
 0
NCHORD  NSPAN  ICOS
 1       50    -1

```

**Figure 2.9:** An example of *blade geometry* input file

### 2.2.3. Blade Dynamics Input File

The *blade dynamics* input file carries information about hinge type, hinge location, structural modes, and blade natural frequency. A user with a strong background and understanding of structural mode shapes should modify the *blade dynamics* input files, Figure 2.10. Without that background, the files should be reserved as recommended by prior user expertise. In the case for this study,

the *blade dynamics* input files were taken as in the CHARM tutorial under DESIGN directory.

```

rigidpropbd.inp: Blade Dynamics Input File: rigid blade
ISTRM
  0
ISTRIP IFPC IAERO
-1     0     1
ICOMP  IRVFLO ISTFLO
  1     0     1
IART   HINGE
  1   0.140
NMODE
  1
NMDFLP NMDTOR NMDLAG NMDELG
  1     0     0     0
IFXMDE  IRIGID
  0     1
FREQMD  GMASS      for Mode 1
  1.115  0.2510
NRBARS
  51
RBARS(IR), IR=1,NRBARS
  0.000  0.020  0.040  0.060  0.080  0.100  0.120  0.140  0.160  0.180
  0.200  0.220  0.240  0.260  0.280  0.300  0.320  0.340  0.360  0.380
  0.400  0.420  0.440  0.460  0.480  0.500  0.520  0.540  0.560  0.580
  0.600  0.620  0.640  0.660  0.680  0.700  0.720  0.740  0.760  0.780
  0.800  0.820  0.840  0.860  0.880  0.900  0.920  0.940  0.960  0.980
  1.000
Rigid flap mode
  0.000  0.000  0.000  0.000  0.000  0.000  0.000  0.000  0.000  0.000
  0.000  0.000  0.000  0.000  0.000  0.000  0.000  0.000  0.000  0.000
  0.000  0.000  0.000  0.000  0.000  0.000  0.000  0.000  0.000  0.000
  0.000  0.000  0.000  0.000  0.000  0.000  0.000  0.000  0.000  0.000
  0.000
  0.000  0.000  0.000  0.000  0.000  0.000  0.000  0.000  0.000  0.000
  0.000  0.000  0.000  0.000  0.000  0.000  0.000  0.000  0.000  0.000
  0.000  0.000  0.000  0.000  0.000  0.000  0.000  0.000  0.000  0.000
  0.000  0.000  0.000  0.000  0.000  0.000  0.000  0.000  0.000  0.000
  0.000  0.000  0.000  0.000  0.000  0.000  0.000  0.000  0.000  0.000
  0.000  0.000  0.000  0.000  0.000  0.000  0.000  0.000  0.084  0.167
  0.251  0.335  0.419  0.502  0.586  0.670  0.753  0.837  0.921  1.005
  1.088  1.172  1.256  1.340  1.423  1.507  1.591  1.674  1.758  1.842
  1.926  2.009  2.093  2.177  2.260  2.344  2.428  2.512  2.595  2.679
  2.763  2.847  2.930  3.014  3.098  3.181  3.265  3.349  3.433  3.516

```

**Figure 2.10:** A *blade dynamics* input file from CHARM tutorial

*ISTRM* presents the structural mode input, where setting  $ISTRM = 0$  means the natural frequency, and mode shapes are provided at the end of the *blade dynamics* input file. CHARM users have the option to choose the CHARM software internal calculation for modal analysis using the finite element method [28]. In this report  $ISTRM \neq 0$  and an additional input file, called the *blade cross section* input file, is provided containing the blade structural properties such as mass and stiffness. *ISTRIP* indicates the vortex lattice method is being used. When  $ISTRIP = 0$ , initial strip theory [29] is used to

define the blade motion, and  $ISTRIP \neq 0$  avoids the initial calculation. The  $IFPC$  parameter allows the user to select between harmonic Analysis, 2nd order predictor-corrector, 2nd order Adams-Bashforth, simple, and harmonic time step schemes to calculate the *blade dynamics*. In this study, the *blade dynamics* are solved in frequency space using the harmonic analysis solution,  $IFPC = 0$ . The  $IAERO$  parameters select the aerodynamic model. In this report, all simulations used the lifting surface vortex lattice method [30],  $IAERO = 1$ , with 2D lookup tables to recover the lift curve and zero lift angle.  $ICOMP = 0$  means that an incompressible calculation was used. However,  $ICOMP = 1$  indicates that a compressibility correction is applied by multiplying the vortex lattice equation coefficients by the amplitude of the rigid flapping mode,  $\beta$ . The amplitude of the rigid flapping mode was calculated using Equation 2.6, where  $M$  is Mach number.

$$\beta = \sqrt{\frac{1}{1-M^2}} \quad (2.6)$$

$IRVFLO = 0$  controls the reverse flow air loads.  $IRVFLO = 0$  is used when the advance ratio  $\mu$  in the shaft frame is less than 0.5, so the reverse flow air loads are disregarded. The advance ratio in the shaft reference frame can be determined using Equation 2.7, where  $ADV$  is the advance ratio, and  $\alpha_s$  is the shaft angle. The advance ratio,  $ADV$ , is related to the forward speed  $V$ , rotational speed  $\Omega$ , and the rotor radius  $R$ . When  $IRVFLO = 1$ , lifting line theory is used to determine the air loads in reverse flow [31].

$$\mu = ADV \cos(\alpha_s) \quad (2.7)$$

$$ADV = \frac{V}{\Omega R} \quad (2.8)$$

The  $ISTFLO$  parameter indicates the presence or absence of the stall correction.  $IART$  indicates the hinge type. For a hingeless blade,  $IART = 0$ , and for an articulated blade  $IART = 1$ . An articulated blade system can flap, feather, lead, and lag independently from other blades [32]. The feather describes the blade motion around the pitch axes, as seen in Figure 2.11. The leading and

lagging is the rotor moving back and forth from its radial position in the disk plane [34], as indicated in Figure 2.13. The flapping is the blade moving up and down with respect to flap hinge  $\beta$  axes [33], as seen in Figure 2.12.

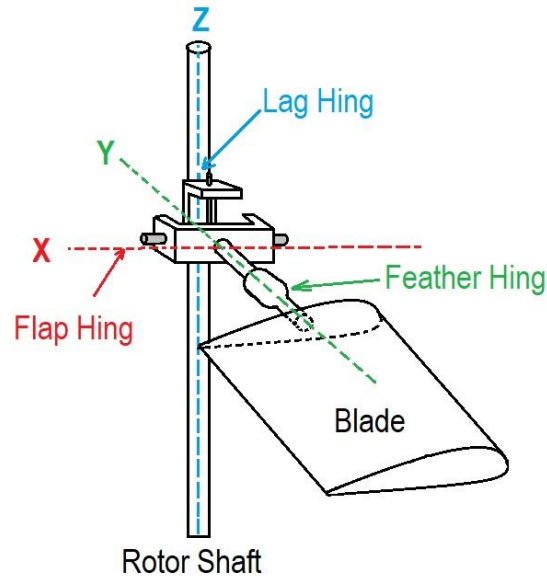


**Figure 2.11:** The main rotor's hub and hinge system

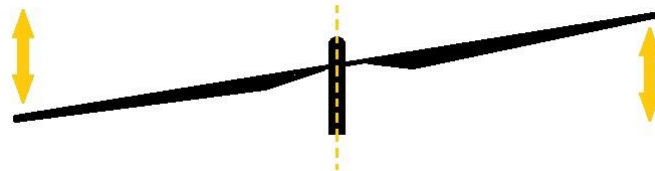


**Figure 2.12:** The blade flapping

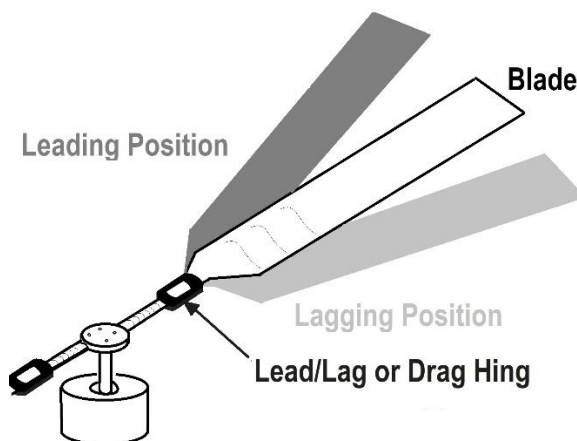


**Figure 2.13:** Leading and lagging in fully articulated rotor blade

The *HINGE* parameter presents the position of the hinge from the hub, which has been normalized by the rotor radius and is input as a radial percentage. *NMODE* indicates the structural mode number used to calculate the *blade dynamics*. The

type of frequency modes can be input through *NMDFLP*, *NMDTOR*, *NMDLAG*, and *NMDELG* [9]. The rest of the *blade dynamics* input file parameters are unchanged due to the lack of information about the rotor frequency modes.

## 2.2.4. Rotor Wake Input File

The *rotor/wake* input file provides information about the rotor system, such as the number of blades, RPM, rotation direction, solidity, collective, pitch, and shaft angle to define the wake model. Note that an individual *rotor/wake* input file is required for each rotor in a multirotor configuration due to different rotation directions and positions. Figure 2.17 shows the *rotor/wake* input files for a hover case.

The parameter *NBLADE* indicates the number of blades in the rotor system. *OMEGA* is the rotor angular velocity. The solidity value, *SOLIDITY*, represented by  $\sigma$  can be calculated and input using Equation 2.9, where  $N$  is the number of blades,  $C$  is the chord length, and  $R$  is the radius of the rotor.

$$\text{Solidity} : \sigma = \frac{Nc}{\pi R} \quad (2.9)$$

The rotation direction can be input as *IROTAT* = 1 for counter-clockwise and *IROTAT* = -1 for clockwise rotation. The *XROT OR* parameter defines the rotor position using three-axis Cartesian. The rotor orientation is defined with the  $X$ ,  $Y$ ,  $Z$  *tilt* parameters in the  $X - Y$  plane. *ITILT* = 1 allows lateral tilt to be applied. Collective adjustments can be applied using the *ICOLL* parameter. In this report, *ICOLL* = 0 and *ICOLL* = 1 will be used. *ICOLL* = 0 shows that the collective is fixed at the initial collective angle, and *ICOLL* = 1 indicates the collective value will be adjusted to the thrust coefficient,  $C_T$ . The *COLL* value is the initial collective pitch in degree (angle). The  $C_T$  parameter is the initial thrust coefficient, which can be calculated using Equation 2.10 where  $T$  is thrust,  $\rho$  is the air density,  $R$  is the rotor radius, and  $\Omega$  is the rotational speed.

$$C_T = \frac{T}{\rho \pi R^2 (\Omega R)^2} \quad (2.10)$$

Note that the rotor angles can change the angle of attack and the pitch angle; therefore, the thrust and drag can be controlled and influenced at some level.



Figure 2.14 shows the tilt angle, shaft angle, and collective angle [34]. The tilt angle is the angle that an individual rotor disk makes with an imaginary vertical line that goes to the rotor center at zero-degree shaft angle. This research is not focused on the effects of tilt angle.

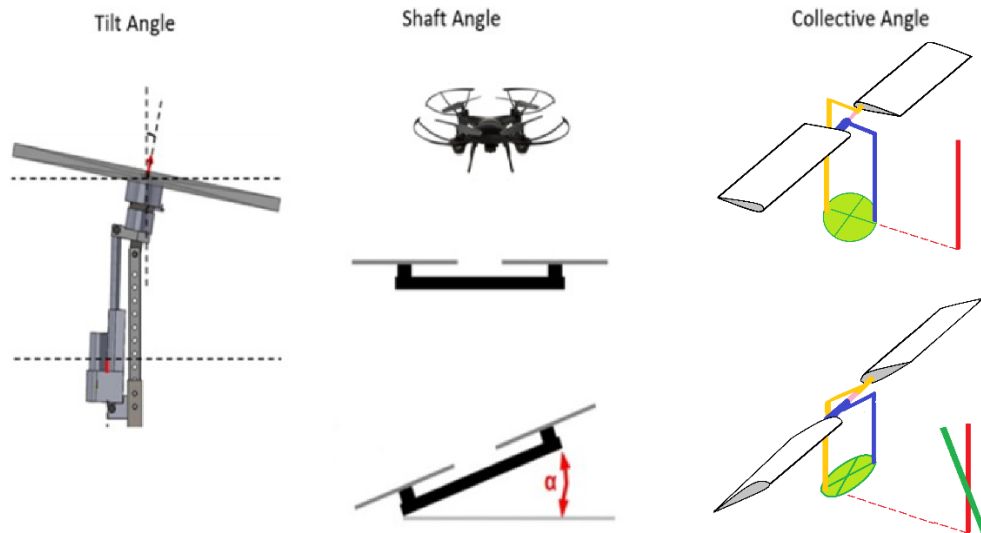


**Figure 2.14:** Tilt, shaft, and collective angles

The shaft angle can be defined as the pitch angle of the vehicle. In wind tunnel testing, the aircraft or rotor is connected to a shaft, and by changing the shaft angle, the whole aircraft will change direction; therefore, the angle of attack for all rotor disks is affected, Figure 2.15. This variable will be studied in this research. Last but not least is the collective angle, which changes the pitch angle of the blades simultaneously. The collective angle does not change the disk angle but changes the rotor blade pitch angle.



**Figure 2.15:** UH-60A airloads rotor in the 40- by 80-Foot Wind Tunnel at Ames Research Center (ARC) [35]

For the purpose of this study, the cyclic pitch input  $ITRIM = 0$  keeps the cyclic pitch fixed, therefore, all the  $ITRIM$  inputs,  $A1W, B1W, A1S, B1S$  will be set to zero. The parameter  $NOWAKE = 0$  indicates a free wake calculation is being used [9].  $ICNVCT = 0$  means the wake geometry has been calculated including induced velocity.  $ICNVCT = 1$  shows the upstream, or  $ICNVCT = 2$  shows the downstream, as part of the wake geometry calculation. The parameter  $NWAKE = 1$  shows the wake-on-wake induced velocity between the wake of different blades is considered, and  $NWAKE = 0$  means this calculation is omitted. The  $NPWAKE$  parameter indicates the number of wake turns trailing from the free wake, and the  $IFAR$  parameter shows the presence or absence of far wake calculation, as shown in Figure 2.16 [37-39].

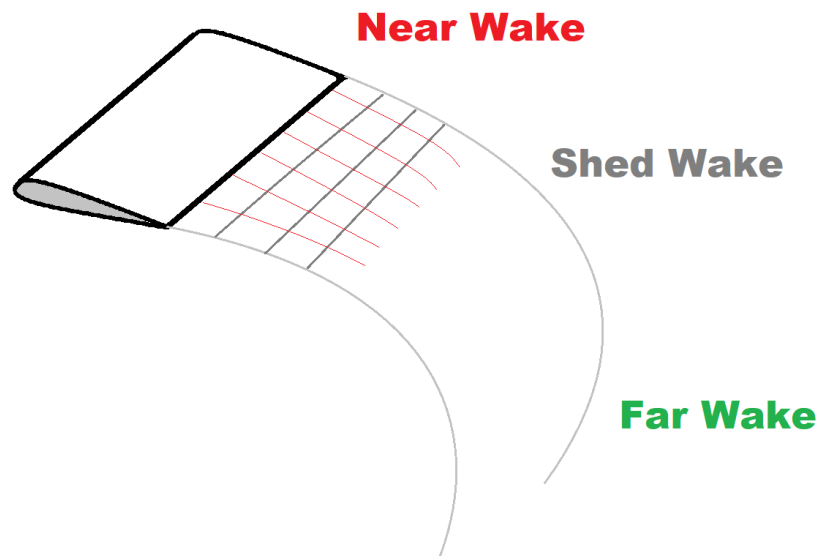


**Figure 2.16:** Schematic of free wake model

$MBCVE = 0$  it shows that basic curved vortex elements are being used to evaluate near-field wake induced velocities [9]. The  $KSCHEME$  and  $KPC$  parameters describe the scheme calculation, and the parameter  $KSCHEME = 0$  and  $KPC = 0$  indicate the use of a default backward step and a single step iteration method [39]. The rest of the *rotor/wake* input file settings stay the same as the CHARM User's Manual recommends to leave these as default settings but provides details if modifications are necessary.

```

hoverrw.inp: Rotor/Wake Input File for hover performance
NBLADE OMEGA
  2 138.89
IROTAT XROTOR X,Y,Z tilt ITILT
  1 0.0 0.0 0.0 0.0 0.0 0.0 1
ICOLL COLL CT
  1 10.0 0.01
ITRIM A1W B1W A1S B1S
  0 0.0 0.0 0.0 0.0
NOWAKE ICNVCT NWAKES NPWAKE IFAR MBCVE
  0 0 1 1 1 0
KSCHEME KPC
  0 0
NCUT AOV LAP ISKEW IUNS
  1 -1.0 1 1
NZONE (NVORT(I), I=1,NZONE)
  3 20 20 2
ICORE AKINEM A1 PCOREM CRMON
  1 0.0 0.0005 0.0 0.0
(NPTFW(I), I=1,NZONE)
  48 48 72
CORLIM Zone 1 Min core radii
  .01
CORLIM Zone 1 Max core radii
  1.0
CORLIM Zone 2 Min core radii
  .01
CORLIM Zone 2 Max core radii
  1.0
CORLIM Zone 3 Min core radii
  0.1
CORLIM Zone 3 Max core radii
  0.1
CUTLIM Zone 1 Min cutoff distance
  .01
CUTLIM Zone 1 Max cutoff distance
  1.0
CUTLIM Zone 2 Min cutoff distance
  .01
CUTLIM Zone 2 Max cutoff distance
  1.0
CUTLIM Zone 3 Min cutoff distance
  0.1
CUTLIM Zone 3 Max cutoff distance
  0.1
IDYNM
  1
SRAD SHGHT
  0.0 0.0
NHHI (Higher harmonic cyclic pitch input flag)
  0

```

**Figure 2.17:** A rotor/wake input file from CHARM tutorial

## 2.2.5. Run Characteristics Input File

The *run characteristics* input file calls all four input files and contains information such as air density, speed of sound, air velocity, presence of the ground, and an overall simulation description related to the flight condition. Figure 2.18 shows the *run characteristics* input file for a single prop in hover.

```

UH60rc.inp: Run Characteristics Input File for UH60 hover
calculations using @submitlots
NROTOR
  1
PATHNAME
../
INPUT FILENAMES for UH60 main rotor
UH60rw.inp
UH60bg.inp
UH60bd.inp
UH60af.inp
none
SSPD      RHO
1116.0    .002377
SFRAME
  0
ADV      ALPHAS
0.0      0.0
NPSI     NREV      CONVG1      CONVG2      CONVG3      MREV
  24      200      -1.0        -1.0        -1.0        0
IRST     IFREE     IGPR
  0        0        1
IOUT     NRS      (ROUT(I),I=1,NRS)
  4        8      0.3  0.4  0.5  0.6  0.7  0.8  0.9  0.95
NPRINT   IBLPLT   (IFILPLT(I),I=1,4)
  0        0        3  3  3  3
IDEBUG (Debug flag)
  0
ISCAN (Scan plane flag)
  0
ISTRSS (Stress calculation flag)
  0
IFV      IQUIK1
  2        1
IFVFLGS
  1  1  1  1  1
ISURF
  0
ISHIP
  0
IRECON   NOISE
  0        0
NLS
  0

```

**Figure 2.18:** A *run characteristics* input file from CHARM tutorial

On the first line, parameter NROTOR represents the number of rotors in the system. In this case, one rotor is being simulated. CHARM reports results in the US customary system (USCS) by default, but adding the parameter IMKS=1 after the

rotor NROTOR number allows a unit change to the International System (SI). The following lines will call the input files, followed by the speed of sound (SSPD) and the air density (RHO). Parameters such as air density from the *run characteristics* input files and rotors disk area from the *blade geometry* input files are required to calculate the rotor coefficients, depicted in equations 2.11, 2.12, 2.13, 2.14.

$$C_T = \frac{T}{\rho A (\Omega R)^2} \quad (2.11)$$

$$C_D = \frac{D}{\rho A (\Omega R)^2} \quad (2.12)$$

$$C_Q = \frac{Q}{\rho A (\Omega R)^2 R} \quad (2.13)$$

$$C_P = \frac{P}{\rho A (\Omega R)^3} \quad (2.14)$$

Where  $C_T$  is thrust coefficient,  $C_D$  is drag coefficient,  $C_Q$  is torque coefficient,  $C_P$  is power coefficient,  $\rho$  is air density,  $A$  is disk area,  $\Omega$  is rotor rotational speed,  $R$  is rotor radius,  $T$  is thrust,  $D$  is drag,  $Q$  is torque, and  $P$  is power. Note that  $\Omega R$  is the rotor tip speed [41]. The next line holds and calls all the input files. Each rotor requires a separate input filename section. The *SSPD* and *RHO* present the speed of sound and air density at sea level. *SFRAME* = 0 indicates that the calculation is being done in the rotor reference frame, and when *SFRAME* = 1 the reference frame switches to the aircraft body. *ADV* is the advance ratio, and *ALPHAS* is the shaft angle of attack, as shown in Figure 2.19.

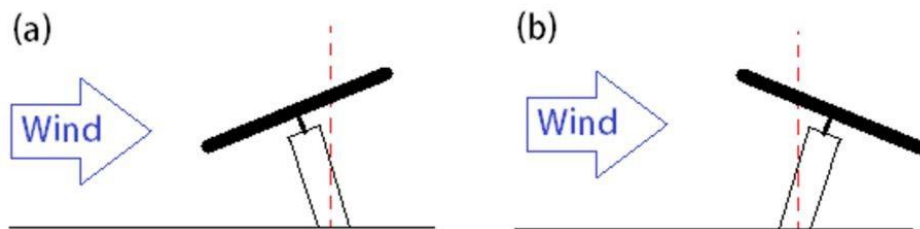


**Figure 2.19:** Shows (a) positive shaft angle and (b) negative shaft angle

The *NPSI* parameter presents the number of azimuth locations per blade revolution, and *NREV* shows the maximum number of blade revolutions used in the trim solution. The parameters *CONVG1*, *CONVG2*, and *CONVG3* set the convergence criteria for CHARM until the maximum number of blade revolutions is satisfied.

The *MREV* parameter indicates the time marching revolution number after the initial *NREV*. Setting *IRST* = 0 allows for the wake geometry using convection and a simple inflow model, and when *IRST* = 1, this information is extracted from the Wake Geometry Output file. *IFREE* = 0 allows the usage of the initial free wake velocity and wake geometry settings and *IFREE* = 1 indicates that a separate file with this information will be provided. The *IGPR* parameter describes the flight type and calculation; for hover *IGPR* = 0 and at forward flight *IGPR* = 1. The *IOUT* or *IVOOUT* parameter allows the user to choose the desired output at each azimuth. For this study, *IOUT* = 0 indicates no output and *IOUT* = 1 means upwash output were used. It is recommended by the CHARM manual to keep *NPRINT* = 0, and *IBLPLT* = 0 to exclude excessive wake printout into the wake geometry output file and allow for normal operation. *ISCAN* = 1 indicates the presence of the *scan* input file, *scan.inp*. The *scan* input file uses grid points to measure the pressure and velocity at each location. *ISTRSS* = 0 indicates the absence of the stress calculation for the blade. The *IFV* parameter allows the user to choose between the Hierarchical Fast Vortex method with the reduced order method for wake calculation *IFV* = 1, Hierarchical Fast Vortex method with the default setting *IFV* = 2, and *IFV* = 0 for no Fast Vortex method in wake calculation. The Hierarchical Fast Vortex method draws a box around the vortex area and allows for calculations where the vortex elements are. *IQUIK1* = 1 allows the vortex lattice method to influence coefficients evaluation once for each *blade dynamics* calculation, and *IQUIK1* = 0 re-evaluates this coefficient at the beginning of each *blade dynamics* calculation. The *IFVFLGS* or *IFVFW*, *IFVBL*, *IFVSU*, *IFVSC*, *IFVLS* define the wake calculation on wake, blade, surface, and lifting surface, Table 2.2. A value of 1 for these parameters indicates the presence of a wake calculation, while a value of 0 indicates a lack of the calculation for the wake.

*ISURF* = 1 indicates that a surface panel calculation is required due to the presence of a wind tunnel, fuselage, or any structure. The *ISHIP* parameter is only used when a ship airwake model is required. *IRECON* allows for reconstructing the wake geometry to increase the resolution of the calculation [9]. The *NOISE* parameter shows the presence of the surface pressure calculation for acoustic output. Note that the unsteady Bernoulli equation can calculate the unsteady surface pressure.

**Table 2.2:** IFVFLGS setting for wake calculation

Parameter	Hierarchical Fast Vortex for
$IFVFW = 1$	wake-on-wake
$IFVBL = 1$	wake-on-blade
$IFVSU = 1$	wake-on-surface
$IFVSC = 1$	wake-on-scan grid
$IFVLS = 1$	wake-on-lifting surface

$$C_p = 1 - \frac{V^2}{U_\infty^2} - \frac{2}{U_\infty^2} \frac{\partial \phi}{\partial t} \quad (2.15)$$

The contribution comes from the blade, wake, and panels. The  $V^2/U_\infty^2$  is the steady term, and the  $2\partial\phi/U_\infty^2 \partial t$  is the unsteady term. In this report,  $NOISE = 0$  is used to eliminate the surface pressure calculation and  $NOISE = 1$  is used to indicate the pressure distribution versus the azimuth file. The last parameter in the *run characteristics* input file is *NLS*, allowing additional lifting surface calculation in the presence of the wing or body using the vortex lattice method.

### 2.3. Output Files

The CHARM result appears in a separate text file, and most of the output files have one of *.dat*, *.out*, *.off*, or *.prt* file extension. For this study, the numerical simulation results presented are from two output files *[NAME]sweep.dat* and *[NAME].off*. The *[NAME]sweep.dat* file contains information such as thrust, power, figure of merit, advance ratio, and shaft angle, as seen in Figure 2.20. From the sweep data file, the figure of merit, thrust, and power was extracted.



ADV	SHAFT	COLL	ALS	BIS	CONING	CT	als
bls	CL/S	CD/S	CX/S	CT/S	CH/S		
CY/S	CQ/S	Cde/S	FM	V	a (wt)	CT (wt)	
CP (wt)	ETA	ALMDhub	ALMDtpp	ALMDnfp	ALMDi	ALMD1C	ALMD1S
THRUST	POWER						
0.0000	0.00	0.00	0.00	0.00	0.00	0.01468	0.00
0.00	0.137746	0.000000	0.000000	0.000000	0.137746	0.001504	
0.000765	0.014389	0.000000	0.822	0.0	0.00	0.00	
0.00	0.0000	0.0838	0.0838	0.0838	0.0838	0.0000	0.0000
4.99	0.200						

Figure 2.20: [NAME]sweep.dat output file example

The [NAME].off output file contains information related to the wake velocity at each point indicated in the user's scan input file, scan.inp. The results in the [NAME].off output file come in eight columns. Figure 2.21 shows the output information from the [NAME].off output file. The first three columns respectively show the location of points at X, Y, and Z axis. The second set of three columns present the velocity components U, V, and W. The last two columns are the pressure coefficient and the surface pressure coefficient. The velocity component from the [NAME].off output file can be used for the outwash study.

1	36	95	(U, V, W)			C <sub>P</sub>	C' <sub>P</sub>
48	(X, Y, Z)						
0.0000							
0.000	-8.300	0.000	-0.4539E-01	-0.1739E-01	-0.3635E-01	0.000	-0.2925E-02
0.000	-8.100	0.000	-0.4713E-01	-0.1785E-01	-0.3993E-01	0.000	-0.3212E-02
0.000	-7.900	0.000	-0.4897E-01	-0.1822E-01	-0.4392E-01	0.000	-0.3531E-02
0.000	-7.700	0.000	-0.5090E-01	-0.1847E-01	-0.4835E-01	0.000	-0.3886E-02
0.000	-7.500	0.000	-0.5294E-01	-0.1855E-01	-0.5328E-01	0.000	-0.4281E-02
0.000	-7.300	0.000	-0.5510E-01	-0.1843E-01	-0.5878E-01	0.000	-0.4720E-02

Figure 2.21: [NAME].off output file example

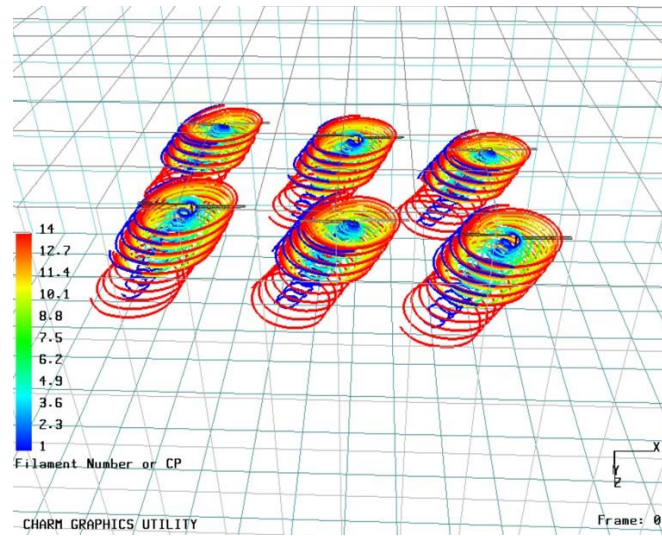
## 2.4. Vortex-X

The CHARM solution can be presented using 3D animation software called Vortex-X. The CHARM simulation results generate two output files, [NAME].sgp.graphics and [NAME].sgp, to be used by Vortex-X. Instead of releasing one particle along the blade, Vortex-X realizes vortex elements with the same strength along the rotor span to decrease the CPU and memory usage and shorten the computation time. Note that in Vortex-X, the user will observe many vortex elements being released from the tip, but actually, these elements



release along the rotor's span. The Figure 2.22 shows an example of the kinds of visualization possible with Vortex-X software environment.

**Figure 2.22:** The simulation of MTB with six rotor in Vortex-X software



---

# CHAPTER 3

---

## CHARM Validation

In this chapter, two different rotors will be used to validate CHARM results and develop a better understanding of each parameter setting. First, a full-scale four bladed UH-60<sup>1</sup> rotor system will be simulated for the hover case, and the CHARM result will be compared with experimental data. Next, a full-scale two bladed SUI rotor will be simulated at hover and forward flight conditions in CHARM, and the result will be compared with test data. In this chapter, the figure of merit will be used as the primary comparison value to study rotor performance for both CHARM simulations and experimental data. CHARM is expected to have less accurate results for hover cases, since hover simulations are challenging due to unsteady wakes generated below the rotor blade plane. The forward flight analysis is more straightforward than the hover case because the wakes generated by the rotor will quickly convected downstream, away from the rotor by the incoming free stream flow.

### 3.1. Figure of Merit Validation Parameter

The figure of merit (FM) is a dimensionless quantity that describes the efficiency of a rotor in hover. This is also the most relevant quantity to identify the rotor performance in this research which is defined as the ratio of the minimum possible power required to the actual power used. For this study, the basic dimensionless parameters of the rotor will be used to calculate the figure of merit. First, the aerodynamic forces on the rotor needs to be modeled using momentum theory or disk actuator theory. Momentum theory can be used with the assumption

---

<sup>1</sup>Sikorsky SC1095 airfoil

of having irrotational flow and uniform flow, which means a constant distribution of aerodynamic forces on the rotor disc. Also, the rotor is assumed to be an infinitely thin disc with no friction. Besides, the rotor doesn't disturb the air outside of the stream tube, Figure 3.1.

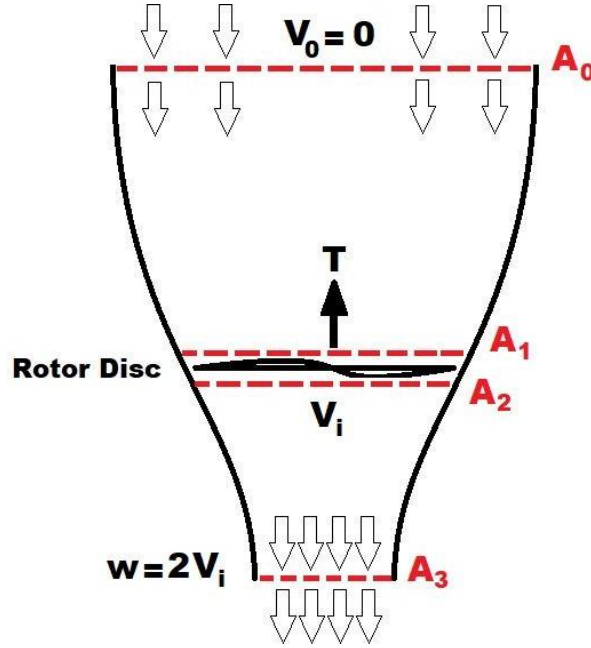


**Figure 3.1:** Streamtube at hovering flight

Momentum theory is used to calculate the thrust by Equation 3.1, where  $\rho$  is the air density,  $v_i$  is the velocity of air through the rotor,  $A$  is the rotor disc area,  $w$  is the wake velocity, and  $V_0$  is the upstream velocity. Note that at hover  $V_0$  is zero and the wake velocity is,  $w = 2v_i$ , Equation 3.2. Therefore, the induced velocity can be defined as a relation between thrust, rotor disc area, and the air density, Equation 3.3.

$$T = \rho v_i A (w - V_0) \quad (3.1)$$

$$T = \rho v_i A (2 v_i) \quad (3.2)$$

$$v_i = \sqrt{\frac{T}{2A\rho}} \quad (3.3)$$

Using momentum theory, the required power to generate the thrust can be defined with thrust and flow velocity, Equation 3.5, where  $V_0$  is the free stream velocity,  $\alpha$  is the disc angle, and  $V_\xi$  is the flow velocity at the rotor in the hub direction.  $V_\xi$  can be calculated using Equation 3.5.

$$P = T \times V_{\xi} \quad (3.4)$$

$$V_{\xi} = V_0 \sin \alpha + v_i \quad (3.5)$$

By combining Equations 3.4 and 3.5, the power can be defined as in Equation 3.6, where the  $T \sin \alpha$  is the drag force  $D$ . Therefore, the required power to generate the thrust can be defined as the summation of parasitic power and induced power, Equation 3.7. The parasitic power is the required power to overcome the fuselage drag and rotor drag when the rotor system is in forward flight, but at hover,  $V_0$  is zero, and the only term left in the equation is the induced power, Equation 3.8.

$$P = T(V_0 \sin \alpha + v_i) \quad (3.6)$$

$$P = \underbrace{DV_0}_{\text{parasitic power}} + \underbrace{Tv_i}_{\text{induced power}} \quad (3.7)$$

$$P_i = Tv_i \quad (3.8)$$

Now, using Equation 3.3, the power can be defined in relation to thrust, air density, and the rotor disk area, Equation 3.9

$$P = T \sqrt{\frac{T}{2A\rho}} \quad (3.9)$$

$$P = T \frac{T^{3/2}}{\sqrt{2A\rho}} \quad (3.10)$$

Equation 3.10 shows the power,  $P$ , required for generating the thrust. The value of  $P$  is different from the mechanical power that has been applied to the rotor shaft  $P_m$ . The mechanical power can be calculated using Equation 3.11, which

shows the relation between the rotor shaft power and torque. The mechanical power,  $P_m$ , is always higher than  $P$  (required power for thrust only) due to energy loss, such as friction (airfoil drag components).

$$P_m = \Omega \times Q \quad (3.11)$$

Recall that the normalization by rotor disk area, tip speed and air density are shown below:

$$C_T = \frac{T}{\rho A (\Omega R)^2} \quad (3.12)$$

$$C_Q = \frac{Q}{\rho A (\Omega R)^2 R} \quad (3.13)$$

$$C_P = \frac{P}{\rho A (\Omega R)^3} \quad (3.14)$$

If the torque coefficient formula and power coefficient formula are placed in Equation 3.11, shown in Equation 3.15, the result will be an equality between the power coefficient and torque coefficient, Equation 3.16.

$$\rho A (\Omega R)^3 C_P = \Omega \rho A (\Omega R)^2 R C_Q \quad (3.15)$$

$$C_P = C_Q. \quad (3.16)$$

The figure of merit is the rotor efficiency and can be defined as the ratio of the power required to generate thrust over the mechanical power, Equation 3.17. The figure of merit is therefore always less than one.

$$FM = \frac{P_i}{P_m} \quad (3.17)$$

Using Equations 3.8, and 3.11 the figure of merit can be written as:

$$FM = \frac{T v_i}{\Omega Q} \quad (3.18)$$

By Equation 3.10,

$$FM = \frac{T^{3/2} / \sqrt{2A\rho}}{\Omega Q} \quad (3.19)$$

By applying Equations 3.12 and 3.13,

$$FM = \frac{(C_T \rho A (\Omega R)^2)^{3/2}}{\sqrt{2A\rho} \Omega C_Q \rho A (\Omega R)^2 R} \quad (3.20)$$

Since  $C_p = C_Q$ , Equation 3.16, replacing  $C_q$  by  $C_p$  in Equation 3.20, the equation

for the figure of merit can be simplified. The figure of merit, which shows that the rotor hovering efficiency, can be written with dimensionless parameters, as shown in Equation 3.21.

$$FM = \frac{C_T^{\frac{3}{2}} / \sqrt{2}}{C_P} \quad (3.21)$$

### 3.2. UH-60A Performance Validation

The UH-60A rotor is used to validate the CHARM results in this section. The experimental data came from the model-scale hover testing of the UH-60A rotor at the Duits-Nederlands Windtunnel (DNW) in the Netherland [41]. Also, the full-scale UH-60A rotor system was tested in hover by the U.S. Army at the National Full-Scale Aerodynamics Complex (NFAC) wind tunnel at NASA Ames Research center, with the test setup shown in the 80- by -120 Foot Wind Tunnel in Figure 3.2. However, in this section, the CHARM results will compare to the DNW hover testing data because less recirculation effect is present in this data set. The CHARM tutorial has provided some input files under the *DESIGN* folder. Some parameter settings need to be changed from the original tutorial input files for the UH-60A rotor at hover, which will be discussed in the following sections [55-59]. To validate the CHARM results, the FM will be compared with experimental data over  $C_T$  range.



**Figure 3.2:** UH-60A rotor system at the National Full-Scale Aerodynamics Complex wind tunnel [44]

### 3.2.1. UH-60A Experiment

The experimental data came from the model-scale four-bladed UH-60A rotor testing in the DNW test section wind tunnel. A more negligible recirculation effect was present in the model-scale test data, making it a reliable data set to use for the CHARM validation. However, using the scale-model rotors requires Reynolds number correction to be applied to the simulation. Previous research has been done to study the effect of the Reynolds number correction for the UH-60A rotor [60,41]. The result showed that the SC1095 and SC1095-R8 are less sensitive to the Reynolds number changes. Therefore the DNW model-scale hover test data can be compared to the CHARM full-scale rotor simulation cases. In CHARM, the UH-60A rotor has been simulated in the free field and without ground effect. The UH-60A rotor has a 26.8-ft radius characterized by the SC1095 and 1094R8 airfoils. For the UH-60A *blade geometry* input file, the rotor is defined using 15 segments with blade root twist  $TWRD = 10$  [55]. The *bladedynamics* input files define the rotor as an articulated blade,  $IART = 1$ , where the aerodynamic model is being used with 2D lookup tables for the lift curve and zero lift angle,  $IAERO = 1$ . In the *run characteristics* input file, parameter  $IGPR = 1$  adjusts the setting for the hover case, meaning the wake is unstable and will not wash out. Also,  $ADV = 0$  accounts for no incoming free stream or wind from the wind tunnel. In the *rotor/wake* input file, the rotor rotational speed is set to  $OMEGA = 27.0$  and the  $SOLIDITY$  value has been calculated using Equation 2.9. The UH-60A rotor is a four bladed rotor,  $N=4$ , with a chord length  $C$  of 1.74 ft [41], and rotor radius  $R$  of 26.8 ft, which brings the solidity value to  $SOLIDITY = 0.0825$ . The UH-60A rotor system parameters have been listed in Table 3.1.

**Table 3.1:** UH-60A rotor parameters

Parameter	Value
Airfoils	SC1095/SC1094-R8
Chord	20.76/20.965 <i>inch</i>
Thickness, % chord	9.5/9.4
Number of blades	4
Radius of blade	26.83 <i>ft</i>
Rotor disk area	2261.5 <i>ft</i> <sup>2</sup>
Solidity ratio	0.0826
Normal rotor speed	258 <i>RPM</i>
Normal Tip Speed	725 <i>ft/sec</i>

Figure 3.3 shows the UH-60A rotor system in hover, as visualized by the CDI Vortex-X software. This simulation has been done with  $NREV = 10$  in the *run characteristics* input file to examine the rotor position and check the rotor shape before collecting data. Note that for the data collection the  $NREV$  was changed back to 200 to increase the number of blade revolutions for the solution.

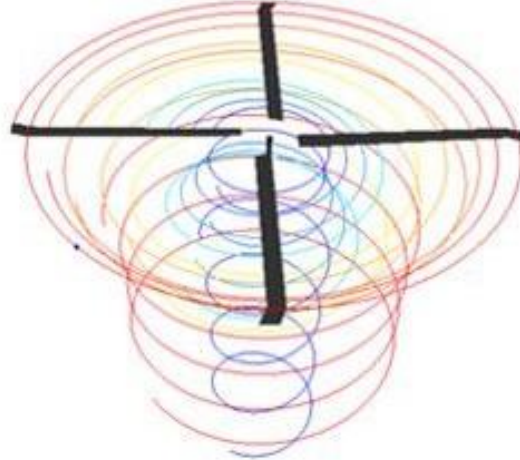


**Figure 3.3:** Vortex-X simulation of the UH-60A rotor system out of ground effect in hover

### 3.2.2. UH-60A Flight Performance

The CHARM simulation for the UH-60A rotor system was done by sweeping the  $C_T/\sigma$  range from 0.01 to 0.09 at a shaft angle of 0 degrees, which makes the angle of attack for the rotor disk  $\alpha = 0^\circ$ . Figure 3.4 provides a comparison of experimental data, CAMRADII, and CHARM results. The figure of merit for the CHARM simulation came from the *[Name]sweep.dat* output file. The discrepancy can be used to assess the difference between the simulation results and the DNW data. Equation 3.22 shows the discrepancy  $\delta$  equation, where the  $v_S$  is the simulation results and  $v_E$  is the DNW data. The results indicate that the CHARM result has an average discrepancy of 3.5% and for this data set.

$$\delta = \left| \frac{v_S - v_E}{v_E} \right| \cdot 100 \% \quad (3.22)$$

In addition, the coefficient of power output for the CHARM simulation can be found in the *[Name]rcprop.dat* output file. Figure 3.5 demonstrates the variability of  $CP/\sigma$  by increasing the  $CT/\sigma$  ratio. These results show that the current CHARM settings overpredict the thrust and underpredict the power value slightly. An additional simulation is required to examine the current settings for hover and



forward flight, but the agreement with experimental results is promising and indicates that CHARM has captured important features of the rotor performance. In the next section, the SUI rotor system will be used to study the current setting future.

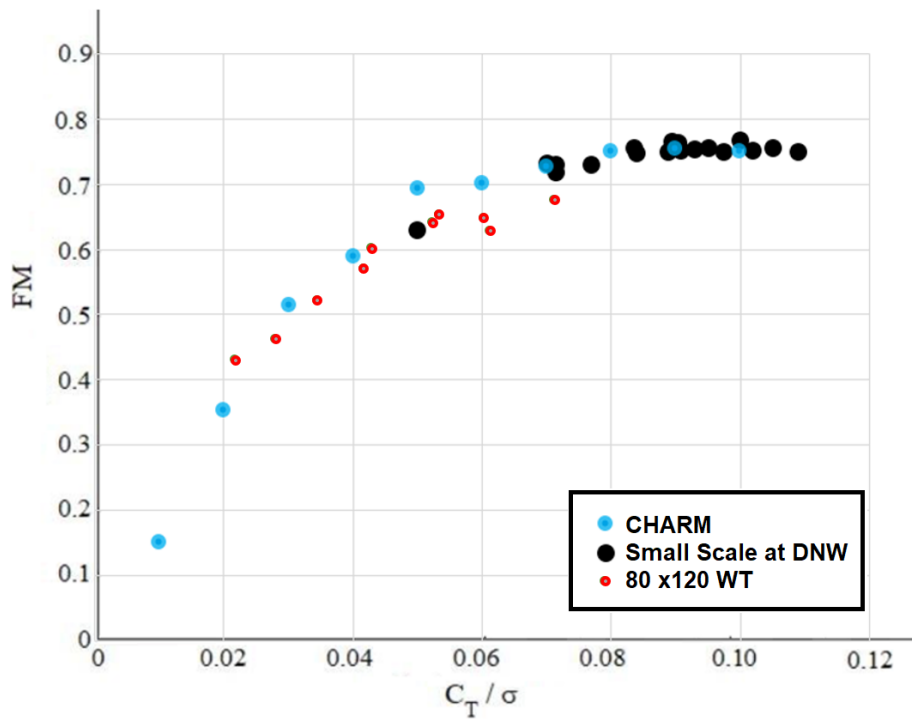


**Figure 3.4:** Figure of merit comparison for UH-60A rotor system at a 0 degrees shaft angle in hover

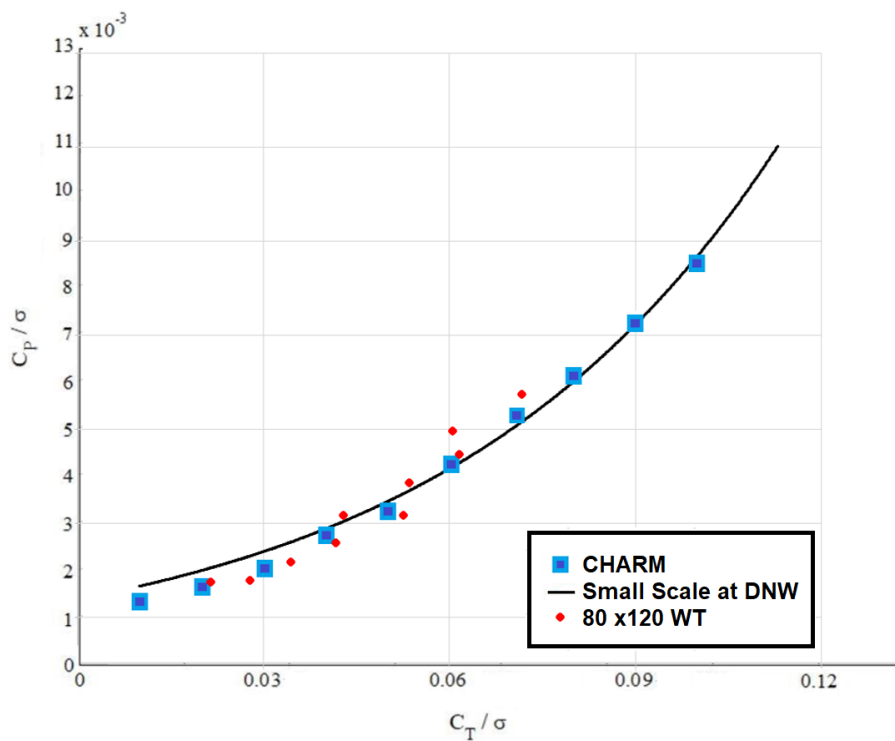


**Figure 3.5:** The power comparison of UH-60A rotor system with DNW data at a 0 degrees shaft angle in hover

### 3.3. SUI Performance Validation

In this section, the SUI rotor was used to validate CHARM results and better understand CHARM variables for hover and forward flight. The CHARM results were compared with experimental wind tunnel data and CAMRADII [7, 24, 42, 43] results for an isolated SUI rotor in forward flight in the wind tunnel and hover in the free field conditions [45]. Because CAMRADII is a comprehensive simulation, it is assumed to be the baseline quality of simulation against which CHARM results can be evaluated.

SUI was one of the rotors tested for the sUAS project in the U.S. Army 7- by 10-Foot Wind Tunnel. The SUI is an off-the-shelf rotor; therefore, a laser scanner was used to extract the blade geometry [46]. Using a scanned geometry of the blade, airfoil profiles were generated for six radial stations, six of which were used to generate airfoil tables using XFOIL [10]. These airfoil tables were later used to make the *2D airfoil section data* input file for the SUI simulation in CHARM. The base of UH-60A input files was used to set up the SUI rotor simulation with some changes in the value of the parameters, as is discussed in the following section. Figure 3.6 shows the isolated SUI rotor at the test section of the 7- by 10-Foot Wind Tunnel.



**Figure 3.6:** Hover test for the SUI isolated rotor in 7- by 10-Foot Wind Tunnel [46]

#### 3.3.1. SUI Experiment

The UH-60A input files were used as a baseline for the SUI case studies.

Some changes were necessary in each input file to define the SUI rotor and the flight conditions. The 2-bladed SUI rotor has a diameter of 1.25 ft and a design rotor RPM of 3500 RPM. Table 3.2 provides an overview of the SUI rotor parameters.

**Table 3.2:** SUI rotor parameters

Parameter	Value
Number of blades	2
Radius of blade	0.625 <i>ft</i>
Rotor disk area	1.23 <i>ft</i> <sup>2</sup>
Design rotor RPM	3500 <i>RPM</i>

The *2D airfoil section data* input file was developed by stacking six airfoil tables that was generated using XFOIL software. Table 3.3 shows the six radial positions along the blade span, the airfoil thickness as a fraction of chord length, and the Reynolds number at each radial station. The top section of the *2D airfoil section data* input file is shown in Figure 3.7. Some input files can be found in Appendix C.

**Table 3.3:** SUI rotor parameters for *2D airfoil section data* input file

r/R	t/c	Re
0.0000	0.0753	80300
0.3077	0.0753	80300
0.6282	0.0713	97000
0.7821	0.0789	93100
0.8974	0.0874	84800
1.0000	0.1015	52800

```

6 0 2
0.0 0.3077 0.6282 0.78205 0.8974 1.0
0.0753 0.0753 0.0713 0.0789 0.0874 0.1015
SC1095 at r/R = 0.0
80300 0.2
SUI045 113911650947
0.0000 0.2000 0.3000 0.4000 0.5000 0.6000 0.7000
0.7500 0.8000 0.9000 1.0000

```

**Figure 3.7:** The header of the *2D airfoil section data* input file for SUI rotor

Figure 3.8 shows the SUI rotor that was 3D scanned, and the extracted

information used to generate the *blade geometry* input files. The blade was measured at 22 radial stations with an even spacing of 0.026 ft between each section. The various airfoil profiles at 22 radial locations of the SUI rotor are shown in Appendix A, where the chord length normalizes each axis. The SUI blade geometry for these 22 sections can be found in Appendix A. For the *blade geometry* input files, 20 airfoil radial stations were used to define the rotor dimensions, presented in Table 3.4. The first radial station is defined as the cut out  $CUTOUT = 0.1292$ , and the rest of the radial stations will be spaced 0.026 ft between 19 segments,  $NSEG = 19$  and  $SL = 19 * 0.026$ . The blade root twist at zero collective angle belongs to the root cutout radial location  $TWRD = 21.77$ .

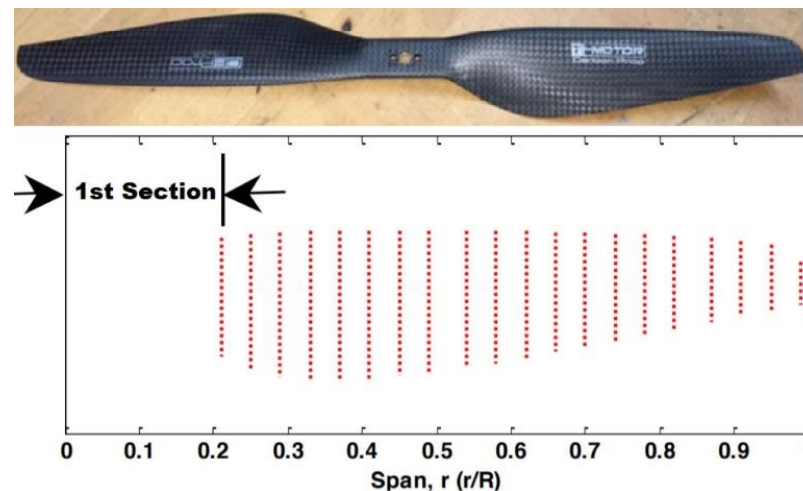


**Figure 3.8:** Axial view of SUI rotor (top), and 22 radial station segments (bottom) [46]

The values for the chord length  $CHORD$ , twist angle between each segment  $TWSTGD$ , and airfoil thickness  $THCKND$  for each section can be determined using the information in Table 3.4. The *blade dynamics* input file is almost the same as for the UH-60, with minor changes needed to describe the SUI rotor. The SUI rotor system has a hingeless blade, so  $IART = 0$  and  $HINGE = 0.0$ . Since the 2-bladed SUI rotor,  $NBLADE = 2$ , was tested at different RPM ranges, the  $OMEGA$  value was swept accordingly in the *rotor/wake* input files.

For each flight condition, different *run characteristics* input files were used to describe forward flight in the wind tunnel and at hover in the free field. Free field represents that the influence of all types of physical boundaries (including the ground) are neglected in the calculation (even though they might exist in the simulation domain) as if the rotor(s) are in an open field. To simulate the SUI isolated rotor at hover in the free field  $IGPR = 1$ , since the test is out of ground effect, and the advance ratio is  $ADV = 0$  due to the absence of free stream velocity.

For forward flight,  $IGPR = 0$  with wind tunnel speed of  $U=20$  ft/sec. To set the surface panels for the 7- by 10-Foot Wind Tunnel  $ISURF = 1$ , and the dimensions will be defined at three  $X, Y, Z$  coordinates where the center of the wind tunnel is at  $O (0, 0, 0)$ . Figure 3.9 shows a section of the *runcharacteristics* input file that defines the wind tunnel dimensions, where the 7- by 10-Foot Wind Tunnel has a 15 ft long test section. Some of the CHARM input files for both the hover case and forward flight cases can be found in Appendix C.

**Table 3.4:** SUI blade geometry distribution [47]

Section	r [ft]	r/R	Theta [Deg]	Chord [ft]	t/c %
1	0.129	0.210	21.770	0.098	11.77
2	0.155	0.250	21.720	0.112	9.76
3	0.181	0.290	19.910	0.120	8.73
4	0.206	0.330	18.140	0.124	8.18
5	0.232	0.370	16.550	0.125	7.88
6	0.258	0.410	15.280	0.124	7.72
7	0.283	0.450	14.010	0.122	7.53
8	0.309	0.490	13.000	0.118	7.38
9	0.335	0.540	12.180	0.115	7.22
10	0.361	0.580	11.390	0.111	7.11
11	0.387	0.620	10.760	0.106	7.04
12	0.413	0.660	10.240	0.101	7.07
13	0.438	0.700	9.850	0.095	7.13
14	0.464	0.740	9.400	0.089	7.26
15	0.490	0.780	9.070	0.083	7.54
16	0.516	0.820	8.700	0.078	7.89
17	0.542	0.870	8.460	0.072	8.30
18	0.568	0.910	8.290	0.064	8.74
19	0.593	0.950	8.190	0.056	8.88
20	0.618	0.990	8.170	0.037	10.15

```

XMIN   XMAX   YMIN   YMAX   ZMIN   ZMAX
-7.5   7.5   -5.0   5.0   -3.5   3.5
NX   NY   NZ   SPACE
-15  10   7   0

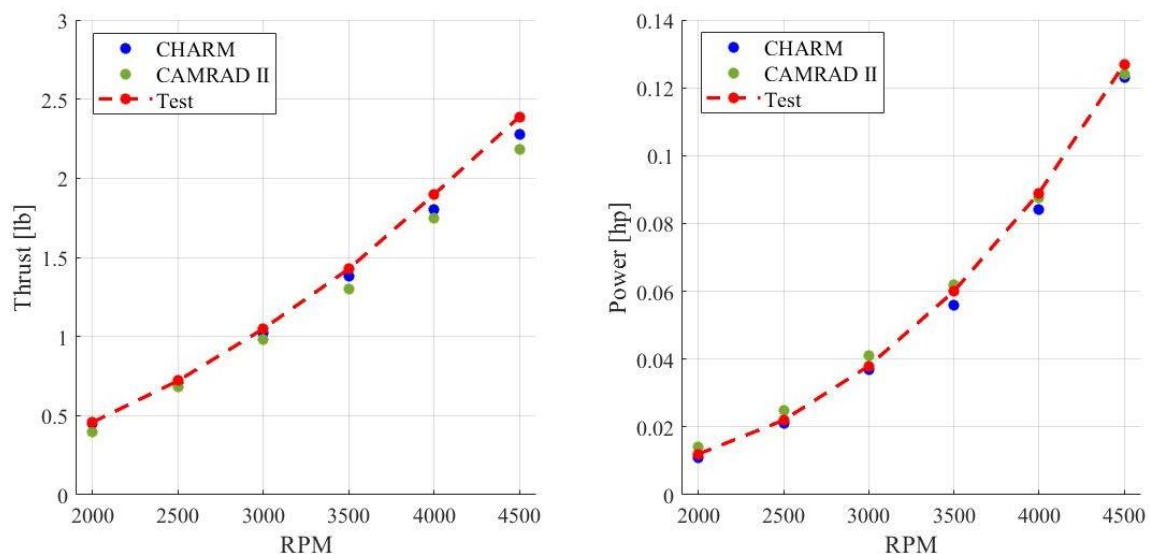
```

**Figure 3.9:** CHARM description of the 7- by 10-Foot Wind Tunnel in the *run characteristics* input file

### 3.3.2. SUI Flight Performance

The SUI rotor system was tested in hover in the Aero Lab<sup>3</sup>, where the rotor was at least five rotor radius away from the side walls, ceiling, or ground; therefore, the flight type is considered to be free field. The hover case was tested and simulated from 2000 to 4500 RPM with two different *blade geometry* input files.

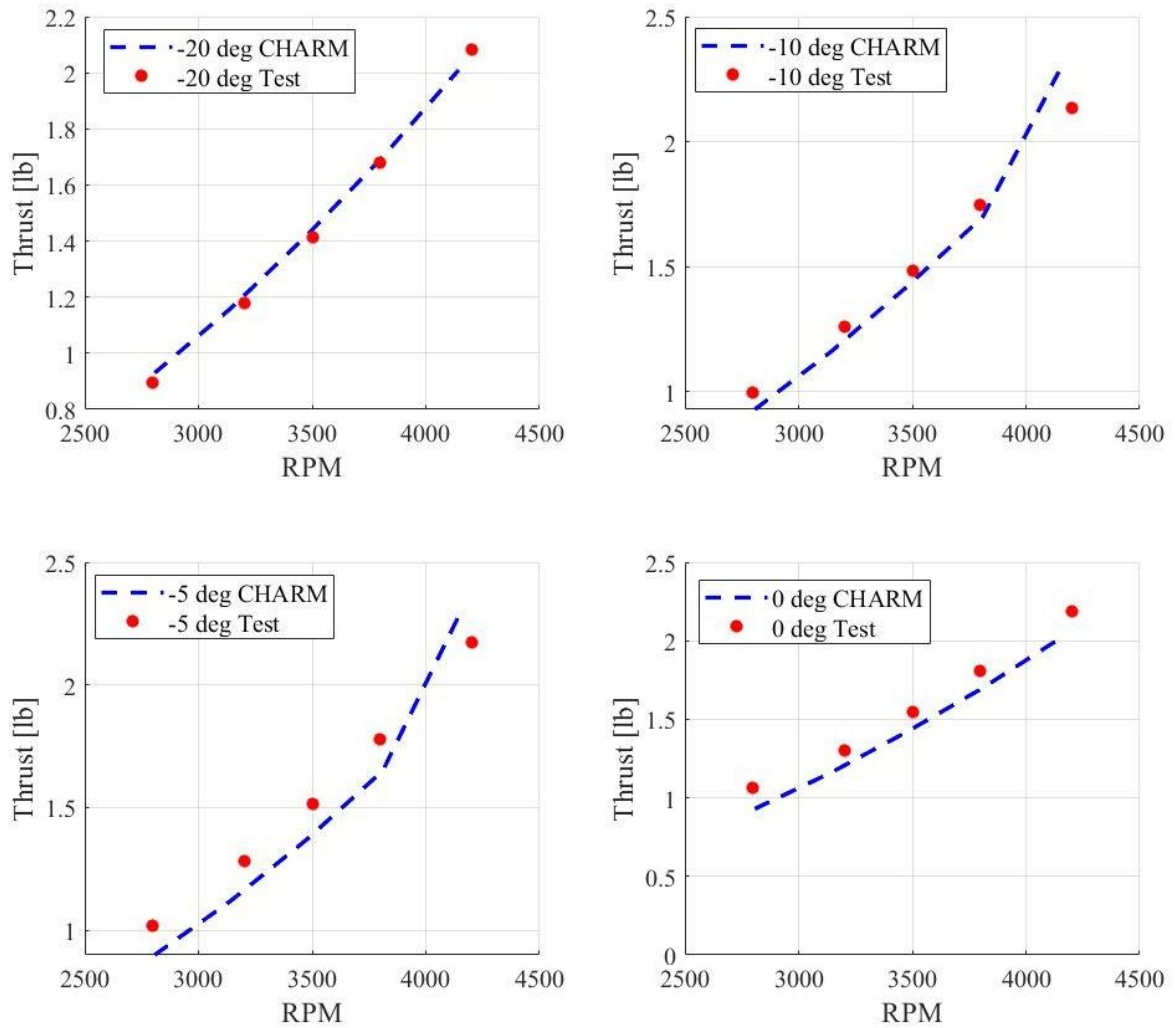
By inputting 20 airfoil locations and 19 segments into the *blade geometry* input files described in the last section, the SUI's airfoil shapes were defined throughout the entire span. Figure 3.10 shows the CHARM results in hover for the SUI rotor. The results show that the CHARM result has a discrepancy of 3.17% for thrust and 5.16% for power while the CAMRADII has a discrepancy of 6.97% for thrust and 7.59% for power in the hover case.



**Figure 3.10:** SUI hover case results using 20 airfoil sections to define the *Blade geometry* input file

The SUI rotor was simulated with a forward speed of 20 ft/sec in the wind tunnel. Due to the presence of the wall panels,  $NOISE = 1$  was used to consider the pressure distribution over flat plates [48]. Figure 3.11 shows the thrust values for forward flight at the rotor pitch angles of -20, -10, -5, and 0 degrees. The current CHARM settings produce a discrepancy of 3% to 10% for forward flight cases.

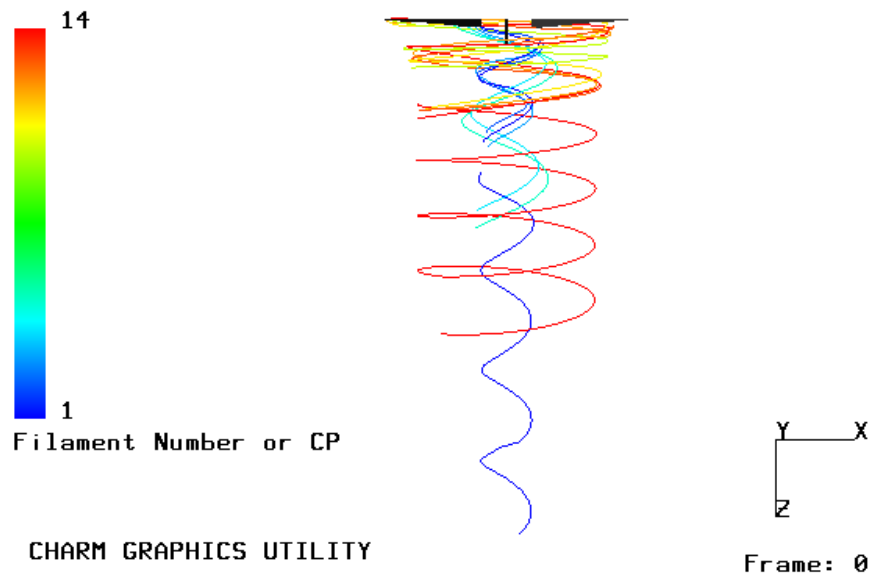
<sup>3</sup> Aero lab is located at Aeromechanics Branch at NASA Ames Research Center, Mountain View, CA



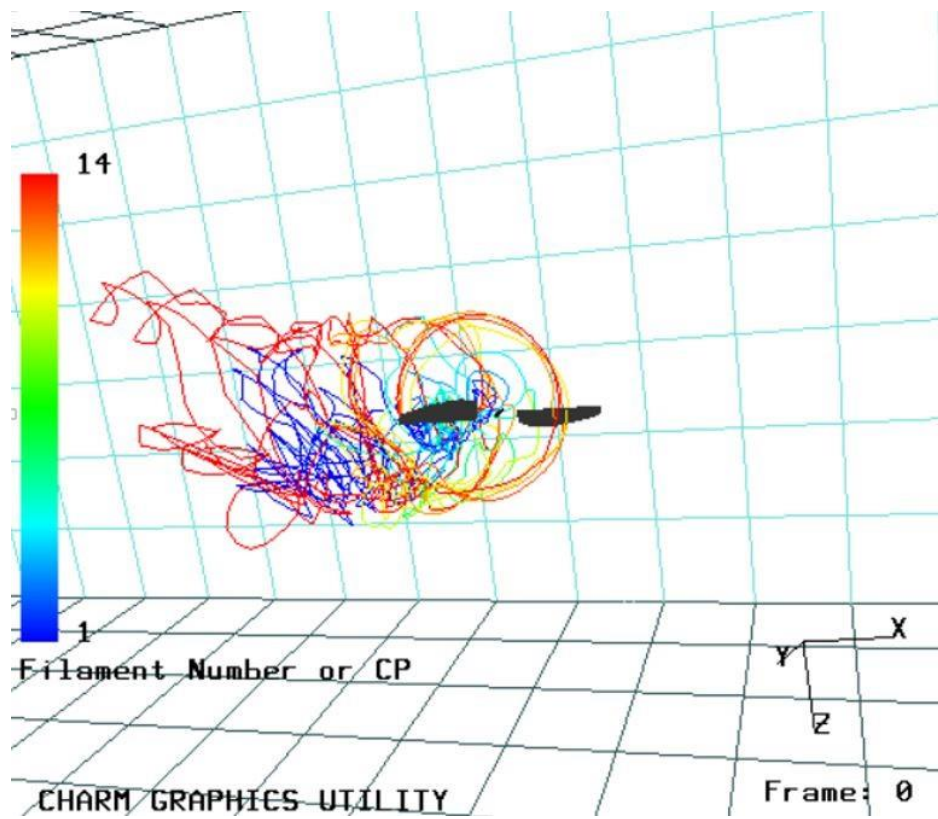
**Figure 3.11:** The thrust values for SUI rotor at forward flight at four different pitch angles

Figure 3.12 and Figure 3.13 demonstrate 3D visualizations, generated in Vortex-X, of the SUI rotor in hover and forward flight. At the forward flight, the rotor is thrusting out in the positive Y direction, and the wake is pushed in the negative Y direction and convected downstream to the negative X direction.





**Figure 3.12:** SUI rotor in hover



**Figure 3.13:** SUI rotor at forward flight



---

# CHAPTER 4

---

## Simulation Results of Multirotor Test Bed

As described earlier, CHARM uses Fast Vortex/Fast Panel methods to characterize the rotor aerodynamics behavior, including the rotor/wake interaction as well as wind tunnel wall effects [18, 49, 50], where the wind tunnel is modeled as inviscid incompressible flow. For the MTB simulations in CHARM, the wind tunnel test section was defined as a conventional closed tunnel with walls, floor, and ceiling. In this chapter, the CHARM simulation capabilities to predict the rotor behavior in a wind tunnel were tested by comparing the CHARM predictions to wind tunnel data [51]. At the time of this study, only preliminary wind tunnel data were available to use for the present work. The final version of the wind tunnel data will be developed by Carl Russell<sup>1</sup> and will be available at the beginning of 2021. In the first section, the isolated rotor simulation result was compared to the experimental data. Then, 24 wind tunnel cases were simulated and compared to preliminary data based on four types of variables: pitch angle, forward flight speed (wind tunnel speed), number of rotors, and rotor configuration (vertical distance). There are 3 pitch angles, 2 flight speeds, 4 rotor combinations, and 2 vertical rotor height configurations (tall and short). The study simulates starting from a smaller number of rotors as a simple case and increases the number of rotors up to the main focus of this work in the six rotor case. For the six rotor case the completed dataset was available to compare. For each simulation case, the air density was adjusted to the recorded value at the time of wind tunnel testing to provide a similar condition to the wind tunnel test. Then, the 24 cases were simulated at the same flight condition, Table 4.3, in free field and without the MTB structural test stand.

---

<sup>1</sup>Research Aerospace Engineer, Aeromechanics Office, NASA, ARC, Moffett Field

## 4.1. KDE Rotor in CHARM

The rotor selected for the MTB project was a two-bladed KDE-CF245-DP<sup>4</sup> made of carbon fiber, Table 4.1. The KDE rotor has a radius of 1.02 ft, which is in the smaller range of rotor size. The size of the KDE rotor was chosen small to minimize the wall effect on the experimental data. A KDE rotor was laser scanned, and the geometry of 25 airfoil sections was measured to define the blade dimensions, Figure 4.1. However, only 20 airfoil sections were used to create the *blade geometry* input file. Note that the KDE rotor's tip was so thin that no airfoil shape and geometry could be recorded.

**Table 4.1:** The KDE rotor parameters

Parameter	Value
Number of blades	2
Radius of blade	1.02 <i>ft</i>
Rotor disk area	3.27 <i>ft</i> <sup>2</sup>
Rotor speed	2000 <i>RPM</i>

These 20 airfoil sections create 19 segments,  $NSEG = 19$ . From the original 25 airfoil cross sections, four airfoil stations were selected to cover the driven region, driving region, and stall region to generate airfoil tables, with these three regions shown in Figure 4.2. Each rotor region has different characteristics, making it critical to select at least one or two airfoil stations from each region to generate airfoil tables according to the angle of attack and the Mach number of each airfoil station.

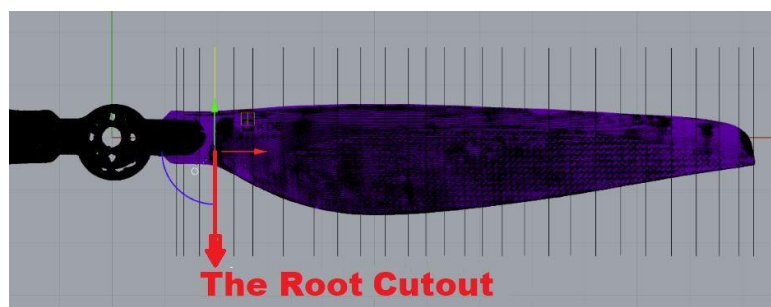


**Figure 4.1:** Axial view of KDE rotor and 28 cross sections- in *blade geometry* input file the geometry of 20 airfoil cross sections were used starting at the root cut (marked in red) [52]

<sup>4</sup> KDE Direct, [www.kdedirect.com/products/kde-cf245-dp](http://www.kdedirect.com/products/kde-cf245-dp)

The first airfoil station was selected at  $\frac{r}{R} = 0.1593$ , which is in the stall region. The stall region covers the inboard 25% of the blade radius nearest to the root of the blade and has the largest angle of the attack, causing drag and slowing down the rotor speed. The largest blade region is the driving region, also known as the autorotative region, which normally lies between about 25-70% of the blade radius. Therefore, two airfoil stations at  $\frac{r}{R} = 0.2662$  and  $\frac{r}{R} = 0.7515$  were selected to represent the behavior of the rotor in this region. The driving region makes up 45% of the blade radius, and most of the rotor lift is generated from this region. The fourth airfoil station, at  $\frac{r}{R} = 0.9432$ , belongs to the driven region, which makes up 30% of the blade radius nearest to the tip of the blade and generates drag, which slows down the rotation of the blade.

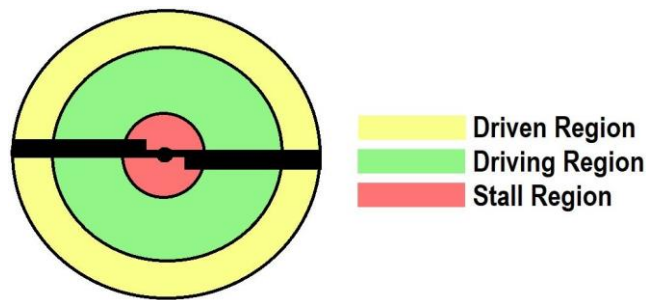


**Figure 4.2:** Blade regions in vertical descend

The airfoil tables for the four airfoil stations were generated using XFOIL [51]. These airfoil tables were generated by considering the environment and conditions such as wind tunnel speed, rotor speed, angle of attack, and Mach number that these four airfoil sections would experience. Since the local velocity is different in each airfoil station, the Reynolds number varies throughout the rotor span. Also, each airfoil station experiences a different Reynolds number depending on the azimuth angle of the blade in forward flight. An airfoil station experiences higher relative airflow at the advancing side of the rotor compared to the retreating side, Figure 4.3. The relative airflow at the advancing side is in the same direction as the forward speed; therefore, the relative airflow is equal to the forward speed and the rotor's speed [53]. At the retreating side, the relative airflow is the speed of forward flight subtracted from the rotor speed. (Note this is correct at the 90 and 270 degrees azimuth angle.

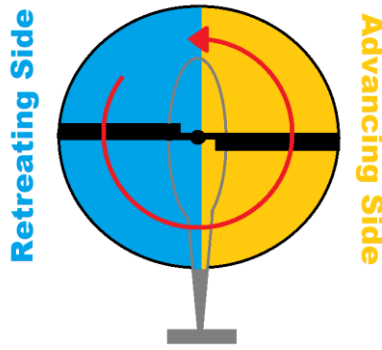


**Figure 4.3:** Graphical representation of advancing and retreating sides of a rotor

Table 4.2 shows airfoil stations, Reynolds numbers, and Mach numbers used in XFOIL to create the airfoil tables for the KDE rotor [11] [51]. These airfoil tables were used to generate the *2D airfoil section data* input file for CHARM simulations. In the *2D airfoil section data* input file, the last airfoil station must be  $\frac{r}{R} = 1.0$ , therefore the  $\frac{r}{R} = 0.9432$  was placed at the tip and was reported as  $\frac{r}{R} = 1.0$  in this input file. Also, CHARM requires the first airfoil section to be at the root of the blade and is recorded as  $\frac{r}{R} = 0$ . The airfoil tables in the look-up tables need to cover all the Mach numbers of any blade section that might occur during the CHARM calculation. The Mach numbers in CHARM should run from 0 to 1 to cover every possible flight condition. There was no airfoil table available for the KDE rotor at Mach number 1. Therefore, the highest Mach number was repeated to present the look-up table for the sonic Mach.

**Table 4.2:** Reynolds number of four main airfoil stations used to generate the airfoil tables in XFOIL

r/R	Local Mach#	Local Re#
0.1891	0.03	18,543
0.2662	0.05	55,807
0.7515	0.14	127,780
0.9432	0.18	98,346

In the *blade dynamics* input file, the following parameters must be set to define the KDE rotor as a rigid hingeless rotor (similar to the SUI rotor),  $IART = 0$ ,  $HINGE = 0$ , and  $IRIGID=1$ . Due to the lack of information about the KDE rotor frequency modes, the rest of the settings on the *blade dynamics* input file's parameters are unchanged from the SUI rotor.

#### 4.1.1. Rotor Positions in CHARM

Rotor locations were defined in three-dimensional space in the rotor/wake input file. In CHARM, the wind tunnel center is the origin of coordinate system by default. In this study, the X-axis is positive in the opposite direction of airflow, the Y-axis is positive for rotors number 1, 3, and 5, and the Z-axis is positive downward. Note that the MTB test stand was not included in CHARM simulations, but in Figure 4.4 the structural test stand was shown to make the visualization of the CHARM coordinates effortless.

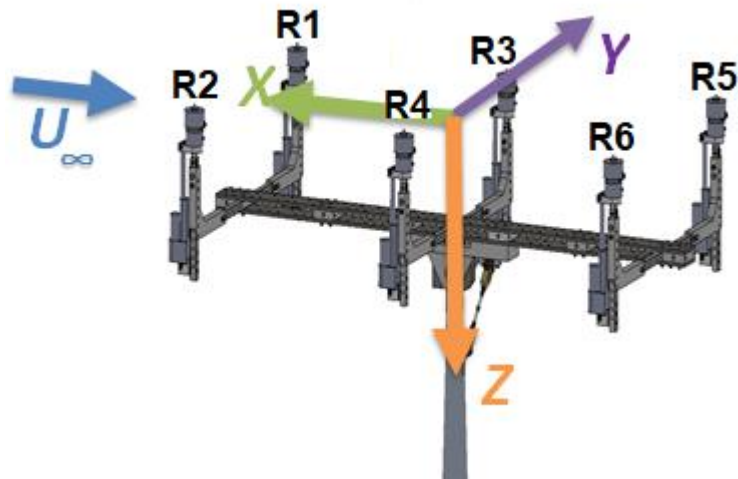


**Figure 4.4:** The coordinate defined by CHARM for MTB structure test stand in free stream. Notice that this MTB system is a side view with the free stream coming from the left (while Figure 1.5 is a top view with the free stream coming from the right).

As mentioned in Chapter 1, the lateral and longitudinal distances between rotors are fixed at 38.7 and 36.0 inches. Rotor vertical distances change with respect to the center point of the wind tunnel from -22.0 to -15.0 inches, respectively, for the tall and short configuration. Also, changing the shaft angle from 0 degrees to -5 and -10 degrees varies the rotor's locations in the X-Z plane. Figure 4.5 shows the location of rotors number two and six before rotation at a 0 degrees shaft angle and after

rotation in negative shaft angle. Since the rotors are not connected, due to the absence of the structural test stand, the rotor location was recalculated with respect to origin using the rotation matrix, Equation 4.1.

$$\begin{bmatrix} x' \\ z' \end{bmatrix} = \begin{bmatrix} \cos \theta & -\sin \theta \\ \sin \theta & \cos \theta \end{bmatrix} \begin{bmatrix} x \\ z \end{bmatrix}$$

$$x' = x \cos \theta - z \sin \theta \quad z' = x \sin \theta + z \cos \theta \quad (4.1)$$

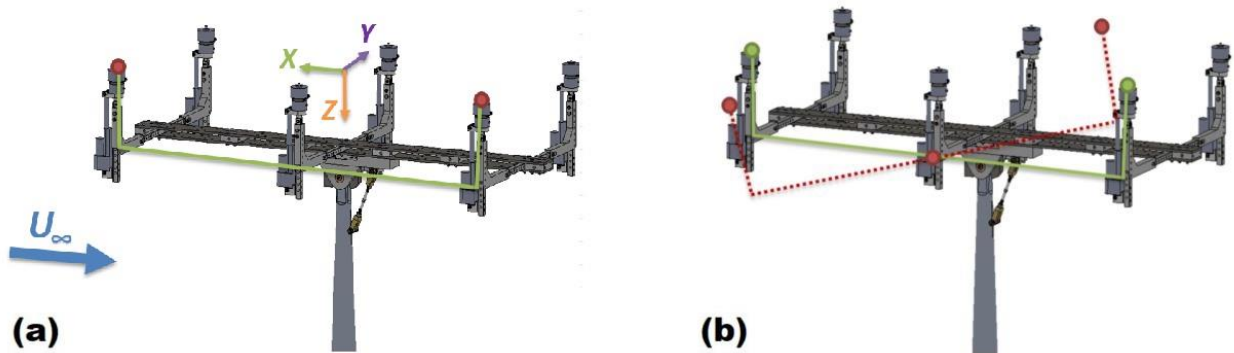


**Figure 4.5:** The MTB structure and location of the rotors at (a) 0 shaft angle and (b) negative shaft angle

Figure 4.6 is the visualization of the location for six rotor cases in the short configuration at 0, -5, and -10 degrees shaft angles in the wind tunnel boundary in Vortex-X. In addition, the MTB rotor system does not have a hinge; therefore, the collective angle is fixed, and the *ICOLL* parameter must be set to 0 in the *rotor/wake* input file.

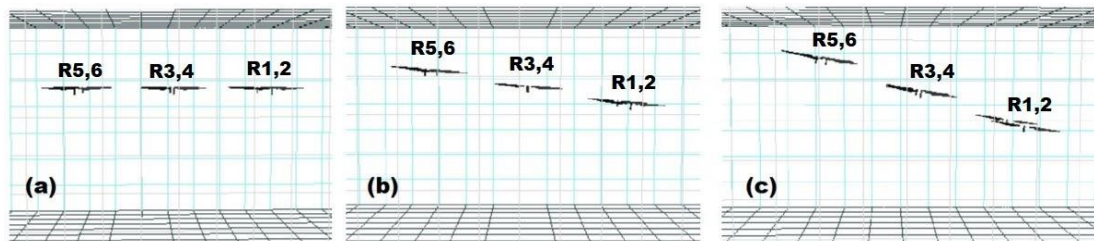


**Figure 4.6:** Side view of the MTB at shaft angles of (a) 0 degrees, (b) -5 degrees, and (c) -10 degrees

## 4.2. Isolated Rotor in Hover

The isolated rotor was tested in the Aero Lab for the free field in hover case. Even though the hover test was done at various speeds, the only experimental data available for comparison was *Run 121, Point 5*, with a 0 degree pitch angle at 2000

RPM. The experimental thrust and power values were calculated using the recorded forces from the six axes load cells. Each rotor's thrust was determined using Equation 4.2, where  $\alpha$  is the angle between the free stream and the rotor disk,  $F_x$  is aft, and  $F_z$  is thrust, with the aerodynamics forces shown in Figure 4.7. Note that for the hover case  $\alpha = 0$ . The torque value can be calculated using Equation 4.3, where  $M_x$  is the roll moment and  $M_z$  is the yaw moment. The moment on the y-axis is known as the pitch moment,  $M_y$ , and the force on the y-axis,  $F_y$ , is the side force. The  $F_y$  force is positive in the direction out of the page, using the right-hand rule. Note that the CHARM coordinates are not the same as the load cell coordinates.

$$Thrust = \sin\alpha F_x + \cos\alpha F_z \quad (4.2)$$

$$Torque = \sin\alpha M_x + \cos\alpha M_z \quad (4.3)$$

Experimental power values were calculated using  $P_{exp} = T \times V_\zeta$  equation, discussed in Chapter 3. The KDE isolated rotor was simulated at an RPM sweep from 500 to 6000. To illustrate the hover flight condition, the *IGPR* parameter is set to one, and the free stream speed at the  $-X$  direction set to zero,  $U = 0$ , in the *run characteristics* input file while sweeping the RPM, and *OMEGA* in the rotor/wake input files. Respectively the thrust and power results from the simulation were plotted versus  $RPM^2$  and  $RPM^3$  in Figures 4.8 and 4.9. It is worth noting that merely one hover experimental data point cannot represent the actual overall performance, particularly the complexity of the unstable wakes generated during hover. Due to the limited access of wind tunnel data, this research continues with complete simulation results ready for the future wind tunnel data. According to this available experimental data set, the CHARM simulation slightly over predicted the thrust and power results at hover.

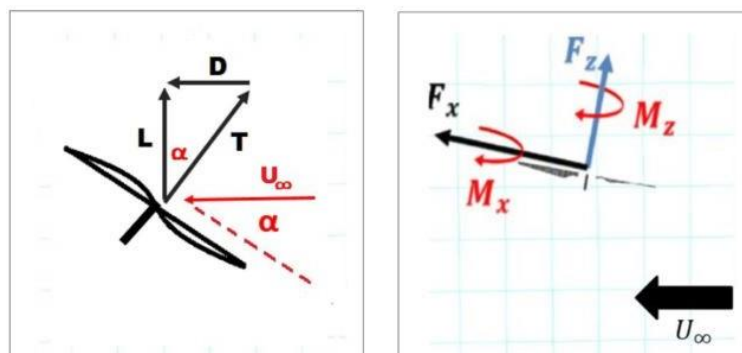


**Figure 4.7:** Aerodynamic forces on a rotor disk (right) - forces and moments on

the load cell (left)

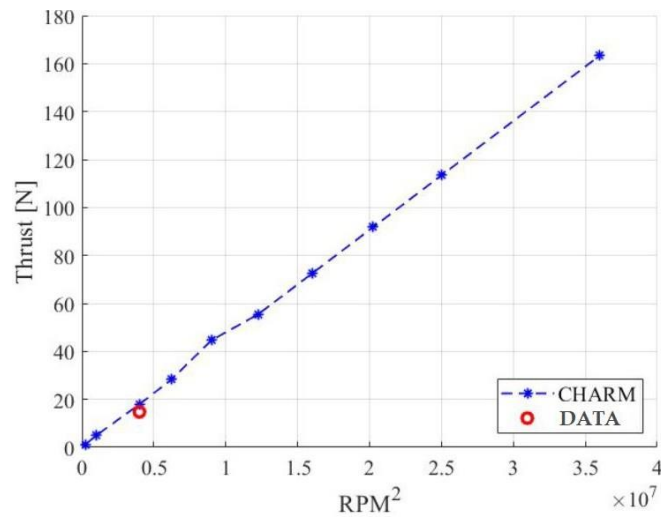


**Figure 4.8:** Isolated rotor in hover – RPM<sup>2</sup> vs thrust

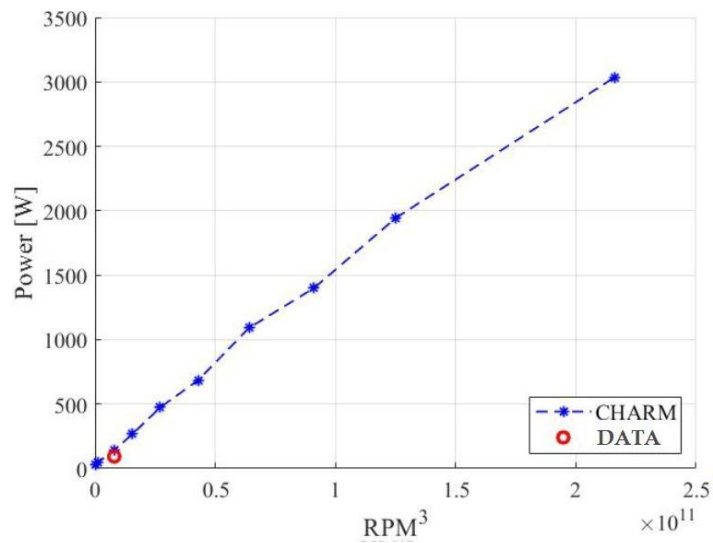


**Figure 4.9:** Isolated rotor in hover – RPM<sup>3</sup> vs power

Figure 4.10 demonstrates the figure of merit versus RPM sweep for simulation and experimental data. The predicted figure of merit values were mostly in the expected range of 0.6 – 0.7 for the KDE rotor. The difference between the predicted results with the single experimental data point indicates CHARM under calculated the FM at 2000 RPM with a discrepancy around 13%. Note that the experimental data is a preliminary result, and these values could be different for the final data.



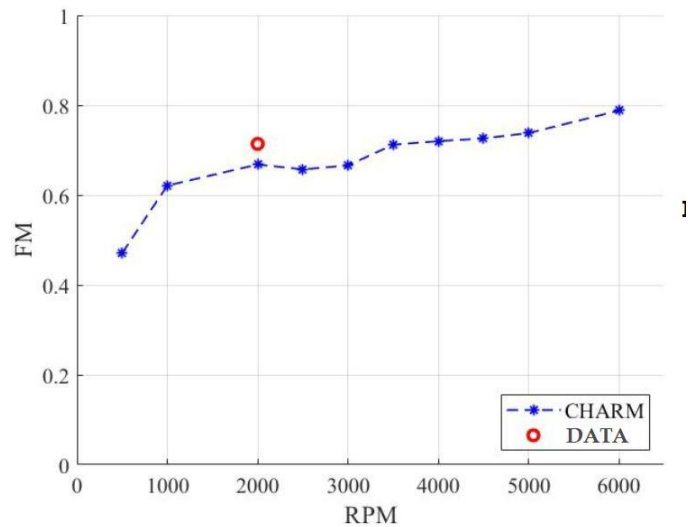


**Figure 4.10:** Isolated rotor in hover – RPM vs figure of merit

### 4.3. Simulation of Multirotor Test Bed in Forward Flight in the Wind Tunnel

This section introduces the forward flight wind tunnel conditions selected to simulate for this research. The shaft angles were set to 0, -5, and -10 degrees; forward flight speeds at 20 and 40 ft/s; one, two, four, and six rotors cases; and short and tall configurations with a 7 inches difference. Table 4.4 shows 24 cases selected for CHARM simulations in the wind tunnel and without the MTB test stand structure. The first three columns indicate the run number, case number, and data point selected from the preliminary datasheet. The pitch angle, *Pitch*, was adjusted by changing the shaft angle, and forward flight speed, *V*, was varied by adjusting the wind tunnel speed. All 24 cases were run at 2000 RPM,  $\Omega = 209$ , at forward flight,  $IGPR = 0$ . The wind tunnel was defined the same as in the *run characteristics* input file for the SUI rotor case.

**Table 4.3:** MTB test matrix

Run	Case	Point	Pitch [Deg]	V [ft/s]	# of Rotors	Configuration
121	1	8	-10	20	1	Short
121	2	13	-5	20	1	Short
121	3	24	0	20	1	Short
122	4	8	-10	40	1	Short
122	5	10	-5	40	1	Short
122	6	14	0	40	1	Short
112	7	8	-10	20	6	Short
112	8	13	-5	20	6	Short
112	9	22	0	20	6	Short
113	10	8	-10	40	6	Short
113	11	10	-5	40	6	Short
113	12	14	0	40	6	Short
102	13	8	-10	20	6	Tall
103	14	8	-5	20	6	Tall
103	15	16	0	20	6	Tall
104	16	10	-10	40	6	Tall
104	17	13	-5	40	6	Tall
104	18	19	0	40	6	Tall
114	19	8	-10	20	4	Short
114	20	14	-5	20	4	Short
114	21	24	0	20	4	Short
116	22	8	-10	20	2	Short
116	23	13	-5	20	2	Short
116	24	23	0	20	2	Short

### 4.3.1. One Rotor in the Wind Tunnel

The single KDE rotor was simulated at 20 ft/s and 40 ft/s for forward flight. Rotor number two, Figure 1.5, was the only rotor installed on the MTB structure during the single rotor test. Figure 4.11 shows the location from a top view of rotor number two in the wind tunnel. The test section length of the 7-

by 10-Foot Wind Tunnel is 15 ft, but in CHARM, the test section length was set to 50 ft to give the simulation enough time to fully develop the flow. Since all single rotor runs were tested in the short configuration, the rotor is placed at 4.75 ft from the wind tunnel floor and 2.25 ft from the ceiling boundary, shown in Figure 4.12.

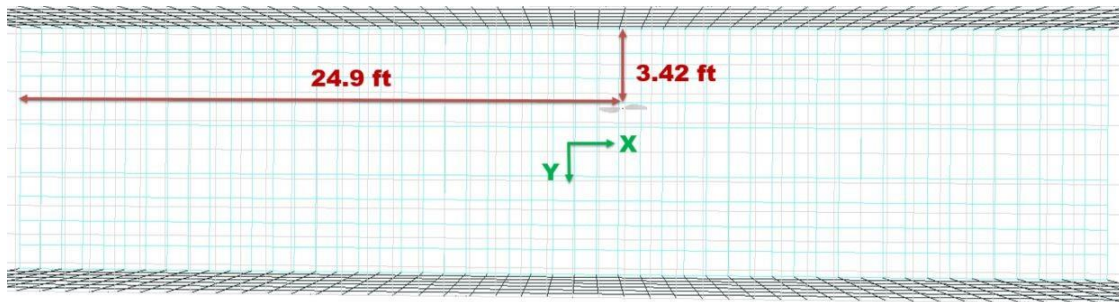


**Figure 4.11:** The top view of location of the rotor number two inside the wind tunnel boundary defined by CHARM

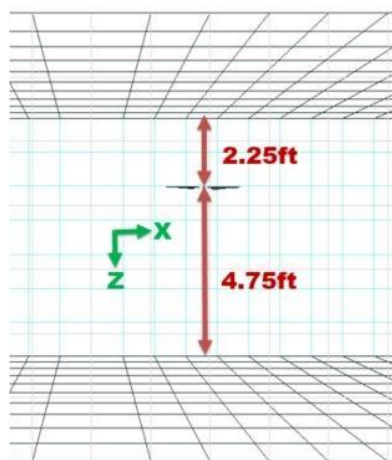


**Figure 4.12:** The side view of location of the rotor number two inside the wind tunnel boundary defined by CHARM

Figure 4.13 shows the experimental and predicted values for thrust and power at pitch angles of 0, -5, and -10 degrees. It was observed that by decreasing the pitch angle, the thrust value increased for CHARM predictions and wind tunnel data. Also, CHARM predictions for thrust and power are much closer to the experimental data at the lower forward flight speed of 20 ft/s. Table 4.4 presents the power and thrust discrepancy between the experimental data and CHARM predictions at different shaft angles and wind tunnel speeds. These results indicate the error for thrust and power was roughly of similar magnitude for single rotor cases. Also, thrust discrepancy and power discrepancy were at their minimum when the pitch angle is -10 degrees at forward flight speeds of 20 and 40 ft/s.

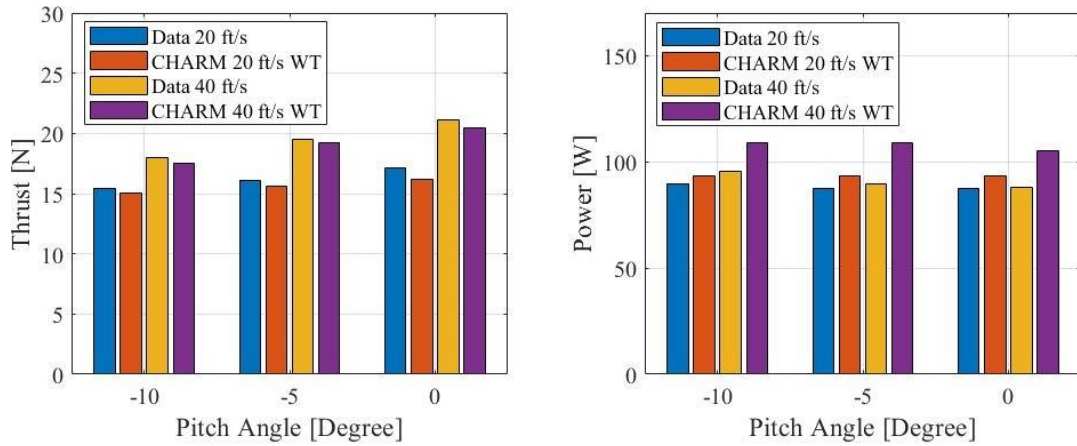


**Figure 4.13:** The rotor thrust and power values for single rotor cases in the short configuration at wind tunnel in forward flight at 20 and 40 ft/s

**Table 4.4:** Discrepancy between the CHARM prediction and experimental data for single rotor at the wind tunnel in forward flight testing

Discrepancy of Thrust	Discrepancy of Power	Pitch [Deg]	V [ft/s]
-1.79%	+4.31%	-10	20
-2.11%	+6.88%	-5	20
-4.25%	+6.78%	0	20
-1.37%	+14.13%	-10	40
-0.18%	+21.50%	-5	40
-2.06%	+ 19.19%	0	40

Figure 4.14 shows flow visualization of the single rotor in the short rotor configuration in Vortex-X, where the pitch angle is 10 degrees, and the wind tunnel speed is 20 ft/s.

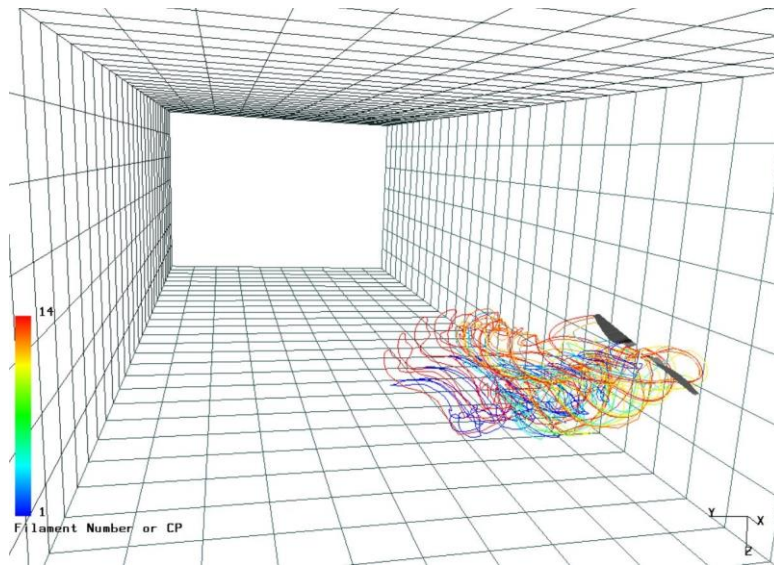


**Figure 4.14:** Flow visualization of single KDE rotor in the short rotor configuration, a -10 degrees pitch angle, and a forward flight speed of 20 ft/s in the wind tunnel

### 4.3.2. Two Rotors in the Wind Tunnel

Two rotors were simulated in the wind tunnel at forward flight mode with a wind tunnel speed of 20 ft/s at pitch angles of 0, -5, and -10 degrees. The two rotors selected for these runs were rotors number three and four, located at the middle of the MTB structure test stand. Figure 4.15 shows the location of rotors with respect to the wind tunnel walls. The simulation results for average power and average thrust are compared to the wind tunnel experimental data in Figure 4.16.

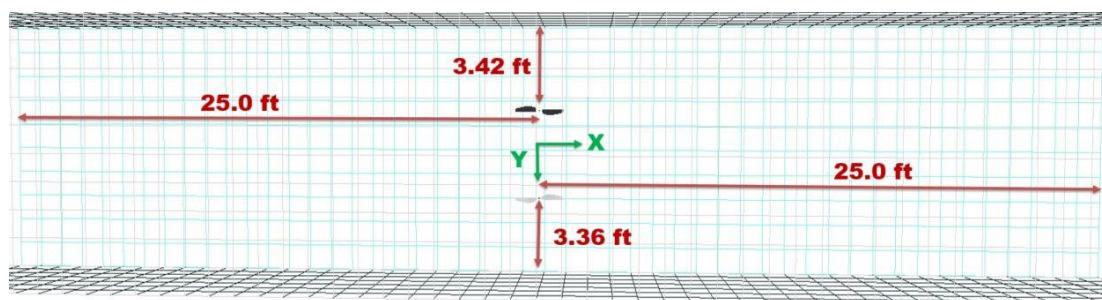


**Figure 4.15:** The top view of location of rotors number three and four inside the wind tunnel boundary defined by CHARM

These results indicate that the thrust value increases with a decrease in pitch angle for CHARM results and experimental data; however, the power value decreased by decreasing the pitch angle. Also, thrust predictions were on average, 9.43% closer to the experimental data compared to the power prediction.

Table 4.5 shows the discrepancy between the average thrust and power predictions and experimental data. These results show that the average thrust discrepancy, 0.6%, and the average power discrepancy, 7.77%, are at their minimum at the pitch angle of -10 degrees.

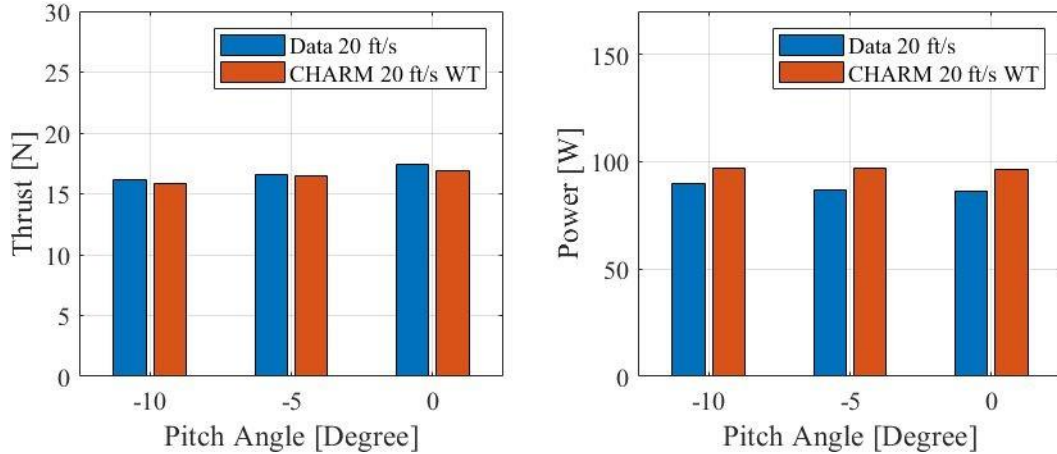


**Figure 4.16:** Averaged thrust and average power values for two rotor cases in the short configuration at wind tunnel in forward flight testing

**Table 4.5:** Discrepancy between the CHARM predictions and experimental data for two MTB rotors at the wind tunnel in forward flight testing speed of 20 ft/s

Discrepancy of Ave. Thrust	Discrepancy of Ave. Power	Pitch [Deg]	V [ft/s]
-0.59%	+7.77%	-10	20
-0.60%	+11.83%	-5	20
-1.54%	+11.43%	0	20

Figure 4.17 is a flow visualization of two MTB rotors from a top view in Vortex-X in the short rotor configuration with pitch angle of -10 degrees. Additional Vortex-X flow visualizations can be found in Appendix B.



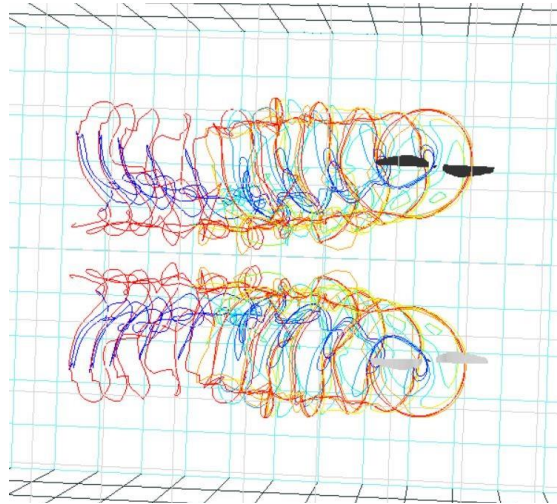


**Figure 4.17:** Flow visualization of rotors number three and four at the short rotor configuration, -10 degrees pitch angle, and speed of 20 ft/s in the wind tunnel

### 4.3.3. Four Rotors in the Wind Tunnel

Four rotor cases were tested at a 20 ft/s forward speed in the wind tunnel where the rotors number one, two, three, and four were installed on the MTB structure test stand, and data was collected at pitch angles of 0, -5, and -10 degrees. Figure 4.18 shows the location of the four rotors inside the wind tunnel simulation boundary.

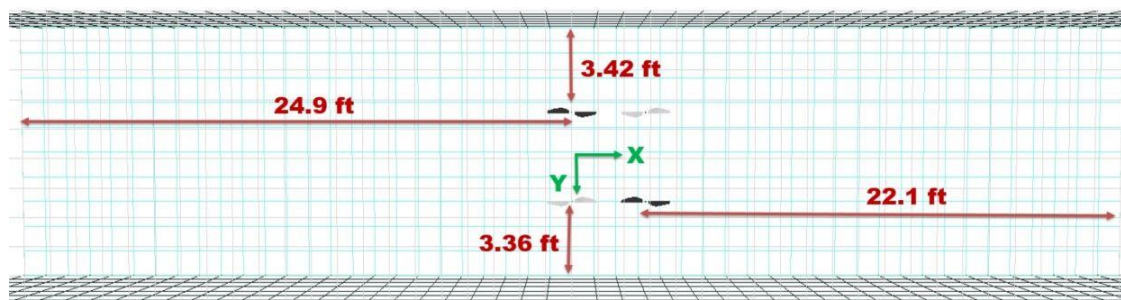


**Figure 4.18:** The top view of location of rotors number 1-4 inside the wind tunnel boundary defined in CHARM

Simulation results for average power and average thrust are compared with experimental data in Figure 4.19. These results also indicate the over prediction of power by CHARM and slightly under predicted thrust value for four rotor configurations at the 20 ft/s forward speed. As seen in the two rotor case, the thrust prediction has the smallest discrepancy value, 0.15%, at a pitch angle of -10 degrees. Also, the power simulation results have the smallest discrepancy, 5.61%, at a -10 degrees pitch angle. Table 4.6 presents a discrepancy between

the CHARM predictions and experimental data for average power and average thrust of four rotors in the short configuration for rotors 1-4.

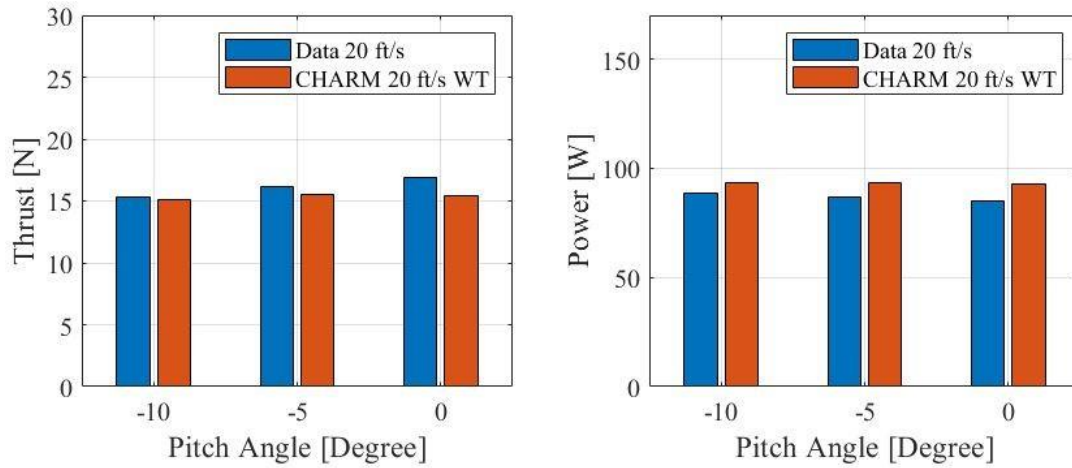


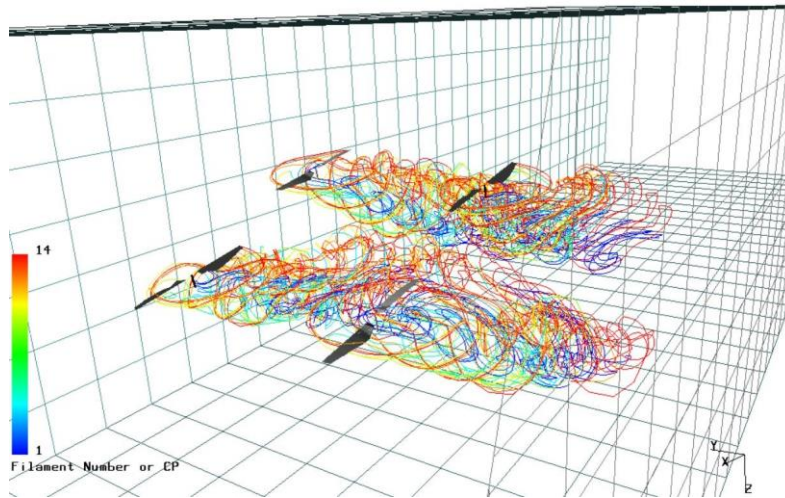
**Figure 4.19:** Averaged thrust and power values for four rotor cases in the short configuration at wind tunnel in forward flight testing

**Table 4.6:** Discrepancy between the CHARM prediction and experimental data for four MTB rotors at the wind tunnel in forward flight testing at speed of 20 ft/s

Discrepancy of Ave. Thrust	Discrepancy of Ave. Power	Pitch [Deg]	V [ft/s]
-0.15%	+5.61%	-10	20
-2.85%	+7.47%	-5	20
-7.78%	+8.89%	0	20

Figure 4.20 shows four KDE rotors at a pitch angle of -10 degrees in the short configuration in the test section using Vortex-X. In the four rotor test, a wake interaction of front rotors with the back rotors appeared, which is discussed in the next chapter. Additional figures for four rotor cases at different pitch angles can be found in Appendix B.

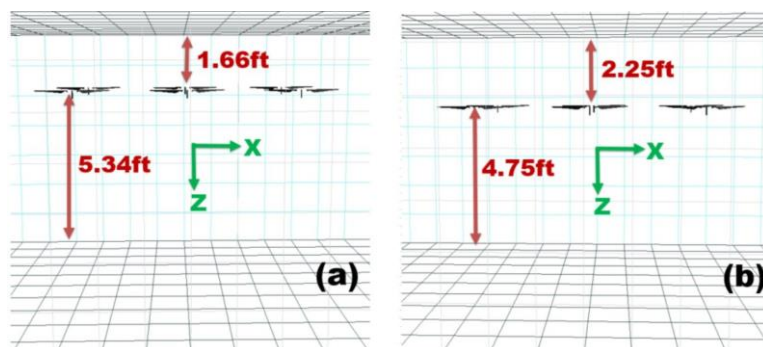




**Figure 4.20:** Flow visualization of rotors numbers 1-4 in the short rotor configuration, at the -10 degrees pitch angle, and with a wind tunnel speed of 20 ft/s

#### 4.3.4. Six Rotors in the Wind Tunnel

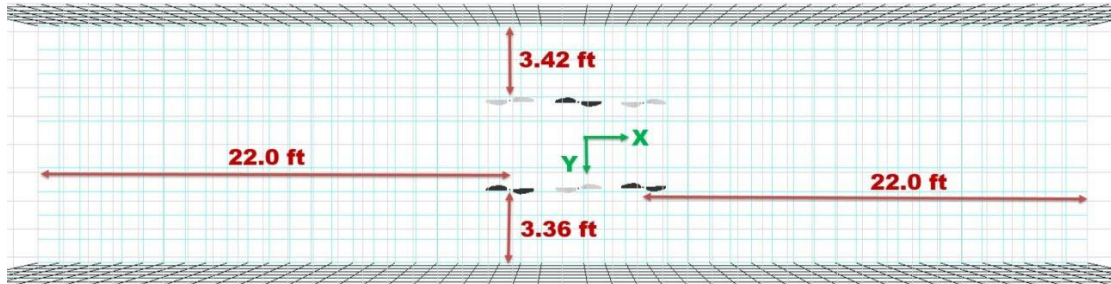
Six rotor simulations completed in short and tall configurations, where the rotors were located 7 inches higher for the tall configuration. The rotor distance from the ceiling at the tall and short configuration were 1.66 ft and 2.45 ft, respectively, at a 0 degrees shaft angle. Changing the shaft angle brings rotors number five and six closer to the ceiling, while rotors number one and two get further from the ceiling. Figure 4.21 shows the location of the six rotor cases in the wind tunnel in the X-Z plane; therefore, only three rotors are visible in this view.



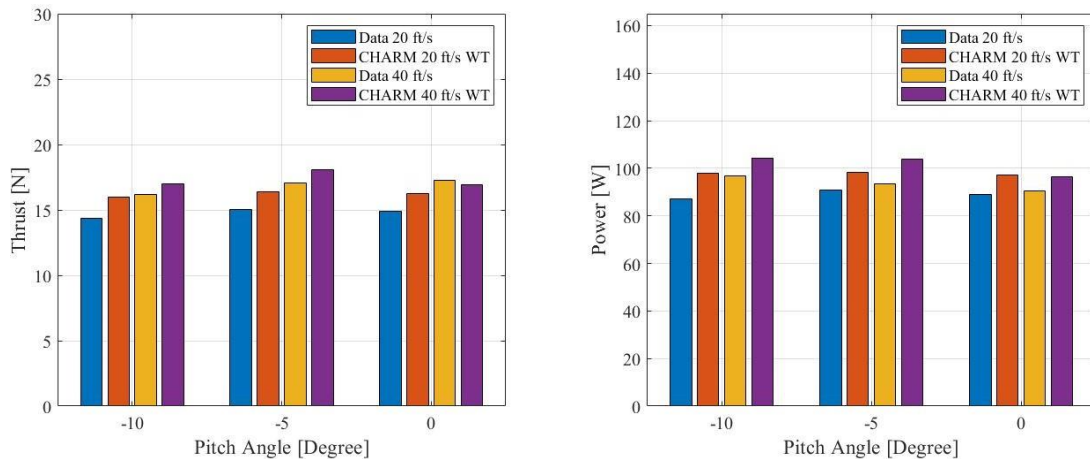
**Figure 4.21:** Rotors height in the wind tunnel at 0 degrees pitch angle at (a) tall and (b) short configuration for six rotor cases

Figure 4.22 shows the distance of the six rotors from the sidewalls for the short and tall configuration in the wind tunnel boundary in CHARM. Figure 4.23 shows the average thrust and average power values for six rotors in the short configuration at the pitch angles of 0, -5, -10 degrees at 20 and 40 ft/s forward

flight. As was expected, the power and thrust value predictions are higher at 40 ft/s in comparison to 20 ft/s cases. It was also observed that at 40 ft/s, the thrust simulation results were over predicted at -10 and -5 degrees and under predicted for 0 degrees pitch angles.



**Figure 4.22:** The top view of location of rotors number 1-6 inside the wind tunnel boundary defined in CHARM



**Figure 4.23:** Data and CHARM results for six rotors at short configuration in the wind tunnel - thrust and power vs. pitch angle

The average thrust and power predicted for the tall configuration for six rotors are shown in Figure 4.24. Similar to the short configuration, the power and thrust were over predicted except for the thrust at the 0 degrees pitch angle. Average thrust values at of forward flight speeds 20 and 40 ft/s were similar for the tall configuration, suggesting that in the future, looking at individual rotor thrust and power could provide a better understanding of the wake interaction. Tables 4.8, and 4.9 provide closer comparison of the predicted results for average thrust and average power with the experimental data for both short and tall configurations at forward flight speeds of 20 and 40 ft/s.

**Table 4.7:** Discrepancy between the CHARM prediction and experimental data for six rotors case at short configuration at the wind tunnel in forward flight speed of 20 and 40 ft/s

Discrepancy of Ave. Thrust	Discrepancy of Ave. Power	Pitch [Deg]	V [ft/s]
+11.5%	+12.4%	-10	20
+9.00%	+8.18%	-5	20
+9.39%	+8.94%	0	20
+5.01%	+8.00%	-10	40
+5.88%	+11.2%	-5	40
-2.13%	+6.56%	0	40

**Table 4.8:** Discrepancy between the CHARM prediction and experimental data for six rotors case at tall configuration at the wind tunnel in forward flight speed of 20 and 40 ft/s

Discrepancy of Ave. Thrust	Discrepancy of Ave. Power	Pitch [Deg]	V [ft/s]
-2.10%	-3.63%	-10	20
+7.12%	+4.07%	-5	20
+5.86%	+4.11%	0	20
+2.31%	+7.53%	-10	40
+3.93%	+10.4%	-5	40
-5.62%	+5.82%	0	40

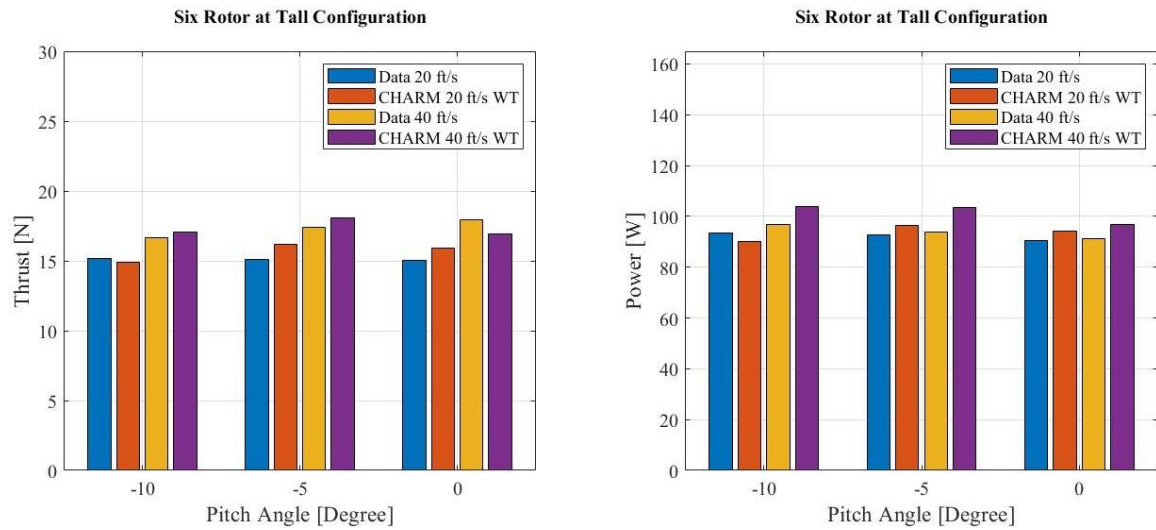


**Figure 4.24:** Experimental data and CHARM results for six rotors at tall configuration in the wind tunnel - thrust and power vs. pitch angle

#### 4.4. Agreement with Experiments

Predicted thrust values of the wind tunnel experiment demonstrate an average discrepancy less than 10% for all cases. The average discrepancy of one rotor, two rotors, and four rotor cases for average thrust, were 1.96%, 1.37%, and 2.69%, respectively. The average thrust discrepancy for the six rotor case in the short and tall configurations were 7.15% and 4.49%; however, simulation power results demonstrate more variability in each case. The average discrepancy of the one rotor, two rotor, and four rotor cases, for average power, accordingly, were 12.13%, 15.51%, and 5.49%. A higher discrepancy percentage for four rotors and six rotor cases was expected due to the generated wake from each blade interacting with each other. However, the average power value predicted by CHARM had an average discrepancy of 9.21% and 5.92% for the six rotor cases in the short and tall configurations. It was also observed that the average thrust and average power in the short configuration had a 1%-3% higher discrepancy when compared with tall configurations. These results indicate that CHARM predicts better overall results for the lower forward flight speed 20 ft/s, and the taller vertical configuration. The pitch angle influence remains uncertain due to the wake interaction. Further study is needed on the wall effects and rotor wake interactions.

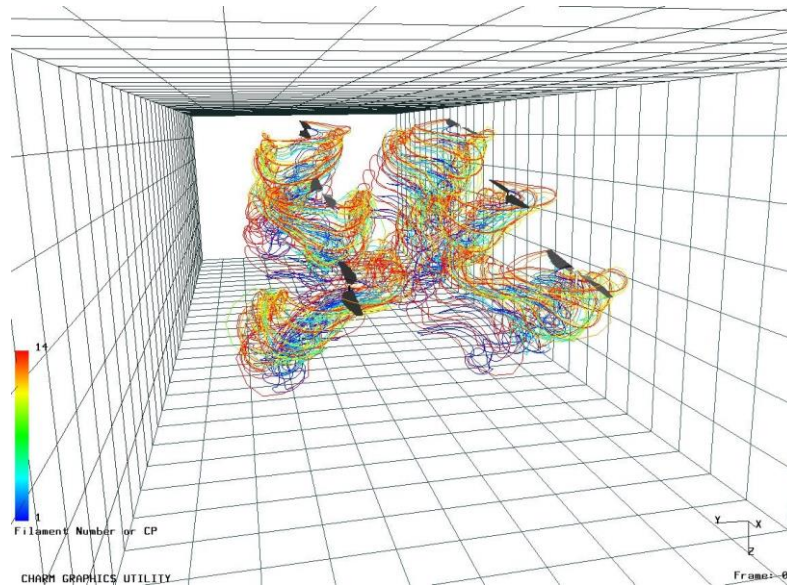


**Figure 4.25:** Six rotors at tall configuration in the wind tunnel, with a -10 degrees pitch angle and forward flight speed of 20 ft/s

#### 4.5. Simulation of Multirotor Test Bed without Wind Tunnel

A single rotor was simulated in a free field at forward flight speeds of 20 and 40 ft/s. Figure 4.26 shows thrust and power predicted in the free field and the wind tunnel data for forward flight. Similar to the predicted wind tunnel results for one rotor, CHARM slightly under predicted the thrust values and over predicted the power. Table 4.10 presents the discrepancy between the predicted free field results and wind tunnel testing. The thrust and power values were similar to the predicted wind tunnel results, as shown in Table 4.4. Correspondingly, simulation in the free field was plotted for two rotors and four rotor cases with the forward flight speed of 20 ft/s. Figure 4.27 shows the average power and average thrust predicted versus the wind tunnel test data. Table 4.9 shows the discrepancy between the experimental data and the free field prediction of the two and four rotor cases. These results equivalently show over prediction of power and under prediction of thrust compared with experimental data. The average thrust discrepancy for four rotor cases shows an increase of 1% to 2% compared to the discrepancy result of predicted thrust values in the wind tunnel.

**Table 4.9:** Discrepancy between the CHARM prediction and experimental data for the single rotor case in free field forward flight

Discrepancy of Thrust	Discrepancy of Ave. Power	Pitch [Deg]	V [ft/s]
-1.79%	+4.31%	-10	20
-2.94%	+6.88%	-5	20
-5.03%	+ 6.78%	0	20
-2.11%	+ 14.13%	-10	40
-0.87%	+ 21.50%	-5	40
-2.48%	+ 20.03%	0	40

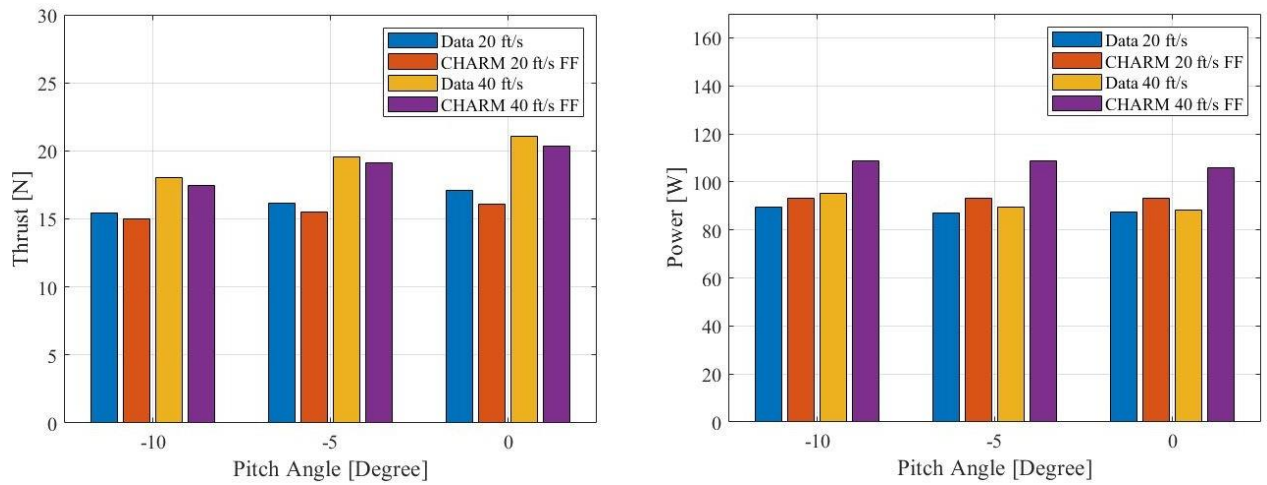


**Figure 4.26:** Single rotor in free field - thrust and power vs. pitch angle

**Table 4.10:** Discrepancy between the CHARM predictions and experimental data for two and four rotors at forward flight in free field

Discrepancy of Ave. Thrust	Discrepancy of Ave. Power	Pitch [Deg]	V [ft/s]	# of Rotors
+2.12%	+5.18%	-10	20	4
-3.88%	+7.26%	-5	20	4
-10.60%	+10.21%	0	20	4
-1.70%	+7.77%	-10	20	2
-0.34%	+ 11.83%	-5	20	2
-1.29%	+ 12.29%	0	20	2

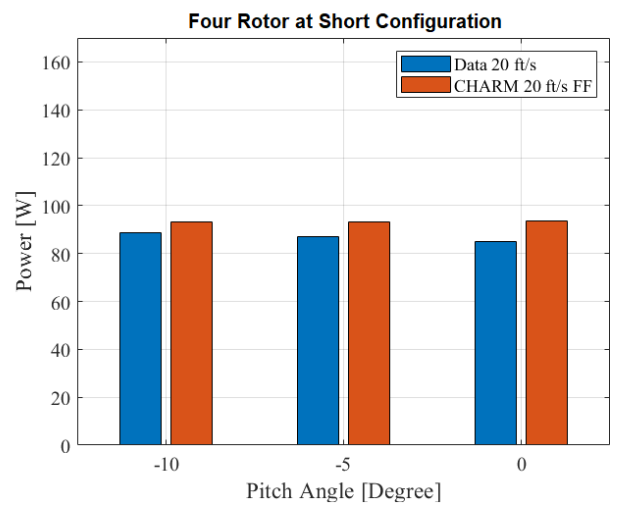
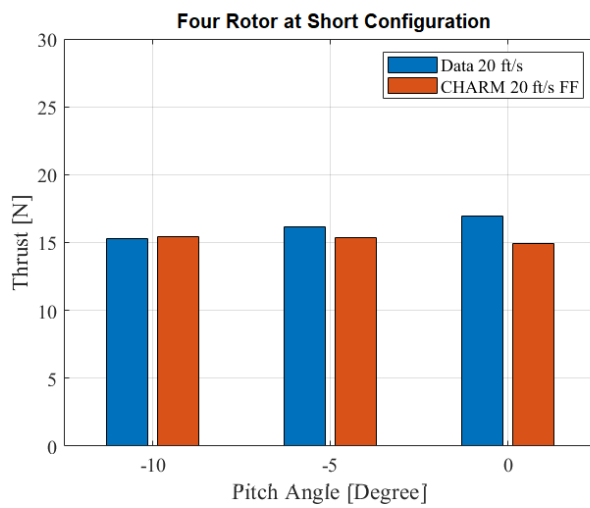
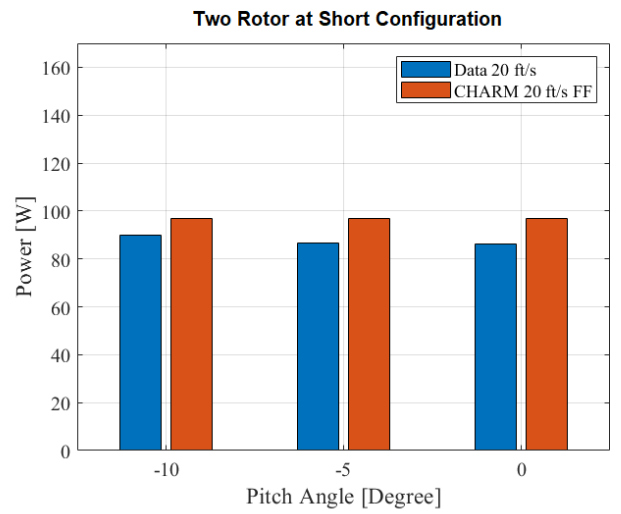
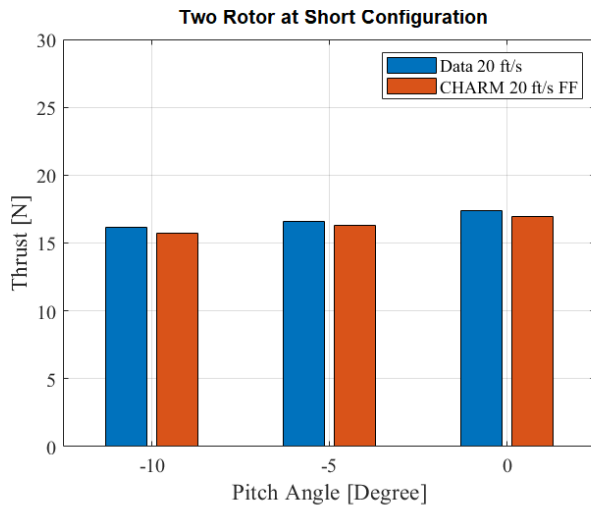


**Figure 4.27:** Two rotor and four rotor free field cases - average thrust and average power vs. pitch angle



Lastly, the six rotor free field cases were simulated in the short and tall configurations at forward flight speeds of 20 ft/s and 40 ft/s. The average power and average thrust of these 12 cases are shown in Figure 4.28. The discrepancy between the experimental wind tunnel data and the free field simulations is shown in Table 4.11. The results for the short configuration have a discrepancy less than 7%. These results indicate that the current CHARM settings allow for better prediction of thrust than power in free field simulations. A lower discrepancy between the one rotor case versus the six rotor cases was expected for short configurations. However, the average power discrepancy of the one rotor case was 12.27%, while the six rotor cases in the short configuration had an average discrepancy of 2.47%. Overall, CHARM predicts closer performance results at smaller shaft angles (0 degrees being the best), in the short configuration, and with slower free field velocity when compared with the experimental data in the wind tunnel. These results indicate the need for a more in-depth investigation in input file settings.

**Table 4.11:** Discrepancy between the CHARM prediction and experimental data for six rotors in short and tall configurations at forward flight in free field

Discrepancy of Ave. Thrust	Discrepancy of Ave. Power	Pitch [Deg]	V [ft/s]	Configuration
+1.04%	+2.88%	-10	20	Short
-1.65%	-1.13%	-5	20	Short
+0.57%	+ 0.43%	0	20	Short
-3.45%	+0.54%	-10	40	Short
-1.94%	+ 3.84%	-5	40	Short
-2.94%	+ 6.01%	0	40	Short
-4.63%	-4.16%	-10	20	Tall
-1.57%	-2.78%	-5	20	Tall
+1.33%	+ 1.22%	0	20	Tall
-6.11%	+23.4%	-10	40	Tall
+2.52%	+10.65%	-5	40	Tall
-0.03%	+12.62%	0	40	Tall



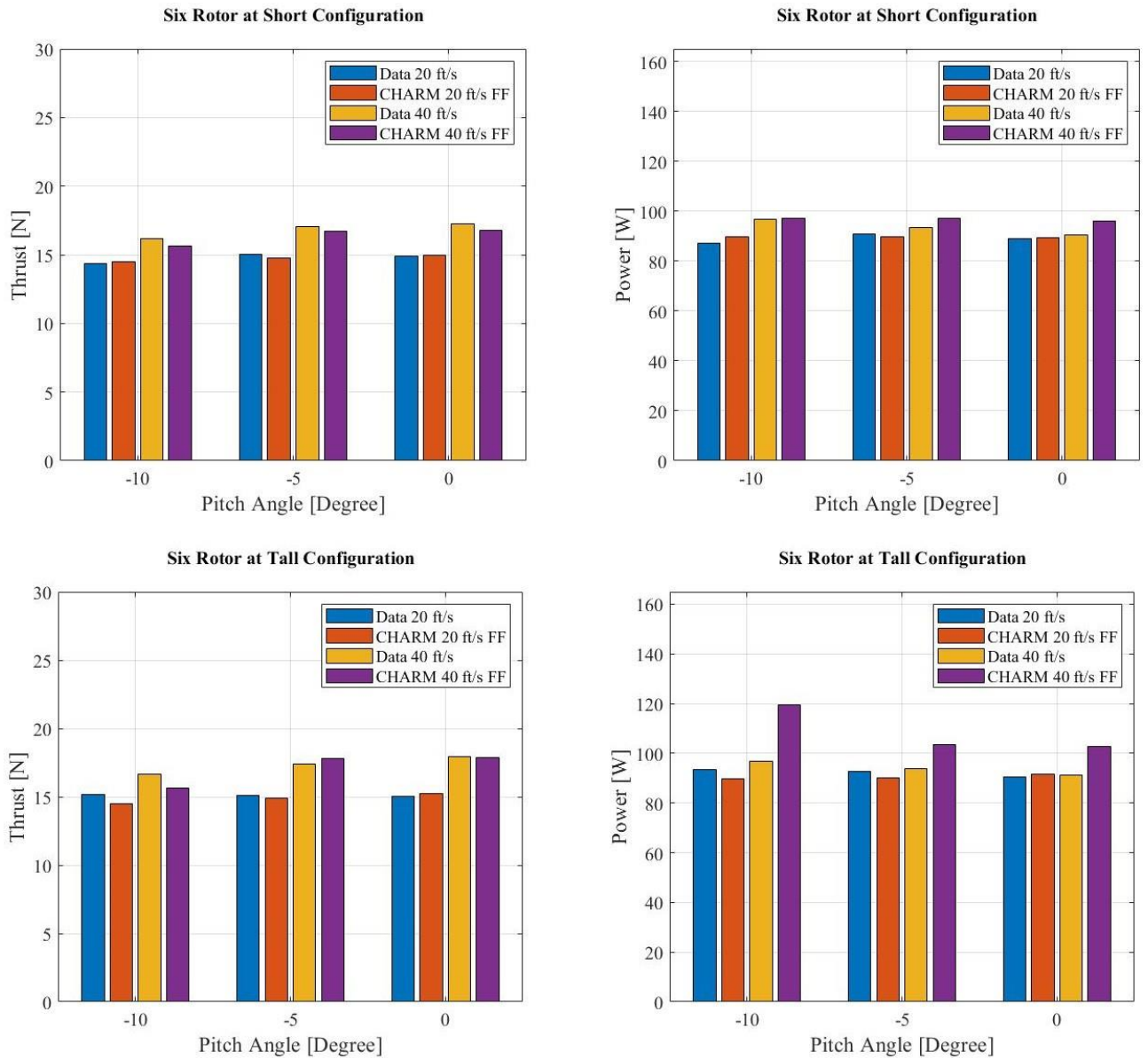


**Figure 4.28:** Six rotors at short and tall configurations in free field - thrust and power vs. pitch angle - forward speeds of 20 ft/s and 40 ft/s

---

# CHAPTER 5

---

## Discussion

This chapter compares the CHARM simulation results for free field and wall bounded wind tunnel conditions with experimental data. The rotor wake interaction was then studied using four and six rotor cases by comparing the CHARM wind tunnel prediction to test data for front (rotors 1 and 2), middle (rotors 3 and 4), and back rotors (rotors 5 and 6). CHARM uses the CVC method to improve the wake geometry (as described in Chapter 2) and the induced velocity predictions while allowing better predictions of the swirl velocity profile and rolled up wakes. This chapter provides the result for free field simulations to better understand CHARM's capability to predict these wake interactions.

### 5.1. Multirotor Test Bed in Wind Tunnel and Free Field Results comparison to Experiments

Comparing free field CHARM simulations with wind tunnel prediction results shows a difference that could indicate wall effect. Figure 5.1 shows the experimental data, CHARM wind tunnel and CHARM free field predictions for a single rotor in forward flight. The similarity of thrust results for the free field and wind tunnel simulations suggests that there is no wall effect on thrust between the two types of simulations, whether it is in the wind tunnel or not, for a single rotor. These results also show that CHARM is better at power predictions at the lower forward speed, 20 ft/s than, predictions at 40 ft/s. The experimental data also indicates at the lower pitch angle, using the same amount of power, more thrust will be generated.

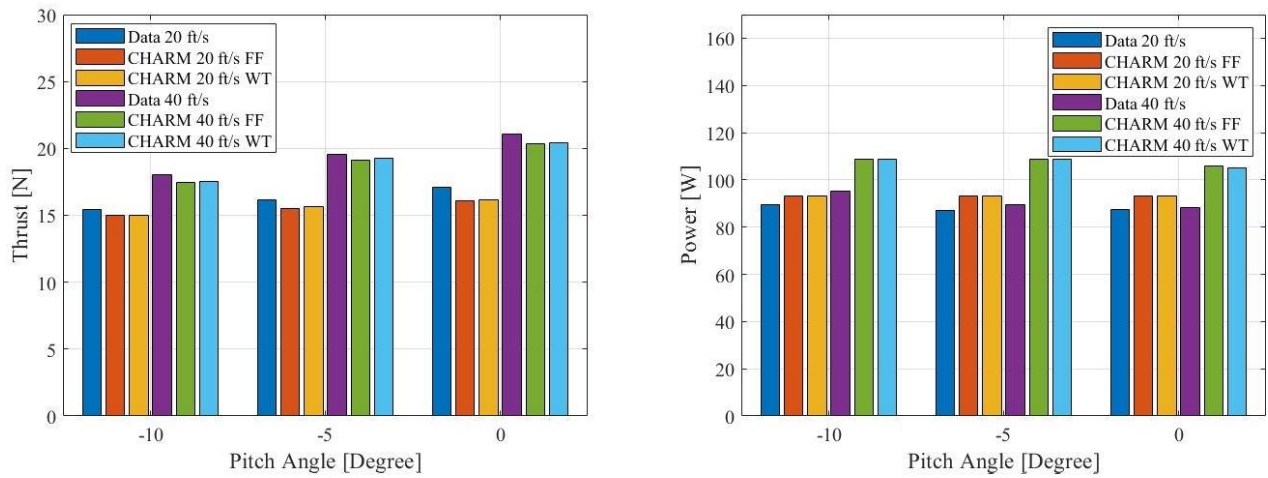


**Figure 5.1:** Single rotor at short configurations - thrust and power vs. pitch angle

Figure 5.2 compares the average thrust and average power from experimental data, free field simulations, and wind tunnel simulations for the two rotor cases at various pitch angles. The difference between wind tunnel and free field simulation results is less than 1%, indicating no wall effect presence in the two rotor cases. CHARM predicts better results for thrust than power, even though there is a tendency of underprediction of thrust and overprediction of power.

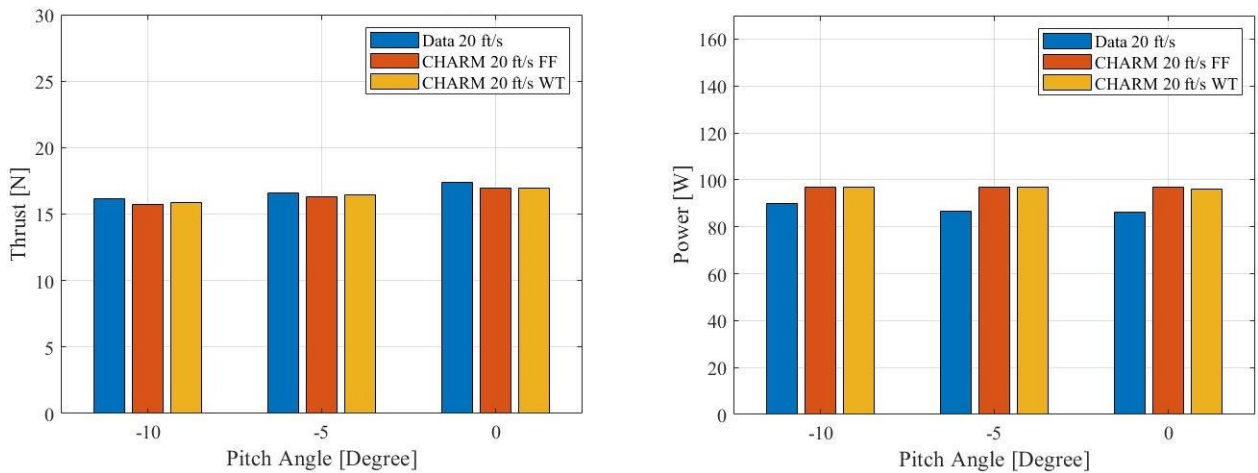


**Figure 5.2:** Two rotors at short configurations - thrust and power vs. pitch angle

Four rotor simulation results indicate the presence of a wall effect on the experimental data, as shown in Figure 5.3. The average thrust discrepancy between predicted wind tunnel results and experimental data is 2.69%, while this value for free field simulation and experimental data is 4.15%. In measured

experimental data, thrust values were increased by decreasing the pitch angle due to going from negative stall to a 0 degree pitch angle; therefore, less drag was generated, and less power was required. But this distinct trend was not identified in either of the CHARM results.

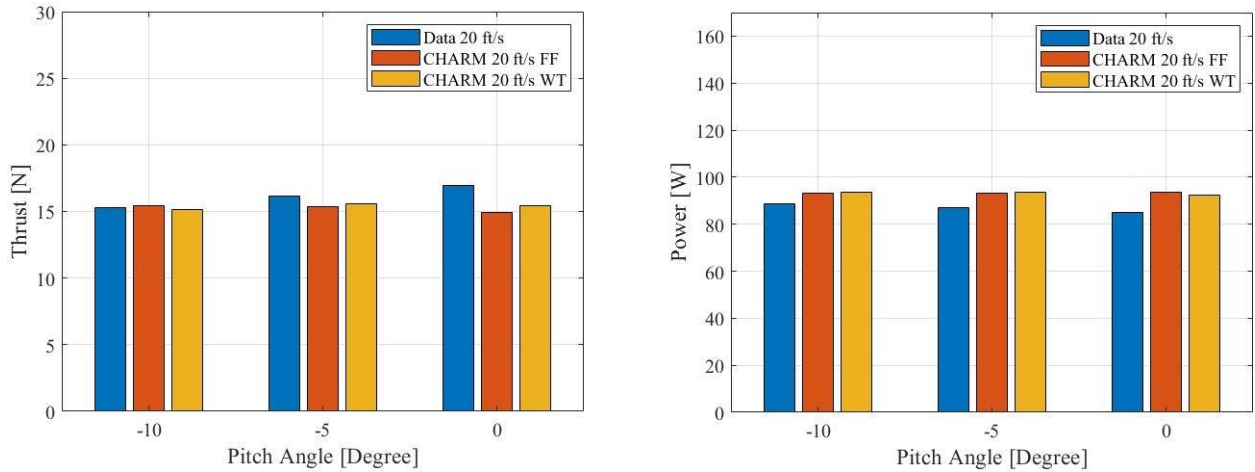


**Figure 5.3:** Four rotors cases in short configurations - thrust and power vs. pitch angle

Figures 5.4 and 5.5 compare the CHARM the wind tunnel and free field prediction for six rotor cases in the short and tall configurations. The free field predictions show better agreement with experimental data, with an average discrepancy of 1.93% and 2.47% for average thrust and average power, respectively in the short configuration (shown in Table 6.1). The free field simulation results have better agreement with the wind tunnel data at 20 ft/s forward flight in the tall configuration. The average discrepancy of free field cases in the tall configuration is 2.70% for thrust and 9.15% for power. This result indicates that the wind tunnel presence has a smaller effect on the experimental results at the lower speed.

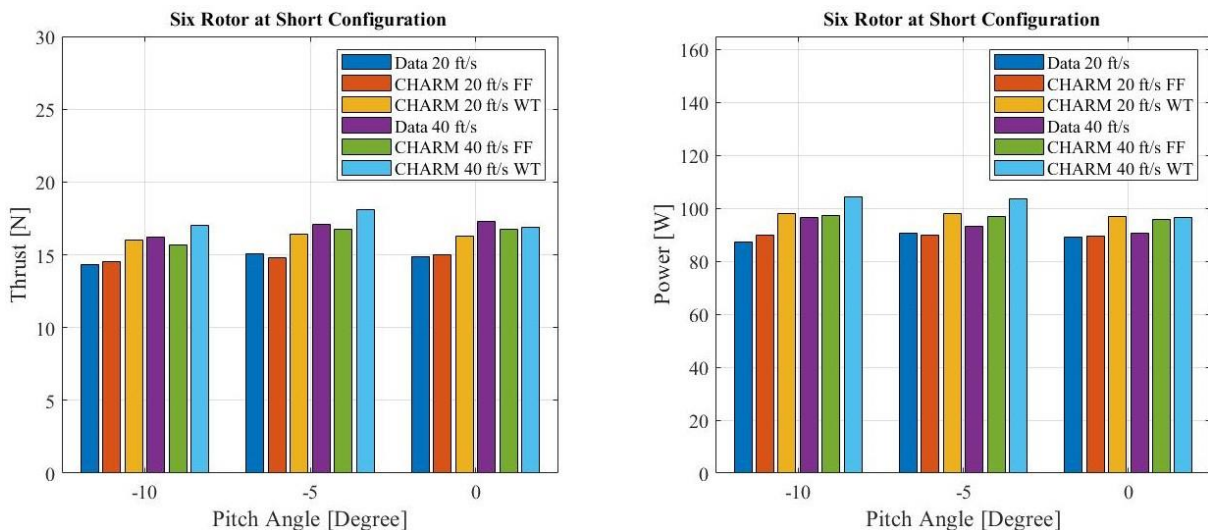


**Figure 5.4:** Six rotor cases in the short configurations - thrust and power vs. pitch angle

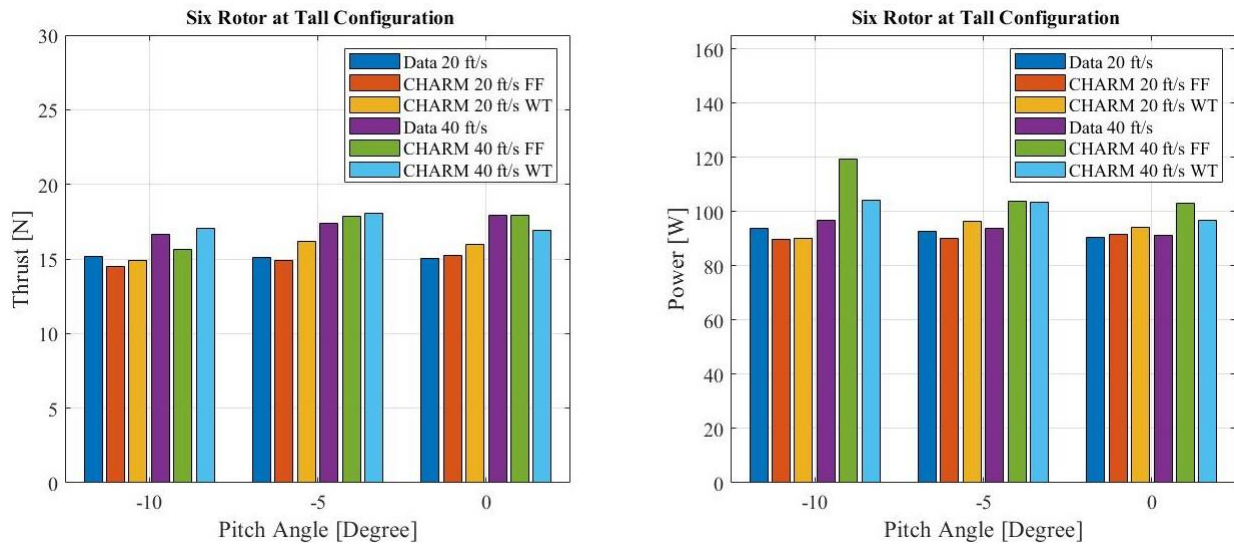


**Figure 5.5:** Six rotors cases in the tall configurations - thrust and power vs. pitch angle

## 5.2. Wake Effect

CHARM uses the potential flow method to compute multiple rotor performance results and the interaction between the rotors and the rotor wake [16]. If the rotors are too close to one another, each rotor's wake can add to the other rotor's wake, creating a roll up effect. This phenomenon can alter (local) performance of the rotor blades and instability in flight quality. In this section, rotor interaction is studied using the experimental and simulation data from MTB in the wind tunnel of the four rotor and six rotor cases. It was expected to see a higher wake roll up at the 0 degrees shaft angle, since the rotors were placed behind one another.

The 3D Vortex-X visualizations of the rotor wake interactions for these cases can be found in Appendix B. Figure 5.6 shows the comparison between the experimental data and wind tunnel simulation data at a forward flight speed of 20 ft/s for the four rotor cases. The average thrust and power presented in these plots belong to the front rotors, rotors# 1 and 2, and the middle rotors, rotors# 3 and 4. As seen before, CHARM overpredicts the power (depicted by the solid lines in Figure 5.6) and underpredicts thrust results, except for the middle rotor thrust value at the -10 degrees pitch angle. Figure 5.6 also indicates the front rotors generate higher thrust at 0 degrees pitch angle.

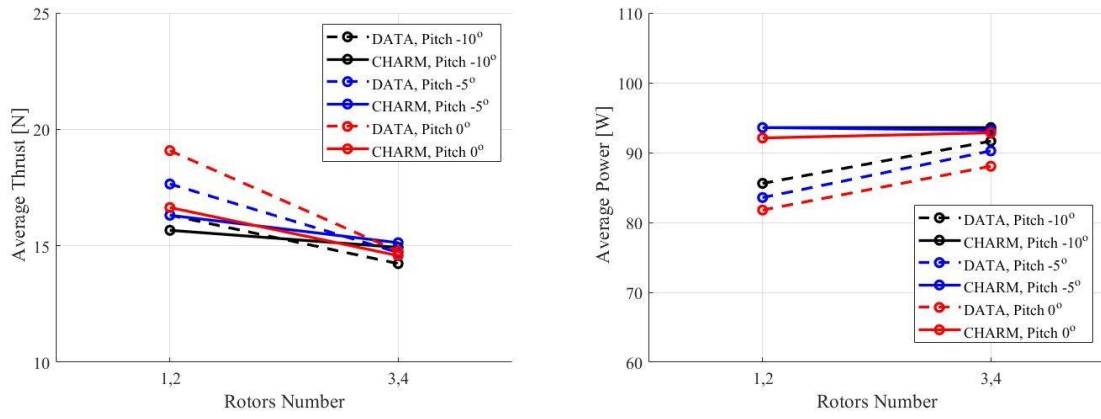


**Figure 5.6:** Four rotor case - rotor interactions - forward flight speed 20 ft/s

Even though the thrust results have a 13.1% lower prediction for the front rotor performance compared to experimental data. Experimental data also show that the middle rotors required  $\sim 6.6\%$  more power to provide  $\sim 87\%$  of the thrust of the front rotors. Overall, CHARM predicts the thrust and power values of the middle rotors close to the experimental data for the four rotor cases. The average thrust discrepancies of the front rotors and middle rotors are 8.1% and 3.02%, shown in Table 5.1. Besides, experimental data shows more sensitivity to the change of pitch angle and the rotor location when compared to the CHARM predictions.

**Table 5.1:** Thrust and power discrepancies between simulations and experimental data for front and middle rotors in four rotors case

Pitch [Deg]	Thrust	Thrust	Power	Power
	Rotors#1,2	Rotors#3,4	Rotors#1,2	Rotors#3,4
-10	4.0%	4.9%	2.1 %	2.1%
-5	7.6%	2.9%	3.7 %	3.3%
0	12.8%	1.3%	4.6%	5.4%

The thrust and power performance versus rotor location for the six rotor cases in the short/tall configuration and at forward flight speed of 20 and 40 ft/s appear in Figure 5.7. Experimental data demonstrates that the front rotors generate higher thrust in the short and tall configuration, as shown in Figure 5.7 (a1-d1). Also, the fact that the thrust decreases after the stream passes by the two front rotors in the measured data shows that the front rotor wakes interact with the rotors behind them; therefore, the thrust generated by the middle and also the back rotors decreases

while power consumption increases, shown in Figure 5.7 (a2-d2). This data shows that the back rotors (rotors five and six) generate  $\sim 25.2\%$ ,  $\sim 14.8\%$ , and  $\sim 9.73\%$  less thrust for respective pitch angles of 0, -5, and -10 degrees compared to the front rotors. However, rotors in the back require  $\sim 3.55\%$ ,  $\sim 3.22\%$ , and  $\sim 2.68\%$  more power at respective pitch angles of 0, -5, and -10 degrees, compared to front rotors. Note that these differences are small and so the changes are not dramatic for the conditions studied. Tables 5.2 and 5.3 show the average thrust and power discrepancies between the simulated and experimental data with respect to rotor location. The average absolute thrust discrepancies of the front, middle, and back rotors are 4.3%, 6.4%, and 10.8%; accordingly, average power discrepancies are 13.5%, 6.8%, and 3.6%. Similar to experimental data, CHARM results indicate that the front rotor wake interacts with middle and back rotors. The wake interaction observed with 3D visualization images indicates that the front rotor wake influences the back rotor wake at the 0 degrees pitch angle, shown in Figure 5.8 (a,b). At the 0 degrees pitch angle, the front rotor wakes were added to middle rotor wakes, then reached the back rotor wakes and caused roll up. These wake interactions had less impact on performance at -5 and -10 degree pitch angles, particularly in CHARM simulations shown in Figure 5.8 (c,d). The difference is slightly better for the 40 ft/s forward flight speed, seen in Figure 5.7 (c1-2, d1-2).



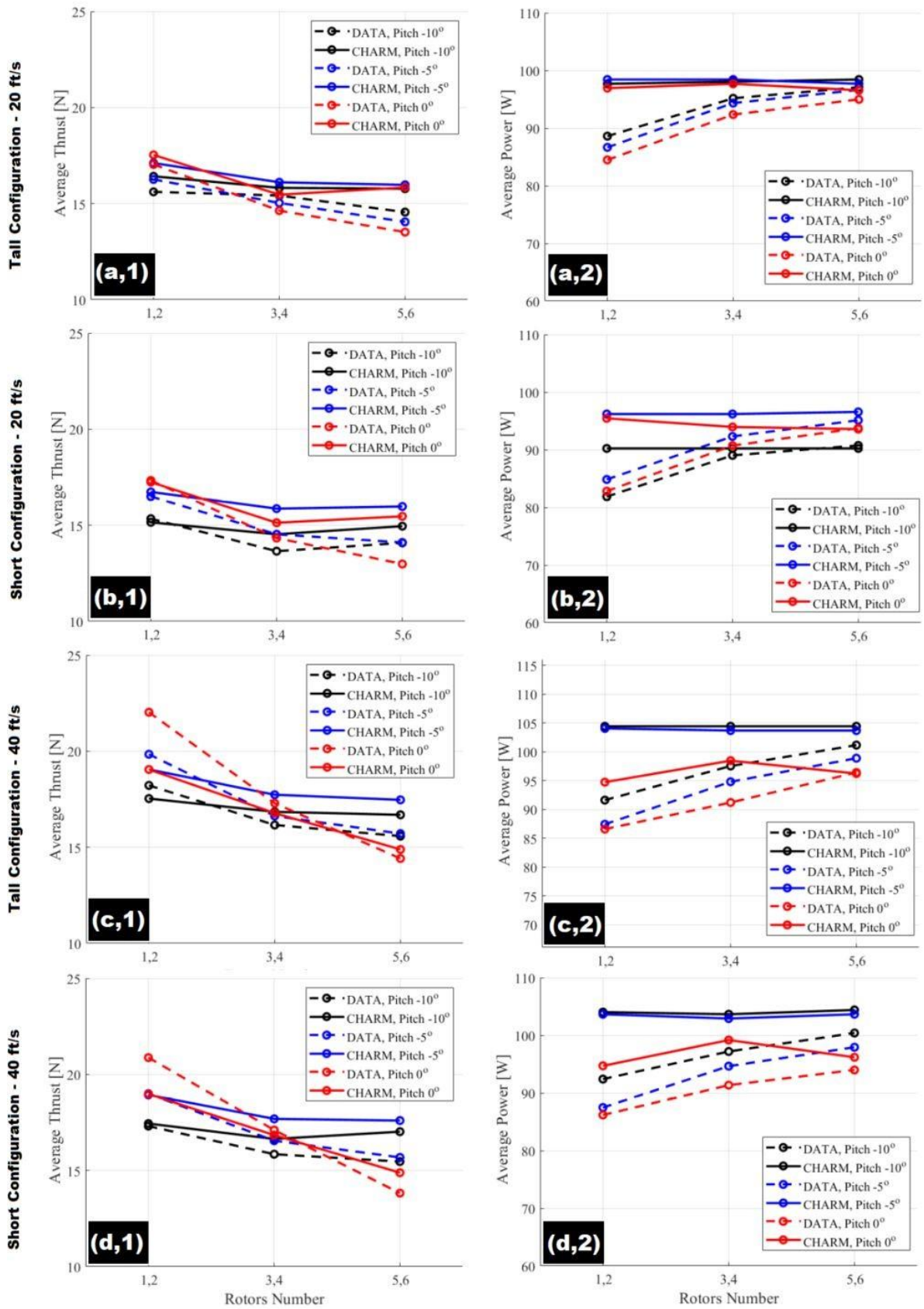
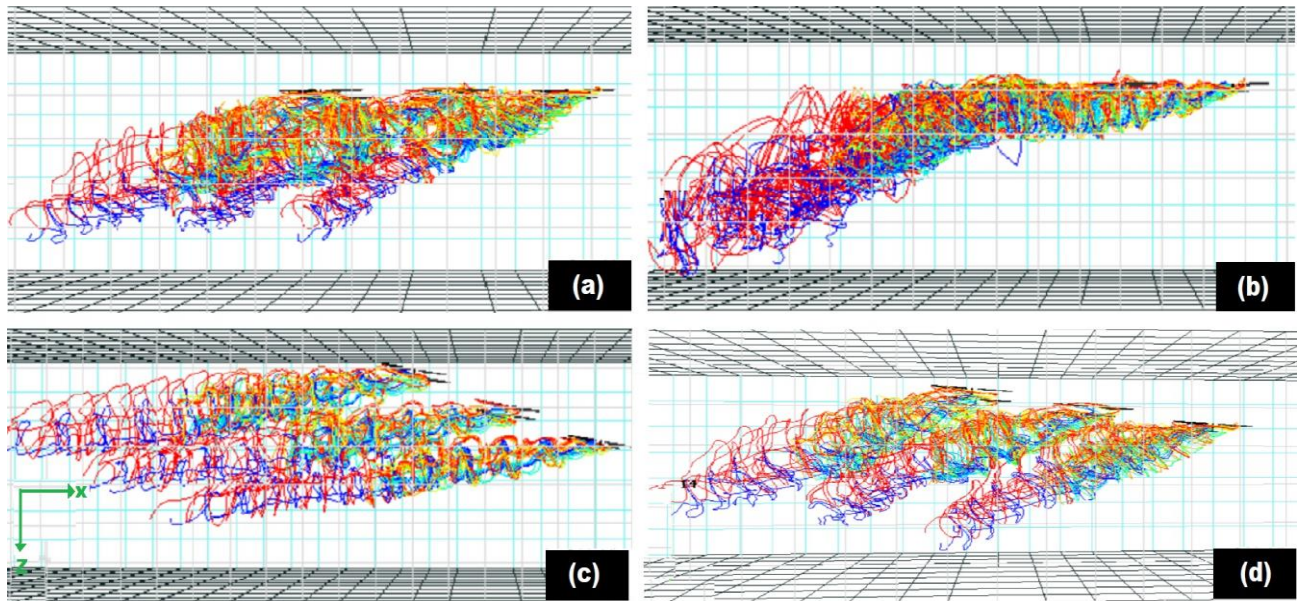


Figure 5.7: Six rotor cases in short and tall configurations - rotor wake interactions - forward flight speeds 20 and 40 ft/s





**Figure 5.8:** Six rotor wake interactions at (a) 0 degree pitch and 20 ft/s, (b) 0 degree pitch and 40 ft/s, (c) -10 degree pitch and 20 ft/s, and (d) -5 degree pitch and 20 ft/s

Figure 5.8 (a,b) shows that the front rotor wakes convected downstream faster at 40 ft/s forward flight than under the lower velocity condition, which increases wake interaction with the rotors behind them. This behavior explains the more significant difference between the thrust value of the front rotors and back rotors at 40 ft/s forward flight, Figure 5.7(c1, d1). Predicted thrust and power values were expected to be closer to experimental data for the front rotors. However, the average absolute power discrepancy for these rotors was between 9.89% and 19.31%, indicating further evaluation of CHARM input file settings is required to better predict the KDE performance in forward flight.

**Table 5.2:** Absolute discrepancy of average thrust and power between prediction and experimental data for front, middle, and back rotors of six rotor cases in the short configuration

Pitch Deg	Velocity [ft/s]	Thrust			Power		
		Rotor#1,2	Rotor#3,4	Rotor#5,6	Rotor#1,2	Rotor#3,4	Rotor#5,6
-10	20	7.04%	15.9%	12.0%	19.3%	10.1%	8.46%
-5	20	3.70%	10.9%	13.3%	16.0%	6.63%	2.69%
0	20	1.16%	7.90%	22.0%	17.1%	7.68%	3.00%
-10	40	1.29%	6.27%	7.90%	12.9%	7.41%	3.98%
-5	40	0.25%	7.13%	11.38%	18.9%	9.51%	5.84%
0	40	8.77%	1.94%	7.66%	9.89%	7.75%	2.34%

**Table 5.3:** Absolute discrepancy of average thrust and power between prediction and experimental data for front, middle, and back rotors of six rotor cases in the tall configuration

Pitch Deg	Velocity [ft/s]	Thrust	Thrust	Thrust	Power	Power	Power
		Rotor#1,2	Rotor#3,4	Rotor#5,6	Rotor#1,2	Rotor#3,4	Rotor#5,6
-10	20	2.94%	5.77%	2.71%	1.83%	5.20%	7.07%
-5	20	2.91%	5.52%	13.7%	10.9%	1.96%	0.07%
0	20	1.21%	3.38%	14.4%	12.9%	1.74%	1.48%
-10	40	4.25%	3.00%	9.26%	13.6%	6.31%	3.23%
-5	40	4.56%	6.39%	12.0%	18.6%	8.58%	4.85%
0	40	13.8%	2.58%	3.26%	9.41%	8.78%	0.19%

---

# CHAPTER 6

---

## Conclusion and Future Work

CHARM uses the vortex panel method to calculate wind tunnel effects and uses the Hierarchical Fast Vortex approach to model wakes and determine aerodynamic interactions. CHARM uses far less CPU and memory than fully resolved CFD simulations. In this study, CHARM capabilities were validated using SUI and UH-60A rotor experimental data mainly at forward flight conditions. Further, CHARM simulations were accomplished in the 7- by 10-Foot Wind Tunnel test section boundary and free field for the MTB project. All CHARM simulations did not consider the test stand effect, and still, the outcomes were promising.

### 6.1. Conclusion

Table 6.1 and Table 6.2 show the average and maximum discrepancy between the simulation results, wind tunnel and free field, and experimental data. The wind tunnel simulation results had an average discrepancy of 3.96% for thrust and 9.01% for power over 24 simulated cases; moreover, the predicted result in the free field had an average discrepancy of 2.62% and 8.25%, respectively, for thrust and power. These results indicate CHARM's capability to predict the thrust value of single, two, and four rotor cases with discrepancies less than 10%. CHARM simulation results in the free field and wind tunnel indicate the presence of a wall effect on the six rotor cases results. To conclude, CHARM predicts thrust better than power for most of the cases due to the challenge of incorporating the mechanical loss accurately. The prediction of the wind tunnel and free field results, for this study, are very close to each other. This demonstrates that one can simply choose either the wind tunnel or free field set up, whichever has faster computation time for future reference. However, the KDE rotor

size was selected with the assumption that the rotor is small enough to avoid any impact of wall effects on the rotor performance. Simulation and experimental results for the MTB project were preliminary, and the experimental data can change when the final experimental data is obtained; nevertheless, the results in this study allow for a better understanding of the rotor interactions for the MTB project, and help create an efficient test matrix for the second wind tunnel test, which is planned for Fall 2021.

**Table 6.1:** Absolute average discrepancy between CHARM wind tunnel and free field prediction and experimental data

Cases	Thrust (WT)	Power (WT)	Thrust (FF)	Power (FF)
Single Rotor	1.96%	12.1%	2.54%	12.3%
Two-Rotor	0.91%	10.3%	1.11%	10.6%
Four-Rotor	3.59%	7.32%	5.53%	7.55%
Six-Rotor (Short)	7.15%	9.21%	1.93%	2.47%
Six-Rotor (Tall)	4.49%	5.92%	2.70%	9.15%

**Table 6.2:** Absolute maximum discrepancy between CHARM wind tunnel and free field prediction and experimental data

Cases	Thrust (WT)	Power (WT)	Thrust (FF)	Power (FF)
Single Rotor	4.25%	21.5%	5.03%	21.5%
Two-Rotor	1.54%	11.8%	1.70%	12.3%
Four-Rotor	7.78%	8.89%	10.6%	10.2%
Six-Rotor (Short)	11.4%	12.4%	3.45%	6.01%
Six-Rotor (Tall)	7.12%	10.4%	6.11%	23.46%

## 6.2. Future Work

The future experimental and computational results for MTB can be improved with some investigation.

- **CHARM Improvement**

Including the MTB structural test stand in CHARM simulations can slightly change the prediction values. There is no expectation of aerodynamic changes in the presence of test stands in simulation, aside from possible changes in drag. Due to the absence of wind tunnel surface panels and the MTB test stand, the same results were expected for six-rotor cases in the tall and short configurations in the free field. Nevertheless, the average power and thrust were slightly higher in the tall configuration, which indicates CHARM input files need further improvements. For example, the *blade dynamics* input file can be improved by measuring and including data such as the KDE blade frequency. Also, including noise prediction in CHARM study using NASA's WOPWOP or PSU-WOPWOP [56] code can improve predictions by setting parameter *NOISE* = 20 in the run characteristics input file. In addition, inaccuracies in the airfoil tables could have resulted in discrepancies. Refining the airfoil tables could improve the correlation between CHARM simulations and experimental data. Moreover, the RPM recorded in experimental data is not an exact value; therefore, these differences need to be considered in CHARM simulations. Furthermore, having more experimental data for the isolated rotor in hover allows for a better understanding and more accurate prediction of the KDE rotor behavior.

- **Experimental**

A potential source of error could be the load cells, suggesting that recalibration is required to minimize possible errors in data measurement. Also, the geometric dimensions of one KDE rotor were used to create the airfoil tables. All six KDE rotors need to be laser scanned to calibrate the geometry difference between the rotors. The simulation results also indicate a wall effect; therefore, testing the MTB in a larger wind tunnel with the same size rotor could improve data measurements.

## References

1. Russell, C. & et al. Multicopter UAS Performance Test 2 in (NASA/TM—TBD.).
2. Russell, C., Willink, G., C., T. & Glasner, B. Wind Tunnel and Hover Performance Test Results for Multicopter UAS Vehicles in NASA/TM—2018-219758 (2018).
3. Conley, S. Design of the Multirotor Test Bed for Load and Acoustic Measurements (2019).
4. Conley, S. & Russell, C. Mechanical Design of the Multirotor Test Bed in Vertical Flight Society Aeromechanics for Advanced Vertical Flight Technical Meeting, San Jose, CA (2020).
5. Russell, C. Multirotor Test Bed (MTB) Test Design Review, July 31, 2019 (Image Credit).
6. Russell, C. & Conley, S. The Multirotor Test Bed – A New NASA Test Capability for Advanced VTOL Rotorcraft Configurations in presented at the Abstract accepted to VFS 76th Annual Forum and Technology Display, Montréal, QC, Canada (2020).
7. Johnson, W. CAMRAD II Comprehensive Analytical Model of Rotorcraft Aerodynamics and Dynamics—Theory Manual. Johnson Aeronautics, Palo Alto, California (1993).
8. Perez Perez, B. N. Forward flight rotor performance at martian atmospheric densities and sensitivity to low Reynolds numbers (2020).
9. Whitehouse, D. A. W. T. R. Q. A. H. B. M. K. Y. G. R. CHARM User's Manual (Version 6.4) in (May 2018).
10. Drela, M. An Analysis and Design System for Low Reynolds Number Airfoils in Lecture Notes in Engineering (1989).
11. Drela, M. XFOIL: An Analysis and Design System for Low Reynolds Number Airfoils in presented at the Conference on Low Reynolds Number Airfoil Aerodynamics, University of Notre Dame (Jun. 1989).
12. BLOCK, T.-A. C. Automated CFD for Generation of Airfoil Performance Tables.

- NASA Tech Briefs, 33 (2009).
13. Quackenbush, T. R., Keller, J. D. & Whitehouse, G. R. Analysis Methods for Advanced V/STOL Configurations in the 72nd AHS Annual Forum, West Palm Beach, FL (2016), 329–345.
  14. Quackenbush, T., Wachspress, D., Boschitsch, A. & Curbishley, T. A comprehensive hierarchical aeromechanics rotorcraft model (CHARM) for general rotor/surface interaction. CDI Report, 99–03 (1999).
  15. Wachspress, D. A., Quackenbush, T. R. & Boschitsch, A. H. First-principles free-vortex wake analysis for helicopters and tiltrotors in ANNUAL FORUM PROCEEDINGS-AMERICAN HELICOPTER SOCIETY (2003), Page:1763–1786.
  16. Choi, J., Summers, M. & Corrigan, J. Validation of CHARM Wake Methodology for Computation of Loads and Vibrations in 65th Annual Forum of the American Helicopter Society (2009).
  17. A H Boschitsch W J Jr Usab, R. J. E. Fast Lifting Panel Method in AIAA-99- 3376, AIAA 14th Computational Fluid Dynamics Conference, Norfolk, VA (1999).
  18. Wachspress, D. A., Quackenbush, T. R. & Boschitsch, A. H. Rotorcraft interactional aerodynamics calculations with fast vortex/fast panel methods in ANNUAL FORUM PROCEEDINGS-AMERICAN HELICOPTER SOCIETY 56 (2000), 51–71.
  19. Boschnitsch, A., Usab Jr, W. & Epstein, R. Fast lifting panel method in 14th Computational Fluid Dynamics Conference (1999), 3376.
  20. AeroToolBox. Angle of Attack. <https://aerotoolbox.com/angle-of-attack/> (2017).
  21. Service, U. D. O. T. F. A. A. F. S. Rotorcraft Flying Handbook. <https://rotorcraft.arc.nasa.gov/faa-h-8083-21.pdf>, FAA-H-8083–21 (2000), last accessed December 15, 2020.
  22. Koning, W. J. Generation of Performance Model for the Aeolian Wind Tunnel (AWT) Rotor at Reduced Pressure (2018).
  23. Acree, C., Price, G. & Rutkowski, M. Rotor Design Options for Improving V-22 Whirl-Mode Stability in (2001).
  24. Johnson, W., “Technology Drivers in the Development of CAMRAD II,” American Helicopter Society Aeromechanics Specialist Meeting, San Francisco, California, January 1994.
  25. Box, A. T. Sweep Angle and Supersonic Flight. <https://aerotoolbox.com/intro-sweep-angle/> (Image Credit).
  26. NASA Glenn Research Center, Kid pages, “Wing Geometry Definitions”,

- <https://www.grc.nasa.gov/www/k-12/airplane/geom.html>, last accessed December 15, 2020 (Image Credit).
27. Parts of an airplane, NASA, Grade 9-12, [https://www.nasa.gov/sites/default/files/atoms/files/parts\\_of\\_an\\_airplane\\_9-12.pdf](https://www.nasa.gov/sites/default/files/atoms/files/parts_of_an_airplane_9-12.pdf), last accessed December 15, 2020.
  28. T.H.G., M. Strip Theory. Aircraft Structures for Engineering Students (Sixth Edition) (2017).
  29. Miranda, L. R., Elliot, R. D. & Baker, W. M. A generalized vortex lattice method for subsonic and supersonic flow applications (1977).
  30. Smith Willard G., L. F. A. Experimental and Theoretical Study of a Rectangular Wing in a Vortical Wake at Low Speed (2013).
  31. Castillo-Rivera, S. & Tomas-Rodriguez, M. Helicopter flap/lag energy exchange study. *Nonlinear Dynamics* 88. (June 2017).
  32. Training, H. F. “Learn to Fly Helicopters”. [www.danubewings.com/fully-articulated-rotor-system/](http://www.danubewings.com/fully-articulated-rotor-system/), 2020
  33. Training, H. F. “Learn to Fly Helicopters”, 2020
  34. StackExchange. How does the a movement of the cyclic control stick in a helicopter affect the swashplate? in aviation (2020).
  35. Meyn, L. ResearchGate. [https://www.researchgate.net/figure/UH-60A-airloads-rotor-in-NFAC-40-by-80-Foot-Wind-Tunnel\\_fig1\\_265050941](https://www.researchgate.net/figure/UH-60A-airloads-rotor-in-NFAC-40-by-80-Foot-Wind-Tunnel_fig1_265050941), last accessed December 15,2020 (Image Credit).
  36. Halder, A. & Benedict, M. Free-Wake Based Nonlinear Aeroelastic Modeling of Cycloidal Rotor in AIAA Aviation 2019 Forum (2019), 3245.
  37. Wood, D. & Meyer, C. Two methods for calculating the velocities induced by a constant diameter far-wake. *Journal of aircraft* 28, 526–531 (1991).
  38. AIAA. Aviation 2019 Forum. paper 20 number 2010.2514- 6.2019- 3245 (Image Credit).
  39. Ostrowski, A. On over and under relaxation in the theory of the cyclic single step iteration. *Mathematical Tables and other Aids to Computation* 7, 152–159 (1953).
  40. Moffett, C. RotCFD Analysis of a Multirotor Test Bed in Aeromechanics Summer Intern Program (Aug 2018).
  41. Shinoda, P. M., Yeo, H. & Norman, T. R. Rotor performance of a UH-60A rotor system in the NASA Ames 80-by 120-foot wind tunnel. *Journal of the American Helicopter Society* 49, 401–413 (2004).
  42. Johnson, W. CAMRAD II Comprehensive Analytical Model of Rotorcraft



- Aerodynamics and Dynamics—Theory Manual. Johnson Aeronautics, Palo Alto, California (1993).
43. Jones, H. E. & Kunz, D. L. Comprehensive modeling of the Apache with CAMRAD II (2001).
  44. Yeo, H. ResearchGate. [https://www.researchgate.net/figure/UH-60-Rotor-System-installed-on-Large-Rotor-Test-Apparatus-in-the-Ames-80-by-120-Foot\\_fig1\\_228890678](https://www.researchgate.net/figure/UH-60-Rotor-System-installed-on-Large-Rotor-Test-Apparatus-in-the-Ames-80-by-120-Foot_fig1_228890678), , last accessed December 15, 2020 (Image Credit).
  45. Russell, C., Theodore, C. R. & Sekula, M. K. Incorporating Test Data for Small UAS at the Conceptual Design Level in (2018).
  46. Russell, C. & Sekula, M. K. Comprehensive Analysis Modeling of Small- Scale UAS Rotors in (NASA Ames Research Center).
  47. Russell, C. R., Jung, J., Willink, G. & Glasner, B. Wind tunnel and hover performance test results for multicopter UAS vehicles (2016).
  48. Weber, J. The Calculation of the Pressure Distribution over the Surface of Two-dimensional and Swept Wings with Symmetrical Aerofoil Sections in Aeronautical Research Council Reports and Memoranda (1956).
  49. Quackenbush, T., Keller, J., Wachspress, D. & Boschitsch, A. Reduced order free wake modeling for near real time simulation of rotorcraft flight mechanics in ANNUAL FORUM PROCEEDINGS-AMERICAN HELICOPTER SOCIETY 55 (1999), 481–497.
  50. Quackenbush, T., Boschitsch, A., Wachspress, D., McKillip Jr, R. & MacNichol, A. Fast analysis methods for surface-bounded flows with applications to rotor wake modeling in AHS 52nd Annual Forum (1996), 1514–1531.
  51. Sarah, C. Comparing RotCFD Predictions of the Multicopter Test Bed with Experimental Results (2020).
  52. Russell, C. Image Credit for Axial view of KDE rotor in Research Aerospace Engineer, Aeromechanics Office, NASA, ARC, Moffett Field (2020).
  53. IVAO. International Virtual Aviation Organisation. <https://www.ivaio.aero/>, last accessed December 15, 2020
  54. Shirey, J., Brentner, K. & Chen, H.-n. A Validation Study of the PSU-WOPWOP Rotor Noise Prediction Code in 45th AIAA Aerospace Sciences Meeting and Exhibit (2007).
  55. D. Jepson, R. Moffitt, K. Hilzinger, and J. Bissell, “Analysis and Correlation of Test Data From an Advanced Technology Rotor System”, Contract NAS2-10211, August 1983, Page 17
  56. William G. Bousman, “Aerodynamic Characteristics of SC1095 and SC1094 R8

Airfoils”, December 2003

57. S. Jon Davis, “Predesign Study For a Modern 4-Bladed Rotor For The RSRA”, NASA Contractor Report 166155, March 1981
58. Karen S. Hamade and Robert M. Kufeld, “Modal Analysis of UH-60 Instrumented Rotor Blades”, NASA Technical Memorandum 4239, 1990
59. J.J. Howlett, “UH-60 Black Hawk Engineering Simulation Program: Volume II- Background Report”, NASA CONTRACTOR REPORT 166310
60. Yamauchi, G. K, and Johnson, W., “Trends of Reynolds Number Effects on Two-Dimensional Airfoil Characteristics for Helicopter Rotor Analyses,” 1983.

# Appendix A

SUI blade geometry for 22 radial stations [46], Page 3.

Section	r (in)	r/R	theta (deg)	chord (in)	t/c (%)	Re
1	0.93	0.12	6.97	0.77	20.80	11,6
2	1.24	0.17	15.97	0.97	15.63	19,500
3	1.55	0.21	21.77	1.18	11.77	29,600
4	1.86	0.25	21.72	1.34	9.76	40,300
5	2.17	0.29	19.91	1.44	8.73	50,500
6	2.47	0.33	18.14	1.49	8.18	59,500
7	2.78	0.37	16.55	1.50	7.88	67,500
8	3.09	0.41	15.28	1.49	7.72	74,5
9	3.40	0.45	14.01	1.46	7.53	80,300
10	3.71	0.49	13.00	1.42	7.38	85,200
11	4.02	0.54	12.18	1.38	7.22	89,700
12	4.33	0.58	11.39	1.33	7.11	93,200
13	4.64	0.62	10.76	1.27	7.04	95,300
14	4.95	0.66	10.24	1.21	7.07	96,900
15	5.26	0.70	9.85	1.14	7.13	97,000
16	5.57	0.74	9.40	1.07	7.26	96,400
17	5.88	0.78	9.07	1.00	7.54	95,100
18	6.19	0.82	8.70	0.93	7.89	93,100
19	6.50	0.87	8.46	0.86	8.30	90,400
20	6.81	0.91	8.29	0.77	8.74	84,800
21	7.11	0.95	8.19	0.67	8.88	77,100
22	7.42	0.99	8.17	0.44	10.15	52,800

**Figure 6.1:** SUI blade geometry

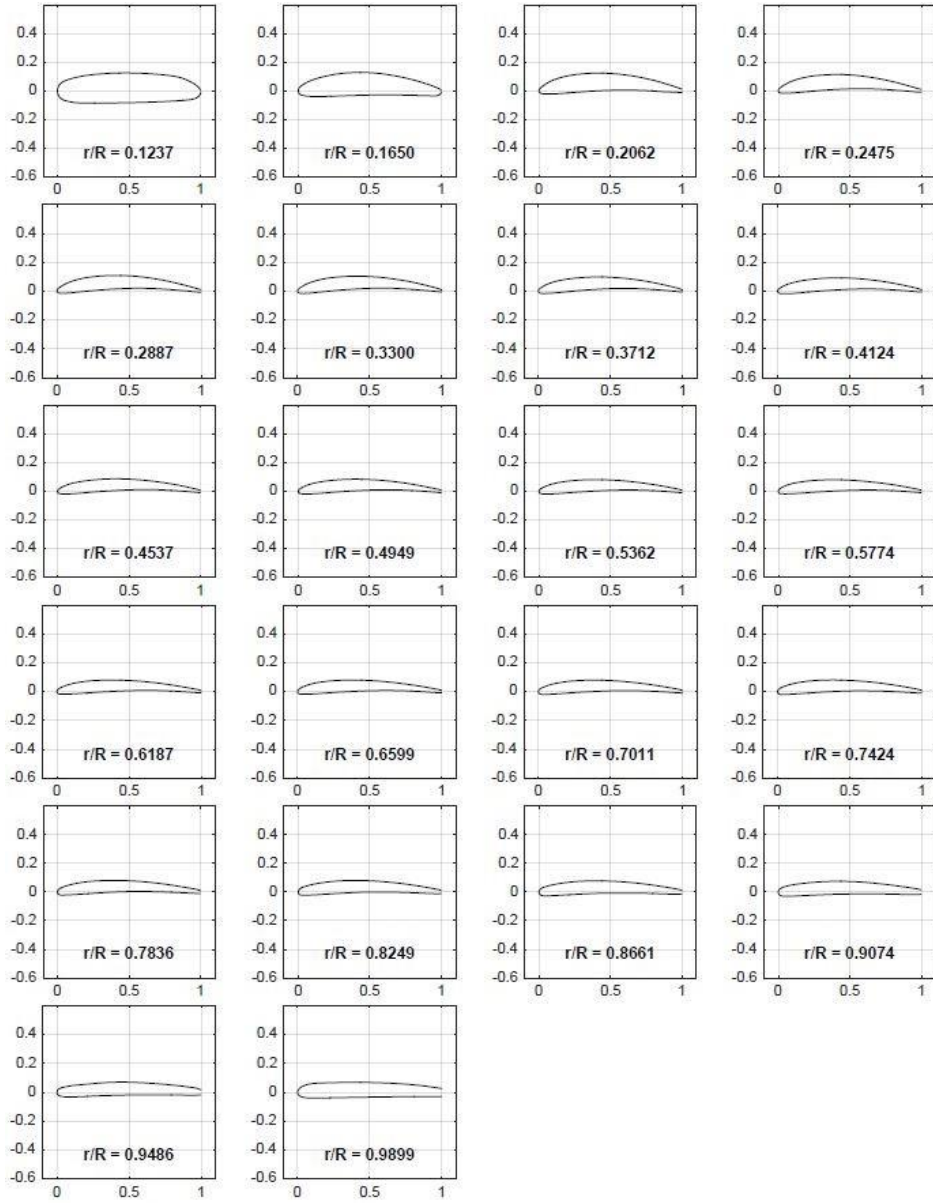


**Figure 6.2:** SU1 airfoil geometry at 22 radial stations [47]

The table below shows the condition of each case that been simulated in this paper. The rotor configuration has been shown by (#, #, #; #, #, #; #, #, #) format, where the first three numbers are the longitudinal location of rotors. The second three values are lateral location and, in the end, vertical location. At each axis location, three positions were inputted for rotors 5 and 6, rotors 3 and 4, and rotors 1 and 2. For example, at the Run#112 Case#7, the rotors 5 and 6 are at aft zero, rotors 3 and 4 are at positive 24 and rotors 1 and 2 are at positive 48.

Run #	Case	Point	Alpha	V	RPM	# of Rotors	Rotors Used	Rotor Configuration
121	1	8	-10	20	2000	1	2 CW	(N/A, N/A, 48; N/A, N/A, 7; N/A, N/A, 0)
121	2	13	-5	20	2000	1	2 CW	(N/A, N/A, 48; N/A, N/A, 7; N/A, N/A, 0)
121	3	24	0	20	2000	1	2 CW	(N/A, N/A, 48; N/A, N/A, 7; N/A, N/A, 0)
122	4	8	-10	40	2000	1	2 CW	(N/A, N/A, 48; N/A, N/A, 7; N/A, N/A, 0)
122	5	10	-5	40	2000	1	2 CW	(N/A, N/A, 48; N/A, N/A, 7; N/A, N/A, 0)
122	6	14	0	40	2000	1	2 CW	(N/A, N/A, 48; N/A, N/A, 7; N/A, N/A, 0)
112	7	8	-10	20	2000	6	1 to 6	(0, 24, 48; 7, 7, 7; 0, 0, 0)
112	8	13	-5	20	2000	6	1 to 6	(0, 24, 48; 7, 7, 7; 0, 0, 0)
112	9	22	0	20	2000	6	1 to 6	(0, 24, 48; 7, 7, 7; 0, 0, 0)
113	10	8	-10	40	2000	6	1 to 6	(0, 24, 48; 7, 7, 7; 0, 0, 0)
113	11	10	-5	40	2000	6	1 to 6	(0, 24, 48; 7, 7, 7; 0, 0, 0)
113	12	14	0	40	2000	6	1 to 6	(0, 24, 48; 7, 7, 7; 0, 0, 0)
102	13	8	-10	20	2000	6	1 to 6	(0, 24, 48; 7, 7, 7; 7, 7, 7)
103	14	8	-5	20	2000	6	1 to 6	(0, 24, 48; 7, 7, 7; 7, 7, 7)
103	15	16	0	20	2000	6	1 to 6	(0, 24, 48; 7, 7, 7; 7, 7, 7)
104	16	10	-10	40	2000	6	1 to 6	(0, 24, 48; 7, 7, 7; 7, 7, 7)
104	17	13	-5	40	2000	6	1 to 6	(0, 24, 48; 7, 7, 7; 7, 7, 7)
104	18	19	0	40	2000	6	1 to 6	(0, 24, 48; 7, 7, 7; 7, 7, 7)
114	19	8	-10	20	2000	4	1 to 4	(0, 24, 48; 7, 7, 7; 0, 0, 0)
114	20	14	-5	20	2000	4	1 to 4	(0, 24, 48; 7, 7, 7; 0, 0, 0)
114	21	24	0	20	2000	4	1 to 4	(0, 24, 48; 7, 7, 7; 0, 0, 0)
116	22	8	-10	20	2000	2	3 and 4	(0, 24, 48; 7, 7, 7; 0, 0, 0)
116	23	13	-5	20	2000	2	3 and 4	(0, 24, 48; 7, 7, 7; 0, 0, 0)
116	24	23	0	20	2000	2	3 and 4	(0, 24, 48; 7, 7, 7; 0, 0, 0)

**Figure 6.3:** Parts and aerodynamic terms of an airfoil



Rotation angle					X' [ft]	Y [ft]	Z' [ft]
0	Tall	0	rightfrw	1	2.995	1.64375	-1.83739
0	Tall	0	leftfrw	2	2.995	-1.58125	-1.83739
0	Tall	0	rightmrw	3	-0.005	1.64375	-1.83739
0	Tall	0	leftmrw	4	-0.005	-1.58125	-1.83739
0	Tall	0	rightbrw	5	-3.005	1.64375	-1.83739
0	Tall	0	leftbrw	6	-3.005	-1.58125	-1.83739
0.087266463	Tall	-5	rightfrw	1	3.292827	1.64375	-1.28576
0.087266463	Tall	-5	leftfrw	2	3.292827	-1.58125	-1.28576
0.087266463	Tall	-5	rightmrw	3	0.338404	1.64375	-1.8067
0.087266463	Tall	-5	leftmrw	4	0.338404	-1.58125	-1.8067
0.087266463	Tall	-5	rightbrw	5	-2.61602	1.64375	-2.32765
0.087266463	Tall	-5	leftbrw	6	-2.61602	-1.58125	-2.32765
0.174532925	Tall	-10	rightfrw	1	3.489928	1.64375	-0.6887
0.174532925	Tall	-10	leftfrw	2	3.489928	-1.58125	-0.6887
0.174532925	Tall	-10	rightmrw	3	0.670853	1.64375	-1.71476
0.174532925	Tall	-10	leftmrw	4	0.670853	-1.58125	-1.71476
0.174532925	Tall	-10	rightbrw	5	-2.14822	1.64375	-2.74082
0.174532925	Tall	-10	leftbrw	6	-2.14822	-1.58125	-2.74082
0	Short	0	rightfrw	1	2.995	1.64375	-1.25405
0	Short	0	leftfrw	2	2.995	-1.58125	-1.25405
0	Short	0	rightmrw	3	-0.005	1.64375	-1.25405
0	Short	0	leftmrw	4	-0.005	-1.58125	-1.25405
0	Short	0	rightbrw	5	-3.005	1.64375	-1.25405
0	Short	0	leftbrw	6	-3.005	-1.58125	-1.25405
0							
0.087266463	Short	-5	rightfrw	1	3.191532	1.64375	-0.71129
0.087266463	Short	-5	leftfrw	2	3.191532	-1.58125	-0.71129
0.087266463	Short	-5	rightmrw	3	0.237109	1.64375	-1.23223
0.087266463	Short	-5	leftmrw	4	0.237109	-1.58125	-1.23223
0.087266463	Short	-5	rightbrw	5	-2.71731	1.64375	-1.75318
0.087266463	Short	-5	leftbrw	6	-2.71731	-1.58125	-1.75318
0.174532925	Short	-10	rightfrw	1	3.290419	1.64375	-0.14054
0.174532925	Short	-10	leftfrw	2	3.290419	-1.58125	-0.14054
0.174532925	Short	-10	rightmrw	3	0.471342	1.64375	-1.1666
0.174532925	Short	-10	leftmrw	4	0.471342	-1.58125	-1.1666
0.174532925	Short	-10	rightbrw	5	-2.34774	1.64375	-2.19266
0.174532925	Short	-10	leftbrw	6	-2.34774	-1.58125	-2.19266

**Figure 6.4:** Rotors location in CHARM simulations

## Appendix B

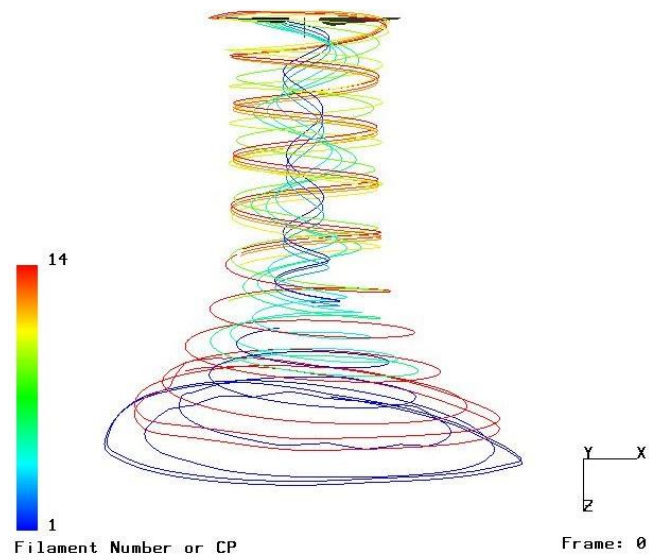


**Figure 6.5:** Isolated KDE rotor at hover

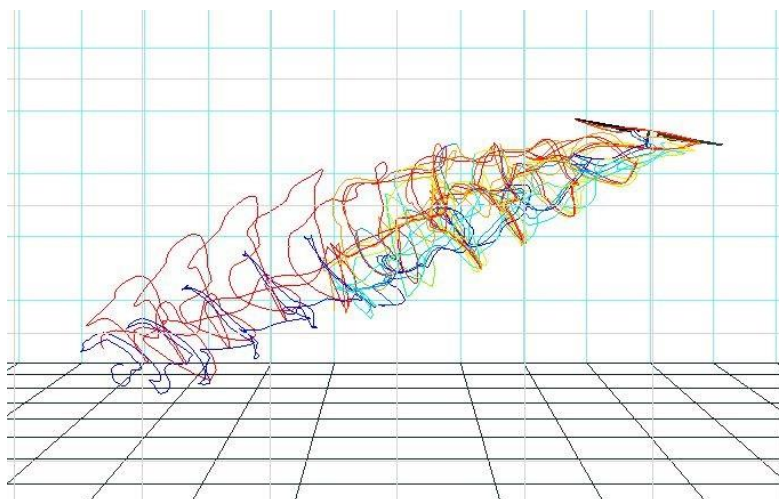


**Figure 6.6:** Single KDE rotor at forward flight 20 ft/s in wind tunnel - pitch -10 degrees - side view

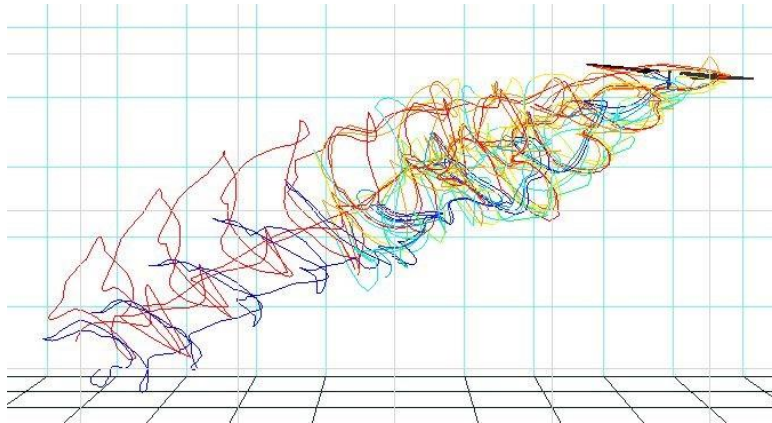


**Figure 6.7:** Single KDE rotor at forward flight 20 ft/s in wind tunnel, pitch angle of -5 Degrees, side view

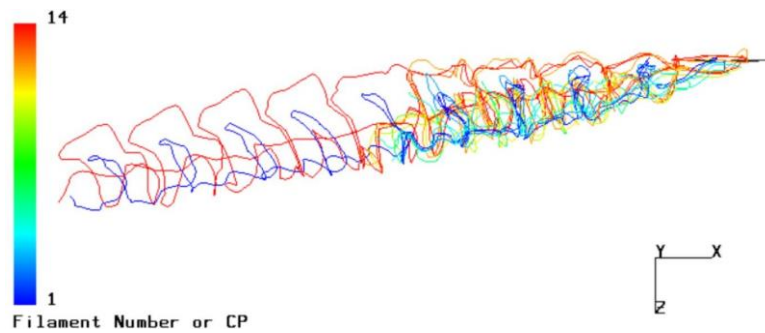


**Figure 6.8:** Single KDE rotor at forward flight 40 ft/s in wind tunnel, pitch angle of 0 degrees, side view

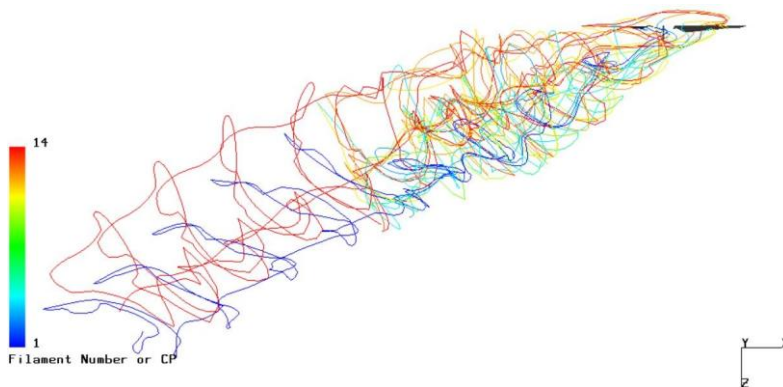


**Figure 6.9:** Single KDE rotor at forward flight 40 ft/s in free field, pitch angle of 0 degrees, side view



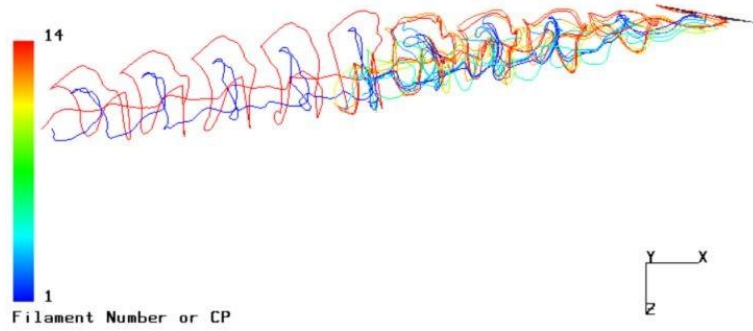


**Figure 6.10:** Single KDE rotor at forward flight 40 ft/s in free field - pitch -10 degrees - side view

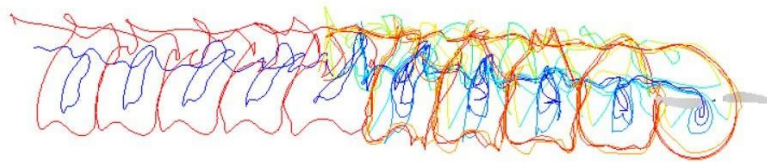


**Figure 6.11:** Single KDE rotor at forward flight 40 ft/s in wind tunnel - pitch 0 degrees - top view

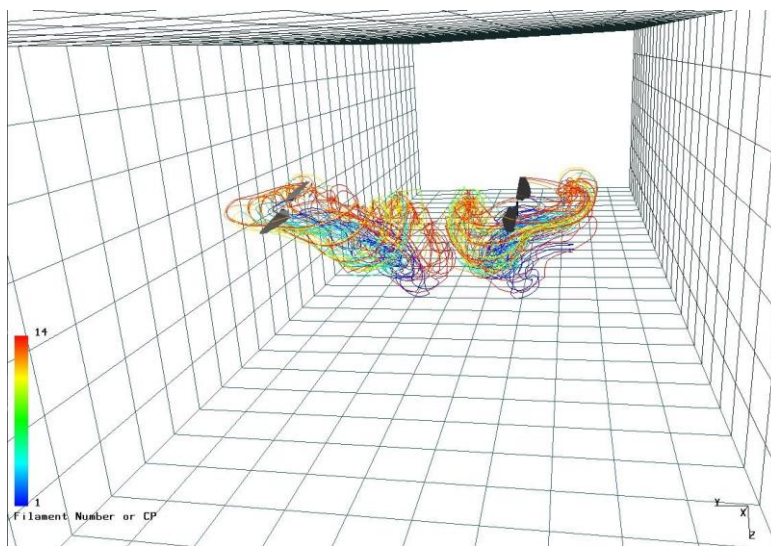


**Figure 6.12:** Two rotor cases at forward flight 20 ft/s in wind tunnel with pitch -10 degrees

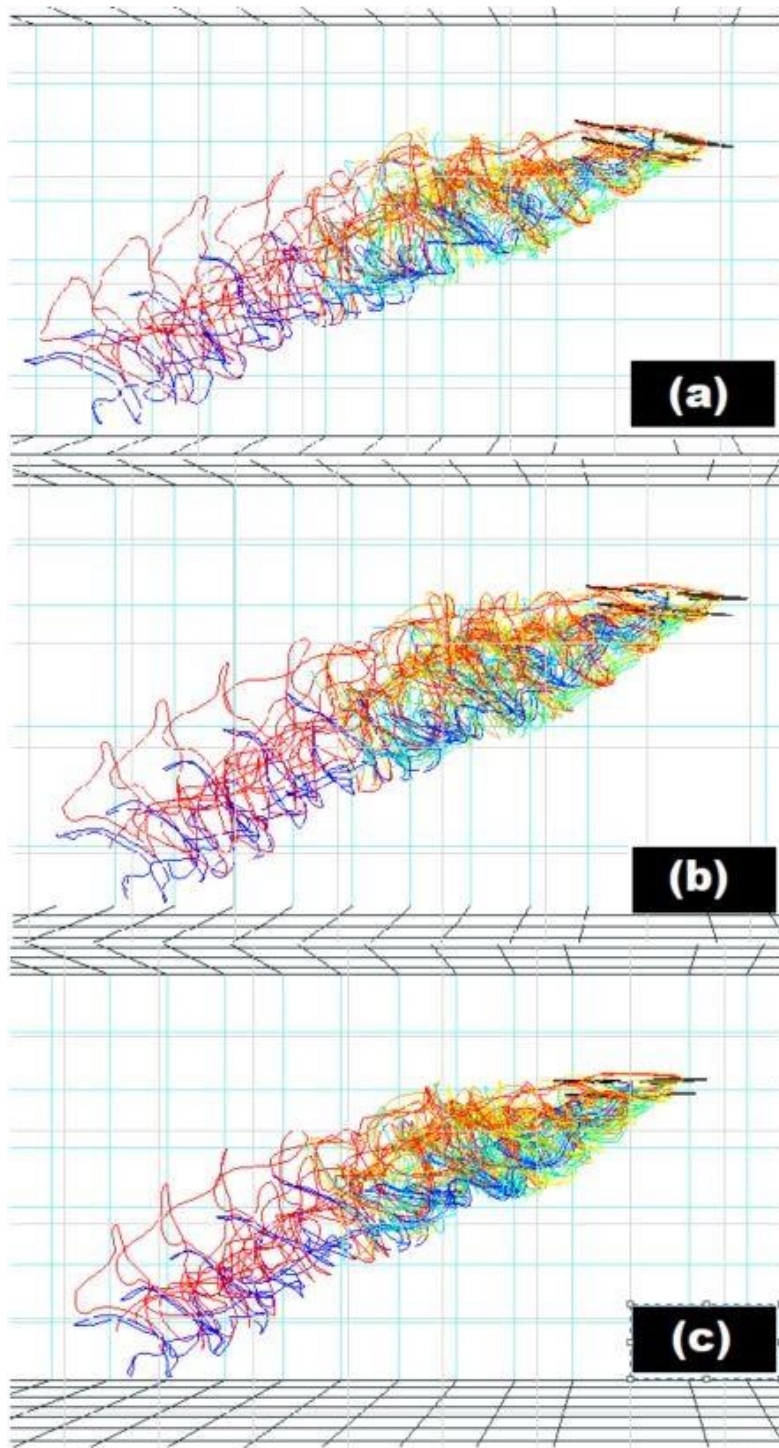


**Figure 6.13:** Two rotor cases at forward flight 20 ft/s in wind tunnel - side view - pitch angle (a) -10 degrees (b) -5 degrees (c) 0 degrees

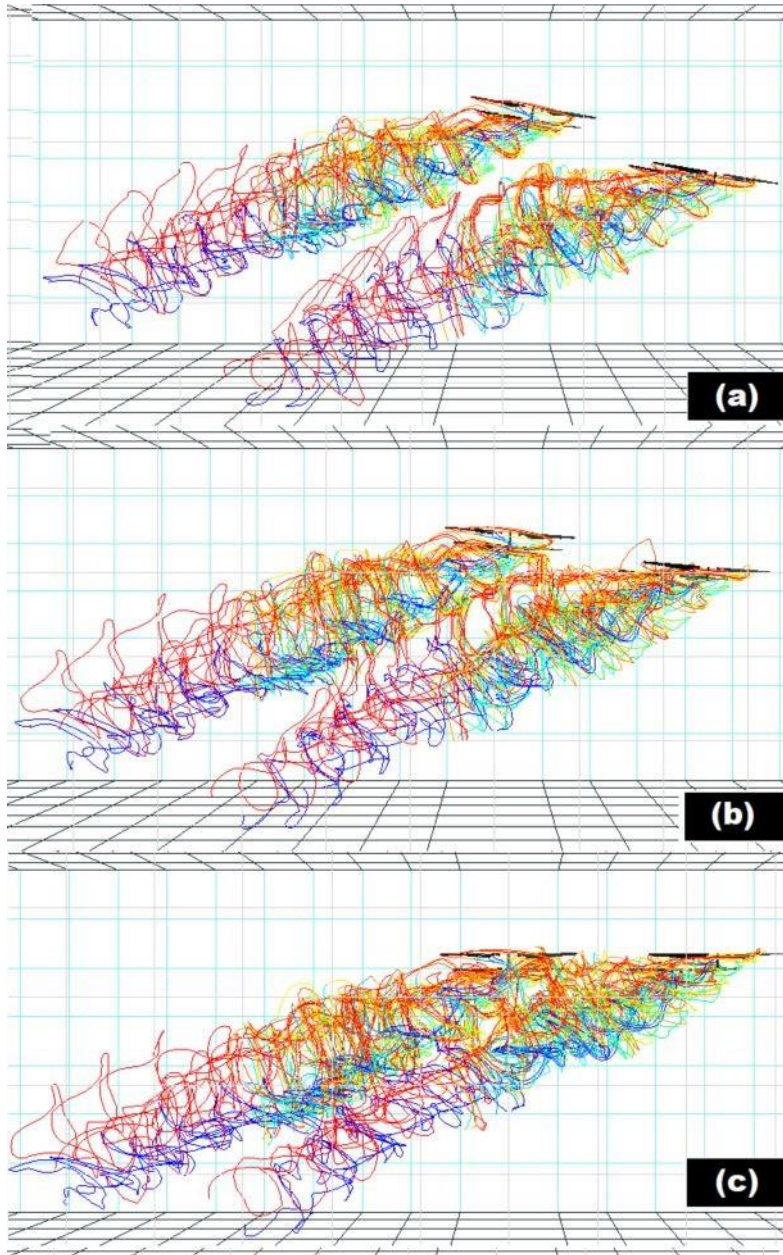


**Figure 6.14:** Four rotor cases at forward flight 20 ft/s in wind tunnel - side view - pitch angle (a) -10 degrees (b) -5 degrees (c) 0 degrees



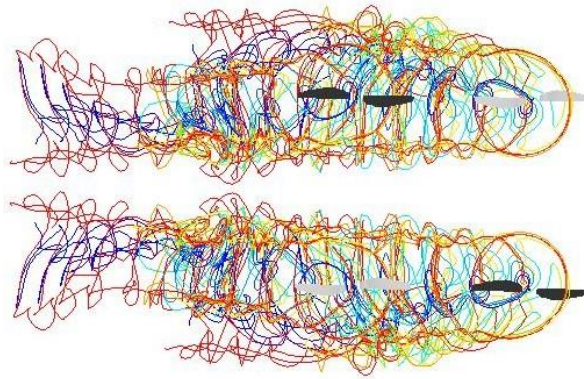


**Figure 6.15:** Four rotor cases at forward flight 20 ft/s in wind tunnel - top view - pitch angle 0 degrees

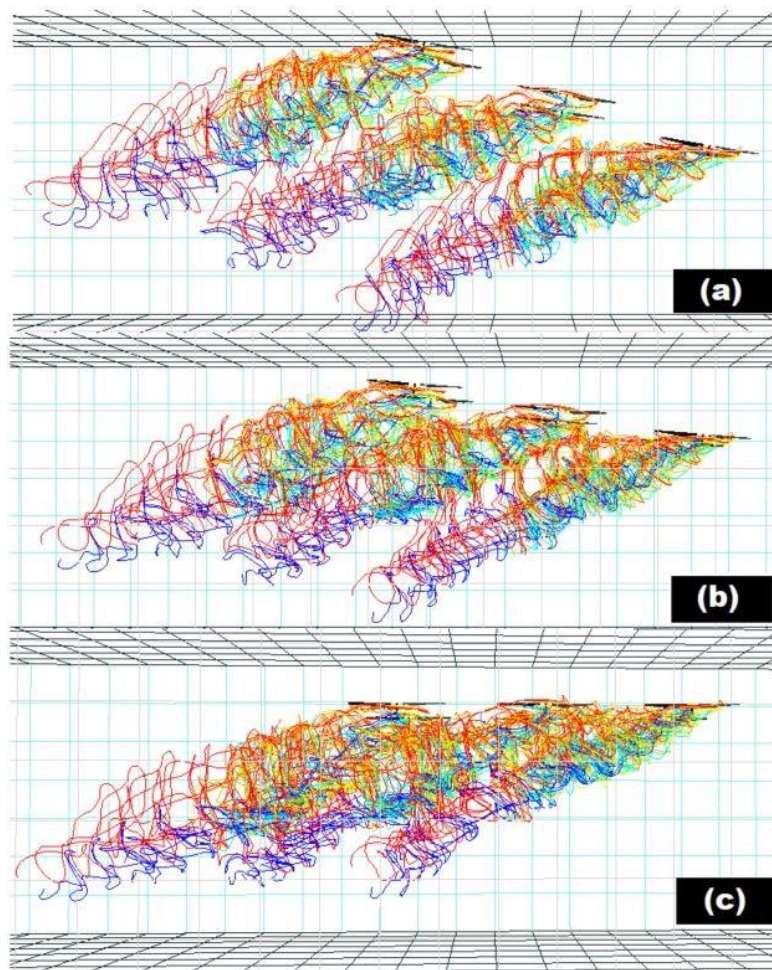


**Figure 6.16:** Six rotor cases in tall configuration at forward flight 20 ft/s in wind tunnel - side view - pitch angle (a) -10 degrees (b) -5 degrees (c) 0 degrees

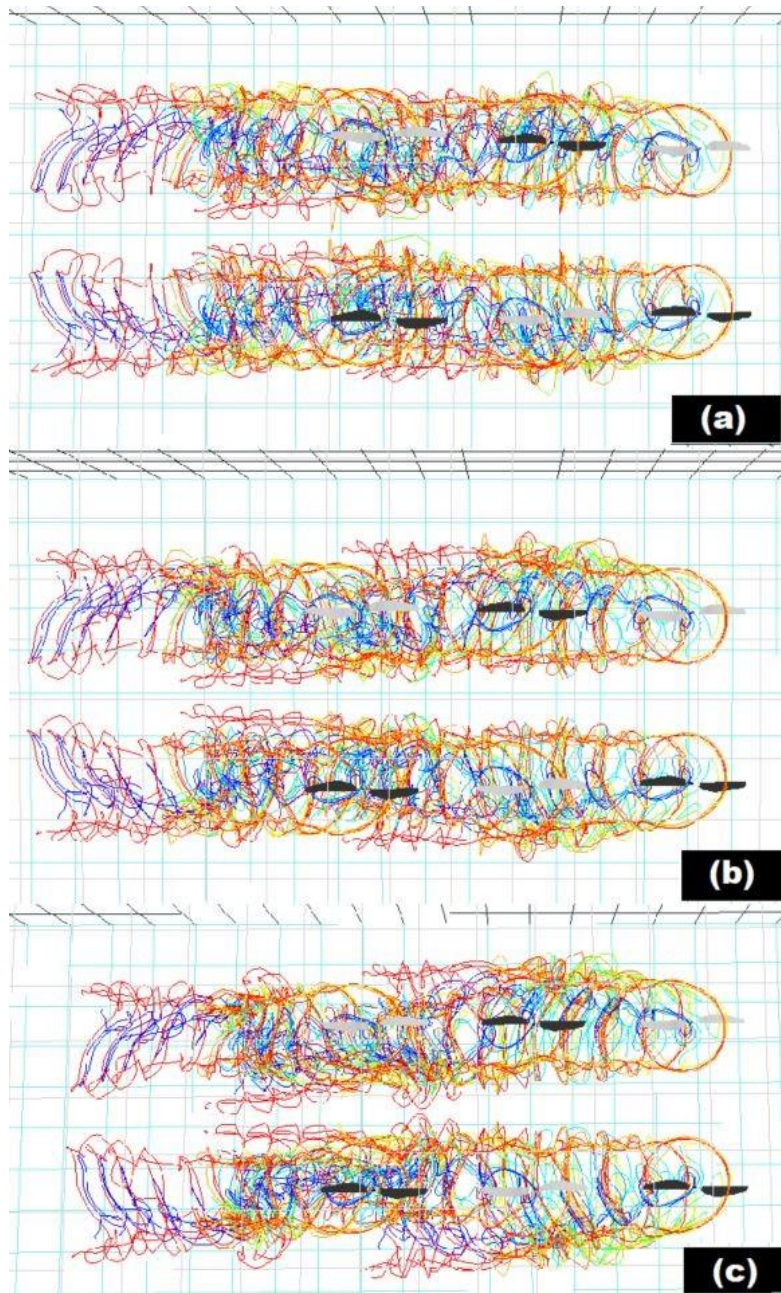


**Figure 6.17:** Six rotor cases in tall configuration at forward flight 20 ft/s in wind tunnel - top view - pitch angle (a) -10 degrees (b) -5 degrees (c) 0 degrees



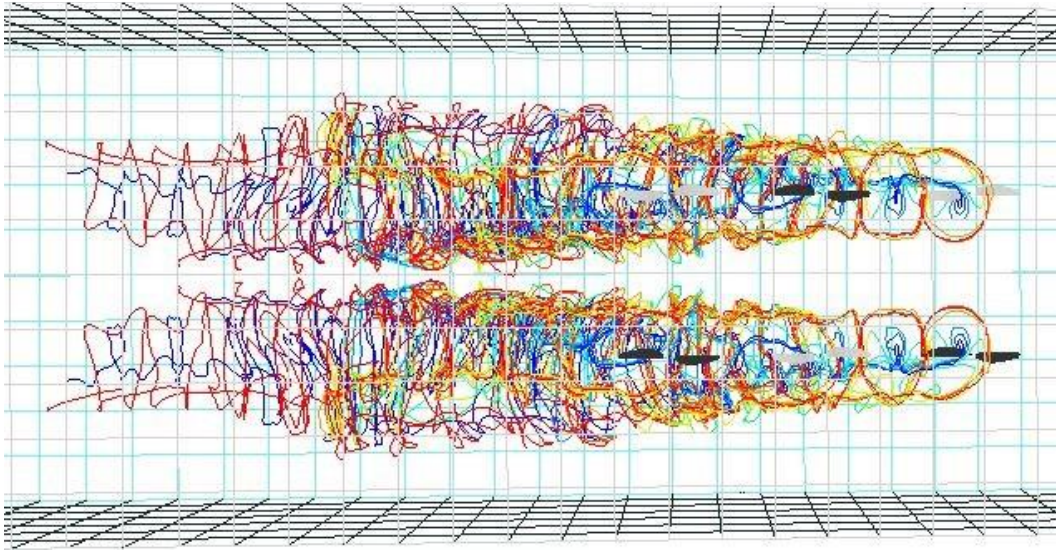


**Figure 6.18:** Six rotor cases in tall configuration at forward flight 40 ft/s in wind tunnel - top view - pitch angle 0 degrees

# Appendix C

Appendix C includes some CHARM input files had been used for this report.

## UH-60A Input Files

- The *run characteristics* input file for UH-60

```
UH60rc.inp: Run Characteristics Input File for UH60 hover
calculations using @submitlots
NROTOR
  1
PATHNAME
  ../
INPUT FILENAMES for UH60 main rotor
  UH60rw.inp
  UH60bg.inp
  UH60bd.inp
  UH60af.inp
  none
SSPD      RHO
1116.0    .002377
SFRAME
  0
ADV  ALPHAS
0.0  0.0
NPSI  NREV  CONVG1  CONVG2  CONVG3  MREV
  24    200    -1.0    -1.0    -1.0    0
IRST  IFREE  IGPR
  0     0     1
IOUT  NRS    (ROUT(I),I=1,NRS)
  4     8    0.3  0.4  0.5  0.6  0.7  0.8  0.9  0.95
NPRINT  IBLPLT  (IFILPLT(I),I=1,4)
  0     0     3  3  3  3
IDEBUG (Debug flag)
  0
ISCAN (Scan plane flag)
  0
ISTRSS (Stress calculation flag)
  0
IFV  IQUIK1
  2     1
IFVFLGS
  1  1  1  1  1
ISURF
  0
ISHIP
  0
IRECON  NOISE
  0     0
NLS
  0
```

## SUI Input Files

- The *run characteristics* input file for SUI

```
NROTOR
  1
PATHNAME
../
INPUT FILENAMES
Glrw.inp
Gbg.inp
Gbd.inp
SUIaf5.inp
none
SSPD      RHO
1125.0    .00238
INFLOW
  0
ADV      ALPHAS
  0      0
NPSI    NREV      CONVG1    CONVG2    CONVG3    MREV
  24    200      -1.0     -1.0     -1.0      0
IRST    IFREE    IGPR
  0     0      1
IVOUT   NRS      (ROUT(I), I=1, NRS)
  6
20     .1 .2 .25 .3 .35 .4 .45 .5 .55 .6 .65 .7 .75 .8 .85 .9 .92 .9
4     .96 .98
NPRINT  IBLPLT    (IFILPLT(I), I=1,4)
  0      0      3      3      3      3
IDEBUG
  0
ISCAN
  0
ISTRSS (Stress calculation flag)
  0
IFV     IQUIK1
  2     1
IFVFW   IFVBL   IFVSU   IFVSC   IFVLS
  1     1     1     1     1
ISURF
  0
ISHIP
  0
IRECON  NOISE
  0     0
NLS
  0
```



• The *rotor/wake* input file for SUI

```

NBLADE OMEGA
 2 469
IROTAT XROTOR X,Y,Z tilt ITILT
 1 0.0 0.0 0.0 0.0 0.0 0.0 0
ICOLL COLL CT
 1 0.000 .0092
ITRIM A1W B1W A1S B1S
 0 0.0 0.0 0.0 0.0
NOWAKE ICNVCT NWAKES NPWAKE IFAR MBCVE
 0 0 1 1 1 0
KSCHEME KPC
 0 0
NCUT AOV LAP ISKEW IUNS
 1 -1.000 1 0
NZONE (NVORT(I), I=1,NZONE)
 3 14 6 2
(NPTFW(I), I=1,NZONE)
 48 48 72
CORLIM Zone 1 Min core radii
0.01
CORLIM Zone 1 Max core radii
1.0
CORLIM Zone 2 Min core radii
0.01
CORLIM Zone 2 Max core radii
1.0
CORLIM Zone 3 Min core radii
0.1
CORLIM Zone 3 Max core radii
0.1
CUTLIM Zone 1 Min cutoff distance
0.01
CUTLIM Zone 1 Max cutoff distance
1.0
CUTLIM Zone 2 Min cutoff distance
0.01
CUTLIM Zone 2 Max cutoff distance
1.0
CUTLIM Zone 3 Min cutoff distance
0.1
CUTLIM Zone 3 Max cutoff distance
0.1
IDYNM
 1
SRAD SHGHT
0.0 0.0
NHHI (Higher harmonic cyclic pitch input flag)
 0

```

- The *blade geometry* input file for SUI

```

NSEG
 19
CUTOUT
 0.1292   -0.020   0.0000
SL (ISEG)
 19*0.026
CHORD (ISEG)
 0.098   0.112   0.120   0.124   0.125   0.124   0.122   0.118
0.115
 0.111   0.106   0.101   0.095   0.089   0.083   0.078   0.072
0.064
 0.056   0.037
ELOFSG (ISEG) - (elastic axis offset)
 20*0.000
SWEEP (ISEG)
 19*0.000
TWRD (Blade root twist at zero collective in degrees)
 21.770
TWSTGD (ISEG)
-0.05   -1.81   -1.77   -1.59   -1.27   -1.27   -1.01   -0.82   -0
.79
-0.63   -0.52   -0.39   -0.45   -0.33   -0.37   -0.24   -0.17   -0
.10
-0.02
ANHD (ISEG)
 19*0.0
THCKND (ISEG)
 0.1177   0.0976   0.0873   0.0818   0.0788   0.0772   0.0753
0.0738   0.0722
 0.0711   0.0704   0.0707   0.0713   0.0726   0.0754   0.0789
0.0830   0.0874
 0.0888
KFLAP (ISEG)
 19*0.0
FLAPND (ISEG)
 19*0.0
FLHNGE (ISEG)
 19*0.0
FLDEFL (ISEG)
 19*0.0
NCAM
 0
NCHORD  NSPAN  ICOS
 1      -80    -1

```

- The *blade dynamics* input file for SUI

```

ISTRM
0
ISTRIP  IFPC  IAERO
-1      0     1
ICOMP   IRVFLO ISTFLO
1       0     1
IART    HINGE  PRECONE
0       0.0   0.0
NMODE
1
NMDFLP  NMDTOR  NMDLAG  NMDELG
1       0     0     0
IFXMDE
0
FREQMD  GMASS      for Mode 1
1.039   0.2308
NRBARS
50
RBARS (IR), IR=1,NRBARS
0.000   0.020   0.041   0.061   0.082   0.102   0.122   0.143
0.163   0.184   0.204   0.224   0.245   0.265   0.286   0.306
0.327   0.347   0.367   0.388
0.408   0.429   0.449   0.469   0.490   0.510   0.531   0.551
0.571   0.592   0.612   0.633   0.653   0.673   0.694   0.714
0.735   0.755   0.776   0.796
0.816   0.837   0.857   0.878   0.898   0.918   0.939   0.959
0.980   1.000
Rigid flap mode
0.000   0.000   0.000   0.000   0.000   0.000   0.000   0.000
0.000   0.000   0.000   0.000   0.000   0.000   0.000   0.000
0.000   0.000   0.000   0.000
0.000   0.000   0.000   0.000   0.000   0.000   0.000   0.000
0.000   0.000   0.000   0.000   0.000   0.000   0.000   0.000
0.000   0.000   0.000   0.000
0.000   0.000   0.000   0.000   0.000   0.000   0.000   0.000
0.000   0.000
0.000   0.000   0.000   0.000   0.000   0.000   0.000   0.000
0.000   0.000   0.000   0.000   0.000   0.000   0.000   0.000
0.000   0.000   0.000   0.000
0.000   0.000   0.000   0.000   0.000   0.000   0.000   0.000
0.000   0.000   0.000   0.000
0.000   0.000   0.000   0.000   0.000   0.000   0.000   0.000
0.000   0.000   0.000   0.000   0.044   0.125   0.205   0.286   0.367
0.447   0.528   0.608   0.689   0.769   0.850   0.930   1.011
1.092   1.172   1.253   1.333
1.414   1.494   1.575   1.655   1.736   1.817   1.897   1.978
2.058   2.139   2.219   2.300   2.381   2.461   2.542   2.622
2.703   2.783   2.864   2.944
3.025   3.106   3.186   3.267   3.347   3.428   3.508   3.589
3.669   3.750
0.000   0.000   0.000   0.000   0.000   0.000   0.000   0.000
0.000   0.000   0.000   0.000   0.000   0.000   0.000   0.000
0.000   0.000   0.000   0.000
0.000   0.000   0.000   0.000   0.000   0.000   0.000   0.000
0.000   0.000   0.000   0.000   0.000   0.000   0.000   0.000
0.000   0.000   0.000   0.000
0.000   0.000   0.000   0.000   0.000   0.000   0.000   0.000

```

## MTB Input Files - 1 Rotor - Free Field(MTB-1R-FF)

The *2D airfoil section data*, *blade geometry*, and *blade dynamics* input files for the MTB simulation stayed the same for all the cases. Therefore, only the *rotor/wake* and the *run characteristics* input files will be inputted for two, four, and six rotor cases.

- **The *run characteristics* input file for (MTB-1R-FF)**

Single rotor case at -10 degrees pitch angle with forward speed of 20 ft/s in free field.

```
mtb2.inp: MTB test baseline CHARM input file - with 7 x 10 wind
tunnel
NROTOR
  1
PATHNAME
  ../
INPUT FILENAMES for Prop 2 - left front
  leftfrw.inp
  Mlbg.inp
  Mbd.inp
  MTBaf8.inp
  none
SSPD      RHO
1133.0    .002314
SFRAME
  1
  U      V      W      P      Q      R - Tunnel speed is 20 feet/sec
20.0    0.0    0.0      0.0    0.0    0.0
NPSI    NREV    CONVG1    CONVG2    CONVG3    MREV
  24     10     -1.0      -1.0     -1.0      0
IRST    IFREE    IGPR
  0      0      0
IVOUT    NRS      (ROUT(I),I=1,NRS)
  4      8        0.5 0.6 0.7 0.8 0.85 0.9 0.95 0.99
NPRINT    IBLPLT    (IFILPLT(I),I=1,4)
  0      0          3 3 3 3
IDEBUG (Debug flag)
  0
ISCAN (Scan plane flag)
  0
ISTRSS (Stress calculation flag)
  0
IFV      IQUIK1
  2      1
IFVFW    IFVBL    IFVSU    IFVSC    IFVLS
  1      1      1      1      1
ISURF
  0
ISHIP
  0
IRECON    NOISE
  0      0
NLS
  0
```

- The *rotor/wake* input file for (MTB-1R-FF)

Single rotor case at -10 degrees pitch angle with forward speed of 20 ft/s in free field.

```

NBLADE OMEGA
 2      209.
IROTAT          XROTOR          X,Y,Z tilt  ITILT
-1      3.290 -1.58 -0.141      0.0 -10.0 0.0      1
ICOLL  COLL      CT      for rotor 1
 0      0.0      .013
ITRIM   A1S      B1S      als      bls
 0      0.0      0.0      0.0      0.0
NOWAKE  ICNVCT   NWAKES   NPWAKE   IFAR   MBCVE
 0      0        1        0        0      0
KSCHEME KPC
 0      0
NCUT   AOV LAP   ISKEW   IUNS
 1      -1      1        1
NZONE  (NVORT(I), I=1,NZONE)
 3      14 14 2
ICORE  AKINEM  A1  PCOREM  CRMON
 1      0.0 0.01 0.0      0.0
(NPTFW(I), I=1,NZONE)
120 120 120
(CORLIM(NV, IZONE, 1), NV=1, NVORT(IZONE) IZONE=1 (Min core radii)
0.01
(CORLIM(NV, IZONE, 2), NV=1, NVORT(IZONE) IZONE=1 (Max core radii)
1.0
(CORLIM(NV, IZONE, 1), NV=1, NVORT(IZONE) IZONE=2 (Min core radii)
0.01
(CORLIM(NV, IZONE, 2), NV=1, NVORT(IZONE) IZONE=2 (Max core radii)
1.0
(CORLIM(NV, IZONE, 1), NV=1, NVORT(IZONE) IZONE=3 (Min core radii)
0.1
(CORLIM(NV, IZONE, 2), NV=1, NVORT(IZONE) IZONE=3 (Max core radii)
0.1
(CUTLIM(NV, IZONE, 1), NV=1, NVORT(IZONE) IZONE=1 (Min cutoff
distances)
0.01
(CUTLIM(NV, IZONE, 2), NV=1, NVORT(IZONE) IZONE=1 (Max cutoff
distances)
1.0
(CUTLIM(NV, IZONE, 1), NV=1, NVORT(IZONE) IZONE=2 (Min cutoff
distances)
0.01
(CUTLIM(NV, IZONE, 2), NV=1, NVORT(IZONE) IZONE=2 (Max cutoff
distances)
1.0
(CUTLIM(NV, IZONE, 1), NV=1, NVORT(IZONE) IZONE=3 (Min cutoff
distances)
0.1
(CUTLIM(NV, IZONE, 2), NV=1, NVORT(IZONE) IZONE=3 (Max cutoff
distances)
0.1
IDYNM
 1
SRAD  SHGHT
0.0   0.0
NHHI (Higher harmonic cyclic pitch input flag)
 0

```

## MTB Input Files - 1 Rotor - Wind Tunnel (MTB-1R-WT)

- The *run characteristics* input file for (MTB-1R-WT)

Single rotor case at -10 degrees pitch angle with forward speed of 20 ft/s in the wind tunnel.

```
mtb2.inp: MTB test baseline CHARM input file - with 7 x 10 wind
tunnel
NROTOR
  1
PATHNAME
  ../
INPUT FILENAMES for Prop 2 - left front
  leftfrw.inp
  Mlbg.inp
  Mbd.inp
  MTBaf8.inp
  none
SSPD      RHO
1133.0    .002314
SFRAME
  1
  U      V      W      P      Q      R - Tunnel speed is 20 feet/sec
20.0     0.0     0.0     0.0     0.0     0.0
NPSI     NREV     CONVG1  CONVG2  CONVG3  MREV
  24      10      -1.0     -1.0     -1.0     0
IRST     IFREE    IGPR
  0       0       0
IVOUT    NRS      (ROUT(I), I=1, NRS)
  4       8       0.5 0.6 0.7 0.8 0.85 0.9 0.95 0.99
NPRINT   IBLPLT   (IFILPLT(I), I=1,4)
  0       0       3 3 3 3
IDEBUG   (Debug flag)
  0
ISCAN    (Scan plane flag)
  0
ISTRSS   (Stress calculation flag)
  0
IFV      IQUIK1
  2       1
IFVFW    IFVBL    IFVSU    IFVSC    IFVLS
  1       1       1       1       1
ISURF
  1
NSURFS
  1
KTYPE
  0
XMIN     XMAX     YMIN     YMAX     ZMIN     ZMAX
-25.0    25.0    -5.0     5.0     -3.5     3.5
NX       NY       NZ       SPACE
-50     10       7       0
NPSET    KLIFT
  0       0
ISHIP
  0
IRECON   NOISE
  0       0
NLS
  0
```



- The *rotor/wake* input file for (MTB-1R-WT)

Single rotor case at -10 degrees pitch angle with forward speed of 20 ft/s in the wind tunnel.

```

NBLADE OMEGA
 2      209.
IROTAT          XROTOR          X,Y,Z tilt  ITILT
-1      3.290 -1.58 -0.141      0.0 -10.0 0.0      1
ICOLL  COLL      CT      for rotor 1
 0      0.0      .013
ITRIM   A1S      B1S      als      bls
 0      0.0      0.0      0.0      0.0
NOWAKE  ICNVCT   NWAKES   NPWAKE   IFAR   MBCVE
 0      0        1        0        0      0
KSCHEME KPC
 0      0
NCUT   AOV LAP   ISKEW   IUNS
 1      -1      1        1
NZONE  (NVORT(I), I=1,NZONE)
 3      14 14 2
ICORE  AKINEM  A1  PCOREM  CRMON
 1      0.0  0.01  0.0      0.0
(NPTFW(I), I=1,NZONE)
120 120 120
(CORLIM(NV, IZONE, 1), NV=1, NVORT(IZONE) IZONE=1 (Min core radii)
0.01
(CORLIM(NV, IZONE, 2), NV=1, NVORT(IZONE) IZONE=1 (Max core radii)
1.0
(CORLIM(NV, IZONE, 1), NV=1, NVORT(IZONE) IZONE=2 (Min core radii)
0.01
(CORLIM(NV, IZONE, 2), NV=1, NVORT(IZONE) IZONE=2 (Max core radii)
1.0
(CORLIM(NV, IZONE, 1), NV=1, NVORT(IZONE) IZONE=3 (Min core radii)
0.1
(CORLIM(NV, IZONE, 2), NV=1, NVORT(IZONE) IZONE=3 (Max core radii)
0.1
(CUTLIM(NV, IZONE, 1), NV=1, NVORT(IZONE) IZONE=1 (Min cutoff
distances)
0.01
(CUTLIM(NV, IZONE, 2), NV=1, NVORT(IZONE) IZONE=1 (Max cutoff
distances)
1.0
(CUTLIM(NV, IZONE, 1), NV=1, NVORT(IZONE) IZONE=2 (Min cutoff
distances)
0.01
(CUTLIM(NV, IZONE, 2), NV=1, NVORT(IZONE) IZONE=2 (Max cutoff
distances)
1.0
(CUTLIM(NV, IZONE, 1), NV=1, NVORT(IZONE) IZONE=3 (Min cutoff
distances)
0.1
(CUTLIM(NV, IZONE, 2), NV=1, NVORT(IZONE) IZONE=3 (Max cutoff
distances)
0.1
IDYNM
 1
SRAD  SHGHT
0.0   0.0
NHHI (Higher harmonic cyclic pitch input flag)
 0

```

## MTB Input Files - 1 Rotor - Isolated at hover (MTB-1R-HOVER)

- The *run characteristics* input file for (MTB-1R-HOVER)

Isolated KDE rotor at hover.

```
MTB test baseline CHARM input file - hover
NROTOR
  1
PATHNAME
  ./
INPUT FILENAMES for Prop 2 - left front
  leftfrw.inp
  Mlbg.inp
  Mbd.inp
  MTBaf8.inp
  none
SSPD      RHO
1125.0    .00238
INFLOW
  0
ADV      ALPHAS
  0      0
NPSI     NREV      CONVG1      CONVG2      CONVG3      MREV
  24     200      -1.0      -1.0      -1.0      0
IRST     IFREE     IGPR
  0      0      1
IVOUT    NRS      (ROUT(I),I=1,NRS)
  6
20      .1 .2 .25 .3 .35 .4 .45 .5 .55 .6 .65 .7 .75 .8 .85 .9 .92 .9
4 .96 .98
NPRINT   IBLPLT   (IFILPLT(I),I=1,4)
  0      0      3      3      3      3
IDEBUG
  0
ISCAN
  0
ISTRSS (Stress calculation flag)
  0
IFV      IQUIK1
  2      1
IFVFW    IFVBL    IFVSU    IFVSC    IFVLS
  1      1      1      1      1
ISURF
  0
ISHIP
  0
IRECON   NOISE
  0      0
NLS
  0
```



• The *rotor/wake* input file for (MTB-1R-HOVER)

Isolated KDE rotor at hover.

```

NBLADE OMEGA
 2      314.2
IROTAT      XROTOR      X,Y,Z tilt  ITILT
-1      2.99 -1.58 -1.254  0.0 0.0 0.0  0
ICOLL  COLL  CT  for rotor 1
 1      0.0  .013
ITRIM  A1S  B1S  a1s  b1s
 0      0.0  0.0  0.0  0.0
NOWAKE  ICNVCT  NWAKES  NPWAKE  IFAR  MBCVE
 0      0      1      1      1      0
KSCHEME  KPC
 0      0
NCUT  AOV LAP  ISKEW  IUNS
 1      -1      1      0
NZONE  (NVORT(I), I=1,NZONE)
 3      14  14  2
ICORE  AKINEM  A1  PCOREM  CRMON
 1      0.0  0.01  0.0  0.0
(NPTFW(I), I=1,NZONE)
120 120 120
(CORLIM(NV, IZONE, 1), NV=1, NVORT(IZONE) IZONE=1 (Min core radii)
0.01
(CORLIM(NV, IZONE, 2), NV=1, NVORT(IZONE) IZONE=1 (Max core radii)
1.0
(CORLIM(NV, IZONE, 1), NV=1, NVORT(IZONE) IZONE=2 (Min core radii)
0.01
(CORLIM(NV, IZONE, 2), NV=1, NVORT(IZONE) IZONE=2 (Max core radii)
1.0
(CORLIM(NV, IZONE, 1), NV=1, NVORT(IZONE) IZONE=3 (Min core radii)
0.1
(CORLIM(NV, IZONE, 2), NV=1, NVORT(IZONE) IZONE=3 (Max core radii)
0.1
(CUTLIM(NV, IZONE, 1), NV=1, NVORT(IZONE) IZONE=1 (Min cutoff
distances)
0.01
(CUTLIM(NV, IZONE, 2), NV=1, NVORT(IZONE) IZONE=1 (Max cutoff
distances)
1.0
(CUTLIM(NV, IZONE, 1), NV=1, NVORT(IZONE) IZONE=2 (Min cutoff
distances)
0.01
(CUTLIM(NV, IZONE, 2), NV=1, NVORT(IZONE) IZONE=2 (Max cutoff
distances)
1.0
(CUTLIM(NV, IZONE, 1), NV=1, NVORT(IZONE) IZONE=3 (Min cutoff
distances)
0.1
(CUTLIM(NV, IZONE, 2), NV=1, NVORT(IZONE) IZONE=3 (Max cutoff
distances)
0.1
IDYNM
 1
SRAD  SHGHT
0.0  0.0
NHHI (Higher harmonic cyclic pitch input flag)
 0

```

## MTB Input Files - 2 Rotors - Free Field (MTB-2R-FF)

- The *run characteristics* input file for (MTB-2R-FF)

Two rotors case at -10 degrees pitch angle with forward speed of 20 ft/s in free field.

```
NROTOR
2
PATHNAME
../
INPUT FILENAMES for Prop 2 - right middle
rightmrw.inp
M1bg.inp
Mbd.inp
MTBaf8.inp
none
INPUT FILENAMES for Prop 5 - left middle
leftmrw.inp
M1bg.inp
Mbd.inp
MTBaf8.inp
none
SSPD      RHO
1109.0    .002411
SFRAME
1
U      V      W      P      Q      R - Tunnel speed is 20 feet/sec
20.0   0.0   0.0   0.0   0.0   0.0
NPSI   NREV   CONVG1  CONVG2  CONVG3  MREV
24     10    -1.0    -1.0    -1.0    0
IRST   IFREE  IGPR
0      0      0
IVOUT  NRS    (ROUT(I),I=1,NRS)
4      8     0.5 0.6 0.7 0.8 0.85 0.9 0.95 0.99
NPRINT IBLPLT (IFILPLT(I),I=1,4)
0      0     3 3 3 3
IDEBUG (Debug flag)
0
ISCAN (Scan plane flag)
0
ISTRSS (Stress calculation flag)
0
IFV    IQUIK1
2      1
IFVFW  IFVBL  IFVSU  IFVSC  IFVLS
1      1    1    1    1
ISURF
0
ISHIP
0
IRECON NOISE
0      0
NLS
0
```

- The *rotor/wake* input file for (MTB-2R-FF)

Two rotors case at -10 degrees pitch angle with forward speed of 20 ft/s in free field. The *rotor/wake* input file for the middle rotor #3:

```

NBLADE OMEGA
 2      209.
IROTAT          XROTOR          X,Y,Z tilt  ITILT
-1      0.471  1.64  -1.16      0.0 -10.0 0.0    1
ICOLL  COLL    CT      for rotor 1
 0      0.0    .013
ITRIM   A1S    B1S    als    bls
 0      0.0    0.0    0.0    0.0
NOWAKE  ICNVCT  NWAKES  NPWAKE  IFAR  MBCVE
 0      0      1      0      0      0
KSCHEME KPC
 0      0
NCUT  AOV LAP  ISKEW  IUNS
 1      -1      1      1
NZONE  (NVORT(I), I=1,NZONE)
 3      14  14  2
ICORE  AKINEM  A1  PCOREM  CRMON
 1      0.0    0.01  0.0    0.0
(NPTFW(I), I=1,NZONE)
120 120 120
(CORLIM(NV, IZONE, 1), NV=1, NVORT(IZONE) IZONE=1 (Min core radii)
0.01
(CORLIM(NV, IZONE, 2), NV=1, NVORT(IZONE) IZONE=1 (Max core radii)
1.0
(CORLIM(NV, IZONE, 1), NV=1, NVORT(IZONE) IZONE=2 (Min core radii)
0.01
(CORLIM(NV, IZONE, 2), NV=1, NVORT(IZONE) IZONE=2 (Max core radii)
1.0
(CORLIM(NV, IZONE, 1), NV=1, NVORT(IZONE) IZONE=3 (Min core radii)
0.1
(CORLIM(NV, IZONE, 2), NV=1, NVORT(IZONE) IZONE=3 (Max core radii)
0.1
(CUTLIM(NV, IZONE, 1), NV=1, NVORT(IZONE) IZONE=1 (Min cutoff
distances)
0.01
(CUTLIM(NV, IZONE, 2), NV=1, NVORT(IZONE) IZONE=1 (Max cutoff
distances)
1.0
(CUTLIM(NV, IZONE, 1), NV=1, NVORT(IZONE) IZONE=2 (Min cutoff
distances)
0.01
(CUTLIM(NV, IZONE, 2), NV=1, NVORT(IZONE) IZONE=2 (Max cutoff
distances)
1.0
(CUTLIM(NV, IZONE, 1), NV=1, NVORT(IZONE) IZONE=3 (Min cutoff
distances)
0.1
(CUTLIM(NV, IZONE, 2), NV=1, NVORT(IZONE) IZONE=3 (Max cutoff
distances)
0.1
IDYNM
 1
SRAD  SHGHT
0.0  0.0
NHHI (Higher harmonic cyclic pitch input flag)
 0

```

The *rotor/wake* input file for the middle rotor #4:

```

NBLADE OMEGA
 2      209.
IROTAT          XROTOR          X,Y,Z tilt  ITILT
 1      0.471 -1.58 -1.16      0.0 -10.0 0.0    1
ICOLL  COLL      CT      for rotor 1
 0      0.0      .013
ITRIM   A1S      B1S      a1s    b1s
 0      0.0      0.0      0.0    0.0
NOWAKE  ICNVCT   NWAKES   NPWAKE  IFAR   MBCVE
 0      0        1        0       0     0
KSCHEME KPC
 0      0
NCUT    AOV LAP   ISKEW   IUNS
 1      -1      1       1
NZONE   (NVORT(I), I=1,NZONE)
 3      14 14 2
ICORE   AKINEM   A1      PCOREM   CRMON
 1      0.0     0.01    0.0     0.0
(NPTFW(I), I=1,NZONE)
120 120 120
(CORLIM(NV, IZONE, 1), NV=1, NVORT(IZONE) IZONE=1 (Min core radii)
0.01
(CORLIM(NV, IZONE, 2), NV=1, NVORT(IZONE) IZONE=1 (Max core radii)
1.0
(CORLIM(NV, IZONE, 1), NV=1, NVORT(IZONE) IZONE=2 (Min core radii)
0.01
(CORLIM(NV, IZONE, 2), NV=1, NVORT(IZONE) IZONE=2 (Max core radii)
1.0
(CORLIM(NV, IZONE, 1), NV=1, NVORT(IZONE) IZONE=3 (Min core radii)
0.1
(CORLIM(NV, IZONE, 2), NV=1, NVORT(IZONE) IZONE=3 (Max core radii)
0.1
(CUTLIM(NV, IZONE, 1), NV=1, NVORT(IZONE) IZONE=1 (Min cutoff
distances)
0.01
(CUTLIM(NV, IZONE, 2), NV=1, NVORT(IZONE) IZONE=1 (Max cutoff
distances)
1.0
(CUTLIM(NV, IZONE, 1), NV=1, NVORT(IZONE) IZONE=2 (Min cutoff
distances)
0.01
(CUTLIM(NV, IZONE, 2), NV=1, NVORT(IZONE) IZONE=2 (Max cutoff
distances)
1.0
(CUTLIM(NV, IZONE, 1), NV=1, NVORT(IZONE) IZONE=3 (Min cutoff
distances)
0.1
(CUTLIM(NV, IZONE, 2), NV=1, NVORT(IZONE) IZONE=3 (Max cutoff
distances)
0.1
IDYNM
 1
SRAD   SHGHT
 0.0   0.0
NHHI (Higher harmonic cyclic pitch input flag)
 0

```

## MTB Input Files - 2 Rotors - Wind Tunnel (MTB-2R-WT)

- The *run characteristics* input file for (MTB-2R-WT)

Two rotors case at the -10 degrees pitch angle with forward speed of 20 ft/s in the wind tunnel.

```
NROTOR
 2
PATHNAME
../
INPUT FILENAMES for Prop 2 - right middle
rightmrw.inp
Mlbg.inp
Mbd.inp
MTBaf8.inp
none
INPUT FILENAMES for Prop 5 - left middle
leftmrw.inp
Mlbg.inp
Mbd.inp
MTBaf8.inp
none
SSPD      RHO
1109.0    .002411
SFRAME
 1
  U      V      W      P      Q      R - Tunnel speed is 20 feet/sec
20.0    0.0    0.0      0.0    0.0    0.0
NPSI    NREV    CONVG1  CONVG2  CONVG3  MREV
 24     10     -1.0     -1.0    -1.0    0
IRST    IFREE    IGPR
 0      0      0
IVOUT   NRS      (ROUT(I),I=1,NRS)
 4      8      0.5 0.6 0.7 0.8 0.85 0.9 0.95 0.99
NPRINT  IBLPLT   (IFILPLT(I),I=1,4)
 0      0      3 3 3 3
IDEBUG (Debug flag)
 0
ISCAN (Scan plane flag)
 0
ISTRSS (Stress calculation flag)
 0
IFV     IQUIK1
 2      1
IFVFW  IFVBL  IFVSU  IFVSC  IFVLS
 1      1      1      1      1
ISURE
 1
NSURFS
 1
KTYPE
 0
XMIN   XMAX   YMIN   YMAX   ZMIN   ZMAX
-25.0  25.0  -5.0   5.0    -3.5   3.5
NX     NY     NZ     SPACE
-50   10    7     0
NPSET  KLIFT
 0      0
ISHIP
 0
IRECON NOISE
 0      0
NLS
 0
```

- The *rotor/wake* input file for (MTB-2R-WT)

Same as the *rotor/wake* input files in the free field for two rotors case.

## **MTB Input Files - 4 and 6 Rotors**

The *rotor/wake* input files for six and four-rotor cases were set up similarly to two rotor cases. Please note that the location of each rotor needs to be adjusted individually. The information about the location of the rotors can be found in the Appendix B.

The information in tables below came directly from CHARM User's Manual.  
Parameters from the *run characteristics* input file:

Parameter	Description
NROTOR	Number of rotors
IMKS	IMKS=0 English units, IMKS=1 MKS units
SSPD	Speed of sound
RHO	Air density
SFRAME	SFRAME=0 performed in the shaft reference frame SFRAME=1 performed in the aircraft reference frame
ADV	Advance ratio
ALPHAS	Shaft angle of attack relative to the inflow velocity
NPSI	Number of azimuth locations per blade revolution
NREV	Maximum number of blade revolutions in the trim solution.
MREV	number of time-marching revolutions
IFREE	IFREE=0: A simple inflow model is used for the initial wake-induced velocity on the blade
IRST	IRST=0 Initialize the wake geometry using convection IRST=1 Initialize the wake geometry from a Wake Geometry Output File
IGPR	IGPR=0 Standard calculation procedure, IGPR=1 Relaxation solution
IVOUT	The Output Variable vs Azimuth File IVOUT=0 No output IVOUT=1 wake-induced velocity in the direction of rotor thrust IVOUT=2 Vertical blade displacement IVOUT=3 Circulation) IVOUT=4 Airload
NRS	Number of radial locations at which the IVOUT variable is returned
ROUT	radial locations where receive information about the IVOUT
NPRINT	Wake geometry output is printed to the Run Results Print File NPRINT=0 to eliminate excessive wake printout
IBLPLT	IBLPLT=0 Normal operation mode. No effect

Parameters from the *run characteristics* input file:

Parameter	Description
IDEBUG	IDEBUG=1 the print file may contain debug printout
ISCAN	determine the velocity and pressure at a grid of points in space
ISTRSS	ISTRSS = 0 No stress calculation ISTRSS = 1 Output shear stresses
IFV	IFV = 0 Fast Vortex Method (FVM) not implemented IFV=1 Hierarchical HFV method with user settings (MXHLEV,FMDG,NCPU) IFV=2 Hierarchical HFV method with default settings
IQUIK1	IQUIK1=0 Re-evaluate vortex lattice method influence coefficients during the first blade revolution of each blade dynamics calculation IQUIK1=1 Evaluate VLM influence coeff once for each blade dynamics
IFVFW	IFVFW=1 Use the HFV method for wake-on-wake calculations IFVFW=0 Do not use HFV for wake-on-wake calculations
IFVBL	IFVBL=1 Use HFV for wake-on-blade calculations IFVBL=0 Do not use HFV for wake-on-blade calculations
IFVSU	IFVSU=1 Use HFV for wake-on-surface calculations IFVSU=0 Do not use HFV for wake-on-surface calculations IFVSU=1 if only interested in surface influence on wake IFVSU=2 or 3 if interested in CP values on the surface
IFVSC	IFVSC=1 Use HFV for wake-on-scan grid calculations IFVSC=0 Do not use HFV for wake-on-scan grid calculations
IFVLS	IFVLS=1 Use HFV for wake-on-lifting surface calculation IFVLS=0 Do not use HFV for these calculations
ISURF	ISURF=0 No surface panel calculation ISURF = 1 Surface panel calculation
ISHIP	o include a ship airwake model in the CHARM solution
IRECON	Flag used for reconstruction of wake geometry to higher resolution
NOISE	NOISE=0 No surface pressure calculation
NLS	NLS=0 No additional lifting surfaces to be modeled with vortex lattices



Parameters from the *rotor/wake* input file:

Parameter	Description
OMEGA	Rotor angular velocity
IROTAT	Rotation direction, "1" for CCW rotation, and "-1" for CW rotation
XROTOR	Position of rotor in the aircraft frame
X,Y,Ztilt	the orientation of rotor in the aircraft frame.
ITILT	ITILT=0 or 1 means apply the lateral tilt (about the +X direction) ITILT=2 means apply the backward tilt
ICOLL	ICOLL=0 The collective is fixed at COLL <sub>D</sub> degrees and the input CT value is simply an estimate used to initialize the wake induced velocity if IFREE=0 ICOLL=1 Collective adjusts until the $C_T$ is equal to the input value of CT
COLL	Initial collective pitch in degrees
CT	Thrust coefficient
ITRIM	ITRIM=0 Cyclic pitch inputs A1s, B1s are fixed
A1W	Lateral cyclic input (radians)
B1W	Longitudinal cyclic input (radians)
A1S	Longitudinal flapping angle (radians)
B1S	Lateral flapping angle (radians)
NOWAKE	NOWAKE=0 A free wake calculation is performed NOWAKE=1: No free wake calculation
ICNVCT	For precise predictions of the downstream flow field, set ICNVCT=0, otherwise ICNVCT=1
NWAKES	NWAKES=0 ignored Wakesnduced velocities between blades
NPWAKE	Number of prescribed wake turns trailing from the free wake
IFAR	IFAR=0: No far wake IFAR=1: Include a far wake consisting of a vortex particle summation
MBCVE	MBCVE=0: Basic Curved Vortex Elements
KSCHEME	KSCHEME=0 Backward difference step
KPC	KPC=0 Single step each iteration KPC=1 Predictor-Corrector step each iteration

Parameters from the *rotor/wake* input file:

Parameter	Description
NCUT	The velocity induced on a blade by the first NCUT elements of its own wake is determined using vortex lattice extensions
AOVLAP	Overlap angle (in degrees).
ISKEW	ISKEW=0 Use straight line elements aligned with the lattice ISKEW=1 Use straight line elements aligned with the local flow angle
IUNS	IUNS=0 Unsteady near wake model not used IUNS=1 Unsteady near wake model activated
NZONE	Number of circulation zones along the blade span
NVORT	Maximum number of vortex trailers representing circulation trailed in Zone IZONE at any azimuth
NPTFW	# of free wake points along vortex trailers in Zone IZONE
IDYNM	IDYNM=1 Normal operation mode. Blade dynamics calculation
SRAD	Shaft or duct radius
SHGHT	Shaft or duct height
NHHI	NHHI = 0 No higher harmonic cyclic pitch inputs

Parameters from the *blade geometry* input file:

Parameter	Description
NSEG	Number of blade segments(must be less than 20)
CUTOUT	Distance from hub axis to blade root
SL	Length of the span of segment
CHORD	Length of the chord at the inboard edge
ELOFSG	Elastic axis offset
SWEEP	Sweep angle (in degrees)
TWRD	Blade root twist at zero collective in degrees
TWSTGD	Twist angle change per segment
ANHD	Anhedral in degree
THCKND	Blade thickness at the root of segment
KFLAP	KFLA=0 segment ISEG has no flaps, KFLAP=1 Plain flaps
FLAPND	Flap length of segment
FLHNGE	Flap hinge offset of segment
FLDEFL	Flap deflection of segment
NCAM	Number of chordwise positions where camber information is supplied
NCHORD	Number of vortex lattice panels chordwise
NSPAN	Number of vortex lattice panels spanwise,
ICOS	vortex lattice layout schemes

Parameters from the *blade dynamics* input file:

Parameter	Description
ISTRM	ISTRM=0 Modal natural frequencies
ISTRIP	=1 <i>Blade Cross – Section</i> input file in CAMRAD format(English Units) =-1 <i>Blade Cross – Section</i> input file in CAMRAD format(SI Units) =0: The vortex lattice method is used after initializing the blade motion with strip theory. ISTRIP=-1 the initial strip theory calculation is skipped.
IFPC	Blade dynamics solved in frequency space using harmonic Analysis
IAERO	flags the aerodynamic model used IAERO=0 Lifting Surface vortex lattice Method with modified with VLM to recover the lift curve slope and zero lift angle in the 2D lookup table
ICOMP	Compressibility correction applied by multiplying vortex lattice matrix
IRVFLO	=0 Reverse flow airloads set to zero
ISTFLO	=1 Original static stall model
IART	Hinge type, IART=0 Hingeless blade, IART=1 Articulated blade
HINGE	Distance of blade hinge from the hub axis, normalized by the radius
PRECONE	Precone angle (degrees)
NMODE	Pitch bearing location
NMDFLP	lowest frequency predominantly flap modes
NMDTOR	lowest frequency predominantly torsion modes
NMDLAG	lowest frequency predominantly lag modes
NMDELG	lowest frequency predominantly elongation modes
IFXMDE	= 0: Normal operation mode
FREQMD	Natural frequency corresponding to mode, nm, normalized by OMEGA
GMASS	is the generalized mass computed for the mode shape(nm)
NRBARS	Number of points along the blade where mode information is stored
RBARS(ir)	X position in blade coordinates of the point, ir, where mode shape information is given (normalized by radius)